INFORMATION TO USERS

This manuscript has been reproduced from the microfilm master. UMI films the text directly from the original or copy submitted. Thus, some thesis and dissertation copies are in typewriter face, while others may be from any type of computer printer.

The quality of this reproduction is dependent upon the quality of the copy submitted. Broken or indistinct print, colored or poor quality illustrations and photographs, print bleedthrough, substandard margins, and improper alignment can adversely affect reproduction.

In the unlikely event that the author did not send UMI a complete manuscript and there are missing pages, these will be noted. Also, if unauthorized copyright material had to be removed, a note will indicate the deletion.

Oversize materials (e.g., maps, drawings, charts) are reproduced by sectioning the original, beginning at the upper left-hand corner and continuing from left to right in equal sections with small overlaps. Each original is also photographed in one exposure and is included in reduced form at the back of the book.

Photographs included in the original manuscript have been reproduced xerographically in this copy. Higher quality 6" x 9" black and white photographic prints are available for any photographs or illustrations appearing in this copy for an additional charge. Contact UMI directly to order.

UMI®

Bell & Howell Information and Learning
300 North Zeeb Road, Ann Arbor, MI 48106-1346 USA
800-521-0600

Measurements of Muon Catalyzed dt Fusion in Solid HD

by

Tracy Ann Porcelli
B.Sc., McMaster University, 1992
M.Sc., University of Western Ontario, 1994

A Dissertation Submitted in Partial Fulfillment of the Requirements for the Degree of

DOCTOR OF PHILOSOPHY

in the Department of Physics and Astronomy

We accept this dissertation as conforming
to the required standard

Dr. G.A. Beer, Co-Supervisor (Department of Physics)

Dr. G.M. Marshall, Co-Supervisor (Department of Physics)

Dr. G.R. Mason, Departmental Member (Department of Physics)

Dr. C. Bohne, Outside Member (Department of Chemistry)

Dr. E. Vogt, External Examiner (Department of Physics, UBC)

Co-Supervisors: Dr. George A. Beer, Dr. Glen M. Marshall

ABSTRACT

The first measurement of muon catalyzed dt fusion ($dt\mu \rightarrow {}^4\mathrm{He} + n + \mu^-$) in solid HD at $\sim$ 3 K has been performed. The theory describing the formation of the $[(dt\mu)pee]$ muonic molecule from the resonant reaction $t\mu + HD \rightarrow [(dt\mu)pee]$, a key process in the dt fusion cycle, can now be tested against the experimental results. Using an experimental technique which employs solid layers of hydrogen isotopes, the energy of molecular formation is determined via time of flight, and dt fusion time spectra in solid HD have been measured. The theory describing the resonant formation of the $dt\mu$ muonic molecule is compared to the experimental results through Monte Carlo simulations. The energy dependent molecular formation rates calculated for HD at 3 K have been employed in the Monte Carlo with the resultant simulated fusion time spectra in fair agreement with the experimental results.

Examiners:

Dr. G.A. Beer, Co-Supervisor (Department of Physics)

Dr. G.M. Marshall, Co-Supervisor (Department of Physics)

Dr. G.R. Mason, Departmental Member (Department of Physics)

Dr. C. Bohne, Outside Member (Department of Chemistry)

Dr. E. Vogt, External Examiner (Department of Physics, UBC)

Contents

List of Tables

List of Figures

Acknowledgements

The number of people to thank is indeed too numerous to list individually, and I hope if I miss anyone they will understand.

Thanks goes to my supervisors George Beer and Glen Marshall for their guidance during my time with UVic. Thanks George for all the time spent revising the thesis and thanks Glen for all the help with analysis and the GEANT simulations. Thanks also goes to Art Olin, Françoise Mulhauser, Paul Knowles and Makoto Fujiwara, for useful discussions on muon catalyzed fusion and suggestions for the thesis, some of which were indeed milestones in understanding the physics involved. A big thanks to Hannes Zmeskal, without whom it is questionable whether the data in this thesis would exist. Another thanks to John Bailey for giving up his vacation time to help prepare the apparatus for the experimental run. Thanks to Maureen Maier for help during the experimental setup. A big thank you to Tom Huber for not only listening to my complaints about his SMC code but responding quickly and positively to them.

Personal thanks to Manuella, Katt, Carlo, Duane and Granny for their continued support of my efforts.

To the memory of my mother

Chapter 1

Introduction

This thesis is been based on data collected in solid deuterium hydride at 3 degrees Kelvin, an experimental first for the study of muon catalyzed fusion in the solid form of HD. The experiment was performed by using a novel target system developed at TRIUMF in Vancouver, Canada. Using a time-of-flight technique, the dt fusion spectra in solid HD have been measured. The theory describing the formation of the $[(dt\mu)pee]$ muonic molecule from the reaction $t\mu + HD \rightarrow [(dt\mu)pee]$, a key process in the dt fusion cycle, is tested against the experimental results through comparisons with Monte Carlo simulations.

Chapter 1 gives a general introduction to muons, fusion in general, and muon catalyzed fusion in particular. Chapter 2 discusses in detail the physics involved in using muons to catalyze fusion, along with the theory specific to resonant molecular formation of $dt\mu$ molecular ions in D_2 and HD. Chapter 3 discusses the apparatus and the idea of solid layered targets. The remaining chapters present the data, the Monte Carlo simulations needed for the analysis and the results.

1.1 Fusion

Hydrogen fusion has long been thought of as the promise for a long-term clean energy source. The energy source that powers the sun and stars has been studied since 1950 and intensely since approximately 1970 in the hopes of reproducing fusion in an energy efficient way to meet future global energy demands [1]. It is estimated that commercial fusion energy could be available before the middle of the next century [1]. This would be a monumental step forward toward a cleaner environment as fusion reactors do not produce air pollutants as does fossil-fuel combustion which cause acid rain that may contribute to global climatic changes. Fusion reactors, unlike fission reactors, do not produce long lived radioisotopes which must be disposed of safely. They do produce energetic neutrons which can cause the reactor structure to become radioactive. However, through the use of low-activation materials this radioactivity can be minimized. There is no need for "geological time-span" disposal of high-level radioactive waste [2] produced by the use of fission reactors. It has been estimated that a fission reactor operating at 1000 kW for one year produces fission products with a total radioactivity of $\sim 6.9\times10^5$ Ci, which reduces to $\sim 6.5\times10^3$ Ci five years after disposal [3].

The most easily activated nuclear fusion reactions are

$$d + t \rightarrow {}^4\mathrm{He} + n + 17.6\ MeV \tag{1.1}$$

$$d + d \rightarrow t + p + 3.98\ MeV \tag{1.2}$$

$$d + d \rightarrow {}^3\mathrm{He} + n + 3.25\ MeV \tag{1.3}$$

$$t + t \rightarrow {}^4\mathrm{He} + 2n + 11.3\ MeV \tag{1.4}$$

$${}^3\mathrm{He} + d \rightarrow {}^4\mathrm{He} + p + 18.3\ MeV \tag{1.5}$$

listed in order of the input energy (or temperature) required to activate fusion [4]. It takes only 1 keV(10^8 J/mol) to start the reaction given in Eq. (1.1); however, this is equivalent

to the gas being heated to approximately 12 million K [4]. For the fusion process to occur at a sufficient rate to be self-sustaining, the temperature required is about 100 million K [2].

In the quest for a clean energy source, the fusion reaction given in Eq. (1.1) is the most promising and efficient source due to its large reaction cross section, approximately 100 times greater than the cross section for the d-d fusion reactions [4,5]. For dt fusion to occur, tritium, which is not naturally occurring, must be produced. By bombarding a naturally occurring isotope of lithium (^6Li with an abundance of 7.42%) with neutrons produced in nuclear fission processes, tritium can be produced via

$$n + {}^6Li \rightarrow {}^4\mathrm{He} + t \ . \tag{1.6}$$

Deuterium, a naturally occurring isotope of hydrogen with an abundance of 0.015%, can be easily extracted from water [6].

It has been an ongoing scientific and engineering challenge to develop methods of obtaining the high temperatures required to cause fusion in the reaction of Eq. (1.1) (which requires the lowest temperature of all hydrogen fusions). Possibilities of producing fusion through different means were sought. It was Sir Charles Frank in 1947 who suggested the use of catalysts to induce fusion in hydrogen isotopes.

1.2 Muons: Discovery and Properties

During the 1930's many cosmic ray experiments took place. The process which caused electronic showers was the topic of interest. An anomaly was observed in the absorption in various materials of electronic showers in the cosmic radiation. Certain particles penetrated deeper into the material than was possible for either electrons or protons [7]. These particles possessed either positive or negative charge and had a mass which was between the mass of an electron and a proton— in the region of 100-200 electron masses [7]. They were first

photographed stopping in a cloud chamber by Neddermeyer and Anderson in 1937 and the mass was estimated to be $\sim$ 240 times the mass of the electron [8]. This new particle was confirmed in 1937 by Street and Stevenson and was given the name muon [9].

Muons from the decay of pions in cosmic rays

$$\pi^+ \rightarrow \mu^+ + \nu_\mu \tag{1.7}$$

were observed in 1947 by Lattes, Muirhead, Occhialini and Powell [10, 11]. It was this discovery which began the "particle physics era" [10]. The observed pions were classified as mesons, particles now known to be made up from a quark-antiquark pair. Muons were classified as leptons— particles which carry integral electric charges, 0 or $\pm|e|$ and interact through electromagnetic (for charged leptons) and weak interactions. Presently there exist three types of leptons— electrons ($e^{\pm}$), muons($\mu^{\pm}$) and taus($\tau^{\pm}$), with their masses satisfying $m_e < m_\mu < m_\tau$. Leptons have associated with them lepton numbers (L_e, L_μ, L_τ), which are conserved in reactions. A lepton number of $+1$ is assigned to leptons (e^-, μ^-, τ^-, ν_e, ν_μ, ν_τ), while a lepton number of -1 is assigned to antileptons (e^+, μ^+, τ^+, $\overline{\nu}_e$, $\overline{\nu}_\mu$, $\overline{\nu}_\tau$). Thus, in Eq. (1.7), the sum of the muon lepton number is zero in all stages of the interaction, indicative of the weak decay.

Muons are approximately 207 times heavier than electrons, but have the same general properties. Muons interact by the weak and electromagnetic forces and decay with a lifetime of 2.2 μs. Due to the large mass of a muon, it will rapidly thermalize when it penetrates matter and will capture onto a nucleus by replacing an electron (note: this is only true for a negatively charged muon). For example, negatively charged muons with an initial energy of $\sim$ 5 keV that penetrate a D_2/T_2 hydrogen mixture consisting of $\sim$ 4×10^{22} nuclei/cm^3 will slow down to $\sim$ 10 eV and be captured on nuclei in picoseconds [5].

1.3 Muons Catalyzing Fusion

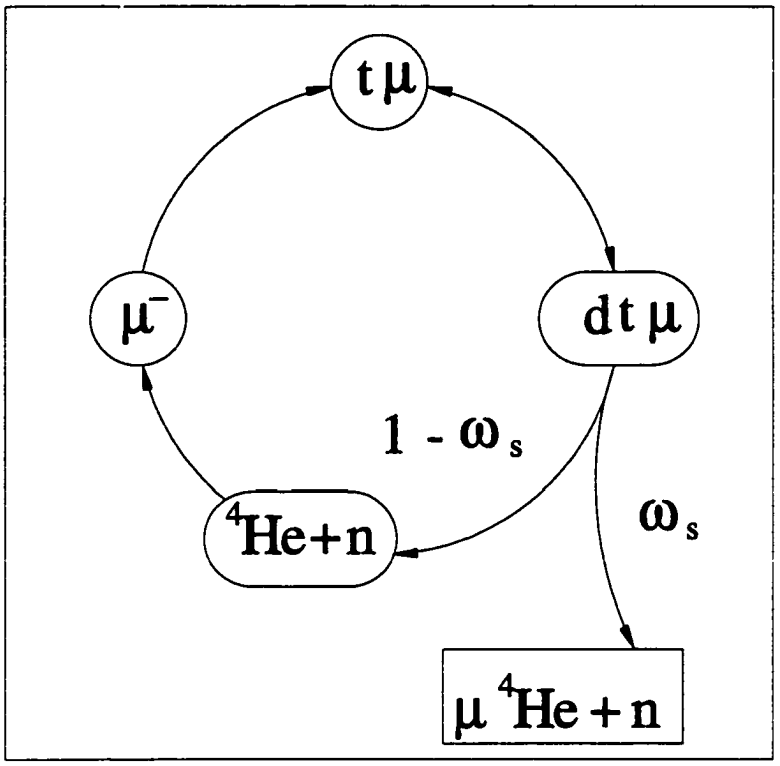

Figure 1.1: *A simplified diagram of the muon catalyzed fusion cycle in a D_2/T_2 hydrogen isotope mixture.*

The idea of using muons to catalyze fusion has been known for over 50 years. The general concept of μCF will be described through the use of the cycling diagram shown in Fig. 1.1 for fusion in D_2/T_2 systems. The process begins when a negative muon is introduced into a D_2/T_2 mixture and is captured by a tritium atom by replacing an orbital electron. This atom, through collisions with D_2 and T_2 molecules, forms a $dt\mu$ muonic molecular ion $(dt\mu)^+$. The d and t atoms are brought close enough together by the muon for the strong nuclear force to cause fusion. The muon may alternatively form a μ^4He atom and thus not

be released back into the cycle to catalyze other fusions. The probability of forming a μ^4He is represented by the sticking coefficient ω_s. Muons which do not form a μ^4He atom can again proceed through the fusion cycle, until the muon either decays or is captured by a ^{4}He nucleus. Muon catalyzed fusion will be discussed in detail in Chapter 2.

The experiment reported in this thesis is the first in which $dt\mu$ fusion in solid deuterium hydride has been studied. In general, experiments to date have concentrated on using either mixtures of D_2 and H/D or H/D/T hydrogen isotopes, as either liquid or gas, at various temperatures and pressures. The TRIUMF experiment is unique not only because it has measured the $dt\mu$ molecular formation rate in a solid target, but because the target consisted of entirely HD molecules with no other forms of hydrogen present.

Chapter 2

Theory

2.1 Muon Catalyzed Fusion; An Overview

The fusion catalyzing processes resulting from the introduction of a negative muon into a mixture of hydrogen isotopes are quite complex due to the many different possible reactions. The various reactions occurring in the muon catalyzed fusion cycle are shown in Fig. 2.1 in which a muon is used as a catalyst to bring two hydrogen-isotope nuclei close enough together to mediate fusion between them, generally producing helium. Muon catalyzed fusion is at least a three step process: a negative muon is captured and forms a muonic hydrogen atom ($p\mu$, $d\mu$, or $t\mu$); a muonic molecule ($pd\mu$, $pt\mu$, $dd\mu$, $dt\mu$, or $tt\mu$) is then formed; finally fusion between the two nuclei occurs in 10^{-5} to 10^{-12} s, depending on which muonic molecule undergoes fusion [5, 12]. A more detailed description of the processes shown in Fig. 2.1 is given below along with specific examples to illustrate and emphasize physics pertinent to the experiment.

The processes involved in muon catalyzed fusion begin when a negative muon is introduced into a mixture of hydrogen isotopes (see the center of Fig. 2.1). The muon will

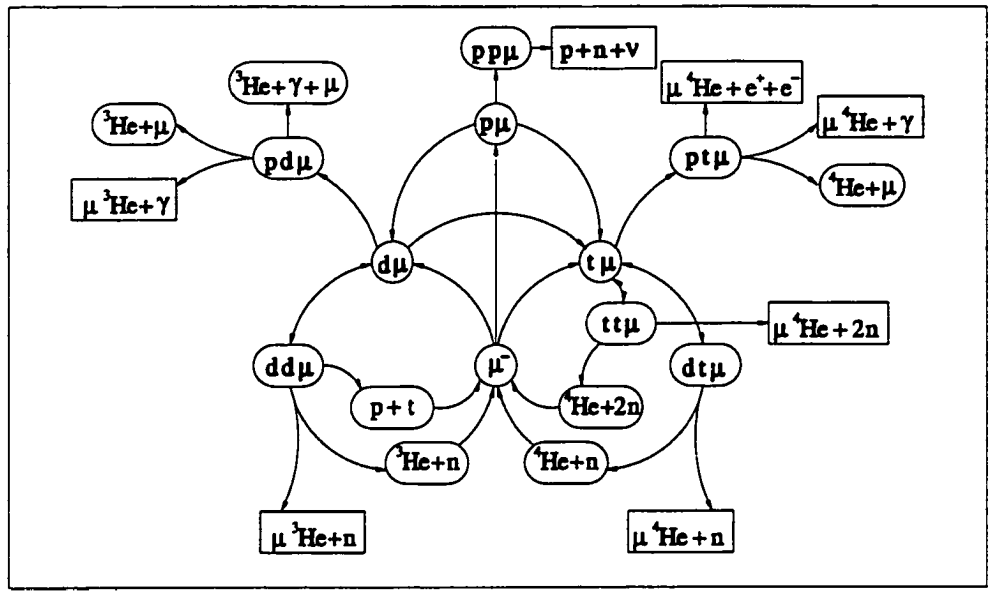

Figure 2.1: *A schematic diagram showing the states which can form during muon catalyzed fusion when a negative muon is introduced into a mixture of hydrogen isotopes. The muon is placed in the center of the diagram. All muonic atoms are enclosed by circles, muonic molecules and fusion products in which the muon is not bound to anything following fusion are enclosed in ellipses. Fusion products in which the muon is stuck to a helium atom or no helium is produced in the fusion process are enclosed by rectangles.*

quickly be captured by an atom (p, d or t) [1]. The muon replaces an orbital electron by transferring energy to the electron greater than its ionization potential. The energy of a charged particle in a hydrogen-like orbital level n, in a Coulomb potential is given by

$$E = \frac{-mZ^2e^4}{2n^2\hbar^2} \tag{2.1}$$

where Z is the atomic number, m is the mass of the charged particle, e is the charge of the particle, and $\hbar$ is Planck's constant. Assuming the muon transfers just enough energy

[1] The capture time could be as small as picoseconds for negative muons in hydrogen with a number density of 2.7×10^{19} cm^{-3} [12].

to ionize a ground state electron in the process of capture, the energy of the bound muon may be set equal to the energy of the previously bound electron. The ratio of the muon's orbital quantum number to that of the electron is thus given by

$$\frac{n_\mu}{n_e} = \sqrt{\frac{m_\mu}{m_e}}. \tag{2.2}$$

Hence, for electrons in the ground state (n_e=1), the muon will be captured by the nucleus in an atomic orbital with $n_\mu \sim 14$, where the muonic orbital has the same size and energy of the ground state electronic orbital [12]. Deexcitation of the muonic atom may occur by Auger, Stark, Coulomb and radiative processes[2]. The muonic atom can slow down in elastic collisions of the type

$$(d\mu)_n + d \rightarrow (d\mu)_n + d. \tag{2.3}$$

A muonic atom can be accelerated by interacting with other atoms and undergoing Coulomb deexcitation. This deexcitation occurs through the collision of a muonic atom with another atom (*e.g.* $(t\mu)_{n_i} + d \rightarrow (t\mu)_{n_f} + d$) where the muon is in a higher initial bound state orbital than after the collision ($n_i > n_f$). As the final state consists of only two particles, they share the released energy from the $n_i \rightarrow n_f$ transition. This energy provides an acceleration mechanism for muonic atoms, allowing them the possibility of obtaining kinetic energies as high as $\sim$ 75 eV [13]. Due to this deexcitation process, the energy distribution of muonic atoms in their ground state is not represented by a Maxwellian distribution (discussed in Section 2.2). The final energy distribution of muonic atoms contains both thermal and epithermal components. "Thermal" refers to a Maxwellian energy distribution which is the same as the average energy distribution of the surrounding medium. "Epithermal" $t\mu$ atoms have higher kinetic energies than thermal $t\mu$ atoms.

[2]For $t\mu$ and $d\mu$ atoms in a $D_2 + T_2$ mixture at liquid hydrogen density (4.25×10^{22} nuclei/cm^3) this occurs on a timescale of 10^{-11} s [5].

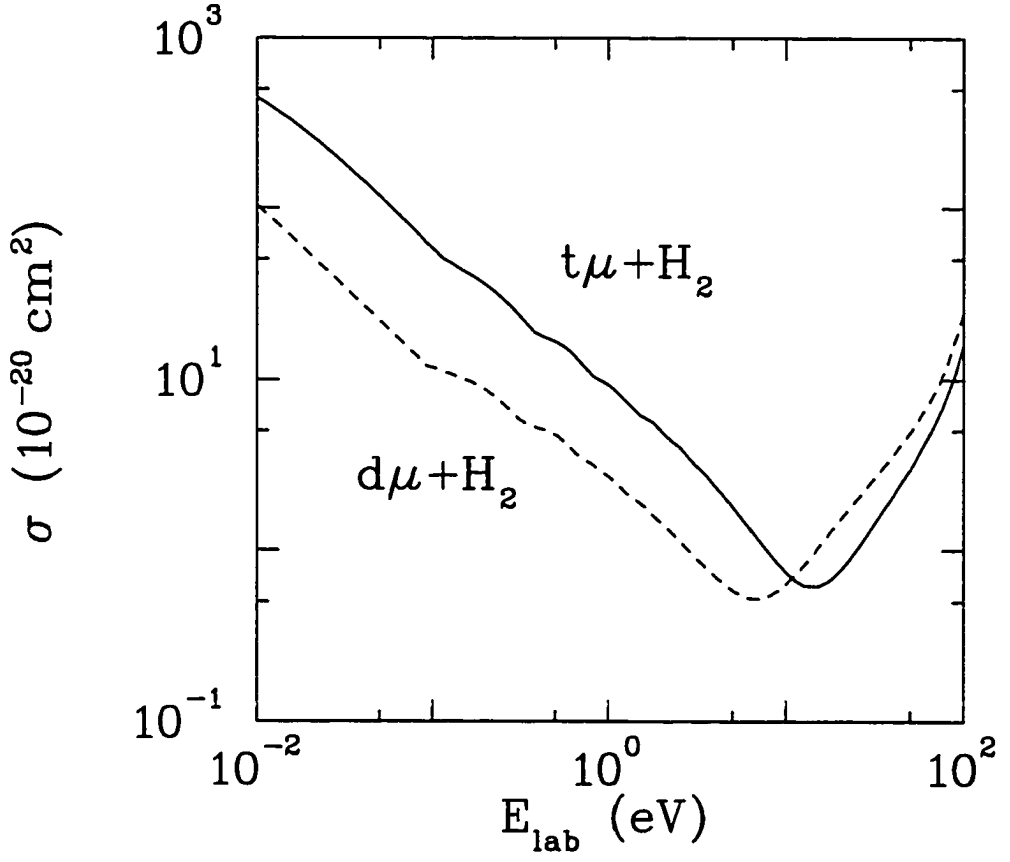

Figure 2.2: *A logarithmic plot of the theoretical elastic scattering cross sections* $\sigma(d\mu + H_2)$ *and* $\sigma(t\mu + H_2)$*, displaying the Ramsauer–Townsend (RT) effect.*

A muonic hydrogen atom in the ground state (1s) has two possible spin states, between which the difference in energy is called the hyperfine splitting. The hyperfine states of a muonic hydrogen atom are determined from the values of the spin quantum number corresponding to the possible total spin values for a muon and the nucleus. Since the spin of a muon is 1/2, and the spin of both protons and tritons is 1/2, the possible hyperfine states for $p\mu$ and $t\mu$ atoms are F=0 and 1 while for $d\mu$ atoms F=1/2 and 3/2, due to the spin 1 deuteron. The hyperfine splitting is $\sim$ 182 meV, $\sim$ 48.5 meV, and $\sim$ 238 meV for $p\mu$, $d\mu$ and $t\mu$ atoms respectively [14]. The scattering of a muonic atom by hydrogen isotopes can cause hyperfine transitions. These transitions occur predominantly as a result of the so called symmetric collisions

$$t\mu(\uparrow\uparrow) + t(\downarrow) \rightarrow t(\uparrow) + t\mu(\downarrow\uparrow) \tag{2.4}$$

through spin exchange (note: the arrows represent the spin states of the particles). In asymmetric collisions such as

$$\begin{aligned} t\mu(\uparrow\uparrow) + d &\rightarrow t\mu(\uparrow\downarrow) + d \\ t\mu(\uparrow\uparrow) + p &\rightarrow t\mu(\uparrow\downarrow) + p, \end{aligned} \tag{2.5}$$

a relativistic interaction is required to flip the spin of the $x\mu$ atoms (where $x = p, d$, or t) and so cross sections for these processes are expected to be 6 to 8 orders of magnitude smaller than those for symmetric collisions [14].

The scattering cross section for $d\mu$ or $t\mu$ atoms on H_2 decreases dramatically over the incident energy range of a few eV, due to the Ramsauer–Townsend effect. The scattering cross section for $d\mu$ and $t\mu$ atoms incident on H_2 is shown in Fig. 2.2. For $d\mu$ and $t\mu$ atoms in the energy range where the cross section is a minimum, they travel macroscopic distances in H_2 because few scattering interactions between the protons and $t\mu$ (or $d\mu$) atoms occur.

A muonic hydrogen atom ($x\mu$) adrift in a hydrogen isotope mixture will interact in

other ways with the mixture (*e.g.* H_2, D_2, T_2, HD, HT, DT). The muon may then transfer to a heavier hydrogen isotope forming a muonic hydrogen atom ($y\mu$) with a larger binding energy. This process is simply due to the reduced-mass ($\frac{m_1 m_2}{m_1+m_2}$) dependence on ground state energy, where m_1 is the mass of the nucleus and m_2 is the mass of the muon. The heavier isotope will form a muonic atom with a stronger binding energy prompting the transfer to occur. For example, the isotopic transfer processes $p\mu + d \rightarrow d\mu + p$ and $p\mu + t \rightarrow t\mu + p$ create muonic hydrogen atoms with kinetic energies of $\sim$ 43 eV and 45 eV respectively, energies equivalent to thermal excitations of thousands of degrees. Because muons transfer rapidly to heavier atoms, any impurities with a high atomic number contained in a mixture of hydrogen isotopes will capture muons from the muonic hydrogen atoms. This will deplete the number of muonic hydrogen atoms which can form muonic hydrogen molecules[3] and subsequently catalyze fusion.

A negative muon can form a bound state between two positive hydrogen nuclei producing a muonic molecule (see Fig. 2.1) by two possible mechanisms. One is the nonresonant Auger process given by

$$x\mu + [yzee] \rightarrow [(yx\mu)_{J\nu} ze]^+ + e \ . \tag{2.6}$$

where x, y and z are any nuclei of the isotopes of hydrogen, e is an electron, and J, ν are rotational and vibrational levels. The muonic atom ($x\mu$) interacts with one nucleus of a hydrogen molecule (y), is captured, and subsequently further Auger deexcitation of the system occurs.

The second process, called resonant formation, proceeds via the reaction

$$x\mu_F + [yzee]_{\nu_i K_i} \rightarrow [(yx\mu)^{J\nu}_S zee]_{\nu_f K_f} \tag{2.7}$$

where $\nu_{i,f}, K_{i,f}$ refer to the initial and final vibrational and rotational quantum numbers of the entire system while J and S refer to the orbital angular momentum and total spin of

[3] A detailed description of this process is given in the section 2.2.

(J,ν)	$pp\mu$	$pd\mu$	$pt\mu$	$dd\mu$	$dt\mu$	$tt\mu$
(0,0)	-253.15	-221.55	-213.84	-325.07	-319.14	-362.91
(0,1)	-	-	-	-35.84	-34.83	-83.77
(1,0)	-107.27	-97.50	-99.13	-226.68	-232.47	-289.14
(1,1)	-	-	-	**-1.9749**	**-0.6603**	-45.21
(2,0)	-	-	-	-86.45	-102.65	-172.65
(3,0)	-	-	-	-	-	-48.70

Table 2.1: *A list of the $yx\mu$ Coulomb molecular bound state energies, in eV, for various isotopic forms of the muonic hydrogen molecule. It is the weakly bound state (J,ν)=(1,1) of the $dd\mu$ and $dt\mu$ molecules which make resonant formation possible for these two molecules. Table is taken from Ref. [15].*

the $yx\mu$ system. Resonant formation depends on the energy levels of all the involved bound states. The collisional energy of the $x\mu$ atom and $yzee$ molecule is partly absorbed by exciting the $yx\mu$ system and partly by exciting the rotational K_f and vibrational ν_f states of the compound six-body molecule $[(yx\mu)^{J\nu}_S zee]_{\nu_f K_f}$. The resonance in the cross section will occur when the incident energy of the $x\mu_F$ atom in hyperfine state F is favourable for the process given by Eq. (2.7) to proceed.

The existence of a loosely bound state of the $yx\mu$ molecular ion makes resonant formation possible. The energy released during formation is transferred to the excitation of the rotational-vibrational states of the six-body complex. A list of the binding energies for the bound states of the $yx\mu$ molecule is given in Table 2.1 [15, 16]. The $dd\mu$ and $dt\mu$ molecules are the only two muonic molecules which have loosely bound states (J,ν)=(1,1) capable of participating in resonant formation. The rotational-vibrational levels (K,ν) can only

absorb $\sim$ 4.5 eV (the dissociation energy of H_2), so strongly bound states cannot undergo resonant formation.

The resonant molecular formation process on its own does not guarantee that the muon will catalyze a fusion between the two nuclei. The product of resonant formation is a molecule in an excited state $J = 1$, with a low probability of contact between the nuclei [17]. The formation process can be reversed by the reaction

$$[(yx\mu)^{J\nu}_{S} zee]_{\nu K} \rightarrow x\mu'_{F} + [yzee]_{\nu' K'}. \tag{2.8}$$

For nuclear fusion to occur, the muonic molecule must be stabilized. Stabilization takes place by the emission of an Auger electron

$$[(yx\mu)^{11} zee]_{\nu K} \rightarrow [(yx\mu)^{01} ze]^{+}_{\nu' K'} + e \tag{2.9}$$

where excitation energy of the muonic ion is carried away by an electron, allowing the $(yx\mu)$ molecule formed originally in the (J, ν)= (1,1) state to deexcite into the (J, ν)=(0,1) state. At high $t\mu$ kinetic energies, Eq. (2.8) may become significant [18]. It has been calculated by M.P. Faifman that back decay (the process represented by Eq. (2.9)) in the $[(dt\mu)dee]$ system can be as high as $\sim$ 45% [18] for $t\mu$ energies of 0.5 eV and as high as $\sim$ 60% for the $[(dt\mu)pee]$ system.

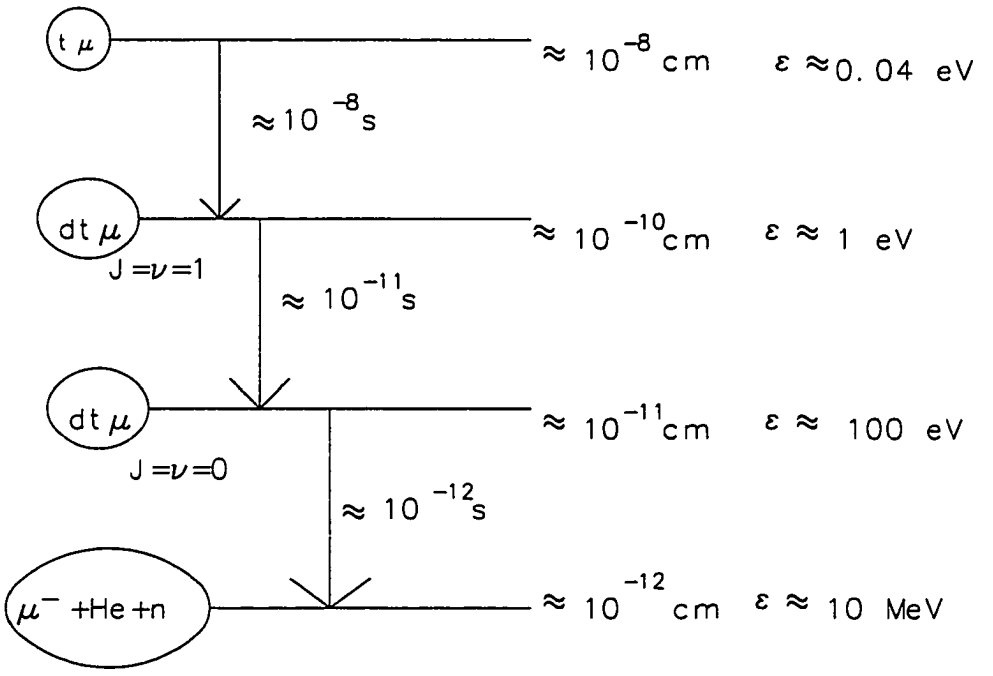

Figure 2.3: *The time, energy and dimensional scale of changes occurring in the muon catalysis cycle. The $t\mu$ atoms, which are on average 10^{-8} cm from other nuclei, form $dt\mu$ molecular ions with average dimensions of 10^{-10} cm in the excited state and 10^{-11} cm in the ground state. Deuterium-tritium fusion takes place at distances of order 10^{-12} cm with an energy release of $\sim$ 10 MeV. The system is compressed in size by a factor of 10^4 in a time of $\sim 10^{-8}$ s with energies of the particles involved increased by a factor of 10^8. Figure is taken from Ref. [5].*

The two hydrogen nuclei in a muonic molecule are close enough to allow tunneling of the nuclei through the Coulomb barrier leading to fusion of the nuclei (see Fig. 2.1). Once the $yx\mu$ is in the strongly bound (J,ν)=(0,1) or (0,0) state, there is a high tunneling probability. Shown in Fig. 2.3 are the time, energy, and dimensional scale of changes occurring in the muon catalysis fusion cycle. $t\mu$ atoms with energies $\sim$ 0.04 eV that are on average a distance of 10^{-8} cm from other nuclei will, in about 10^{-8} s, form $dt\mu$ molecules in the $J = \nu$=1 state with a binding energy of $\sim$ 1 eV and a molecular size of 10^{-10} cm. The $dt\mu$ molecule will deexcite into the 100 eV bound ground state in a time of 10^{-11} s and have an average dimension of 10^{-11} cm. The deuteron and triton fuse (to produce ^{4}He + n) within 10^{-12} s if they are within a distance of $\sim 10^{-12}$ cm, producing an energy release of $\sim$ 10 MeV. This compression of the system by a factor of 10^4 within $\sim 10^{-8}$ s increases the energies of the particles involved by a factor of 10^8 and is possible due to the following unique coincidences and circumstances [5]. If the mass of any particle in the $dt\mu$ system differed even slightly from its currently accepted value, the loosely bound state $J = \nu$=1 would either disappear or become tightly bound and resonant molecular formation (described in detail in the following section) would not be possible. The $dt\mu$ molecule with orbital momentum $J = 1$ allows the strong E1 dipole transition from the $t\mu + D_2$ s–wave scattering state to the $dt\mu$ molecule bound p–state. Because the $dt\mu$ molecule consists of nuclei which are not identical, it cascades into the $J = 0$ state very quickly. There exists a nuclear resonance in the d+t system due to which fusion is enhanced by a factor of 100 compared to the d+d system fusion [5]. The possible fusion reactions for hydrogen isotopes are given in Table 2.2.

In the muon catalyzed fusion cycles there is a chance that the catalyzing muon may "stick" to an atom and not be released to subsequently catalyze further fusions. For example, when helium is produced in the fusion process, the muon can be captured into a bound

Nuclear Reaction	Q value (MeV)
$p + p \rightarrow d + e + \nu_e$	0.42
$p + d \rightarrow {}^3\mathrm{He} + \gamma$	5.49
$p + t \rightarrow {}^4\mathrm{He} + \gamma$	19.77
$d + d \rightarrow {}^3\mathrm{He} + n$	3.27
$d + d \rightarrow p + t$	4.03
$d + t \rightarrow {}^4\mathrm{He} + n$	17.59
$t + t \rightarrow {}^4\mathrm{He} + 2n$	11.33

Table 2.2: *Table of the fusion reactions between the hydrogen isotopes and energy released in the reaction.*

orbit in helium, removing it from the catalysis cycle. Through subsequent collisions of the muonic helium atom with the surrounding material, the muon may be stripped away from the helium, allowing it to reenter the muon catalyzed fusion process. The theoretical value for final sticking of the muon to helium after the muonic helium atom has come to rest is $\sim 0.65\%$ while the most recent experimental measurement gives $\sim 0.56\%$ [19] for the fusion reaction $dt\mu \rightarrow \alpha\mu + n$.

As we have seen from the preceding discussion, the muon catalyzed fusion cycle is far from simple. The formation of muonic molecules can occur by two different processes and is indeed a key step in the fusion cycle. The following section will expand on the details of molecular formation. The effect of resonant molecular formation versus nonresonant formation on the fusion rates and hence fusion yield will be investigated.

2.2 Molecular Formation

As a muon cycles through the fusion process, the formation of a muonic molecule (*e.g.* $dt\mu$) acts as a rate limiting step. The number of fusions that occur is directly dependent on the number of muonic molecules formed. The resonant molecular formation process proceeds one to four orders of magnitude faster than the Auger process, depending on the molecule formed and the incident energy of the muonic atom [20].

The $dt\mu$ molecule formed by a resonant process is formed extremely quickly compared to any other muonic molecules. Because of this, it has gained recent theoretical attention [5, 15, 17, 20–22]. The $dt\mu$ molecule also undergoes fusion much more rapidly and produces one of the highest energy yields (Q values) per fusion (see Table 2.2). Table 2.3 gives resonant and nonresonant molecular formation rates for various processes. The difference in rates between resonant and nonresonant molecular formation is clearly seen from Table 2.3, where the resonant formation rate of $t\mu + D_2 \rightarrow [(dt\mu)dee]$ is four orders of magnitude higher than the similar nonresonant process [15].

The formation of a $[(dt\mu)aee]$ molecular system (where $a = p, d, t$ and represents a nucleus) is due either to a resonant or a nonresonant collision of a DA molecule ($A = H, D, T$ and is a neutral atom) with a $t\mu$ atom in the ground state. For a nonresonant collision, the molecular formation takes place via electric monopole (E0) and electric dipole (E1) transitions [23]. The muonic atom collides with a hydrogen isotope molecule (see Eq. (2.10)). The $t\mu$ atom binds to the d nucleus of the DA molecule and forms a $(dt\mu)^+$ molecular ion which becomes one "nucleus" of the muon molecular complex $[(dt\mu)de]^+$ [5];

$$t\mu + DA \rightarrow [(dt\mu)_{J,\nu}ae]^+ + e. \tag{2.10}$$

The released energy in the above reaction is carried away from the DA molecule by the electron [23].

Process	Resonant Rate	Source
$d\mu(F=3/2)+D_2 \rightarrow (dd\mu)dee$	$4\times10^6 s^{-1}$	E,T
$t\mu(F=0)+D_2 \rightarrow (dt\mu)dee$	$4\times10^8 s^{-1}$	E
$t\mu(F=0)+DT \rightarrow (dt\mu)tee$	$1\times10^7 s^{-1}$	E
Process	Nonresonant Rate	Source
$t\mu(F=1)+D_2 \rightarrow (dt\mu)dee$	$3\times10^4 s^{-1}$	T
$d\mu+H_2 \rightarrow (pd\mu)pee$	$5.9\times10^6 s^{-1}$	T
$t\mu+H_2 \rightarrow (pt\mu)pee$	$6.5\times10^6 s^{-1}$	T

Table 2.3: *A table of the experimental (E) and/or theoretical (T) rates determined at a temperature of 30 K for different muonic molecules. Table is taken from Ref. [15].*

In the resonant process, a $t\mu$ atom collides with one of the nuclei in a DA molecule and excites the system to a higher rotational-vibrational state. Simultaneously, the $t\mu$ atom attaches itself to the deuteron, for example, creating the complex $[(dt\mu)aee]$ where the $dt\mu$ ion is in the $(J,\nu)=(1,1)$ state:

$$(t\mu)_{1s}+[DA]_{\nu_i,K_i} \rightarrow [(dt\mu)_{11}aee]_{\nu_f,K_f} \tag{2.11}$$

and $\nu_{i,f}$, $K_{i,f}$ refer to the initial and final vibrational and rotational quantum numbers of the entire system. The excess energy of the colliding $t\mu$ atom and DA molecule in a resonant process is partly absorbed by exciting the $dt\mu$ system and partly by exciting the rotational and vibrational states of the compound molecule. The $dt\mu$ is formed in a loosely bound state $J{=}\nu{=}1$. The existence of this state makes the resonant formation process possible [17]. The available rotational-vibrational excitations in the resonance process mean that only $t\mu$ atoms with certain incident kinetic energies can participate. Resonant formation is possible

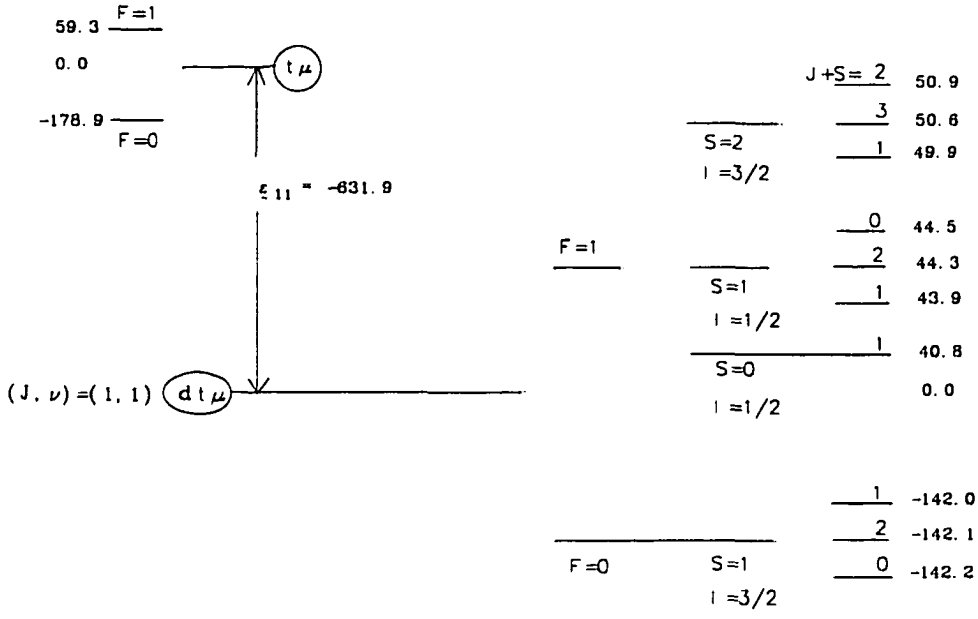

Figure 2.4: *The fine and hyperfine splitting schemes of $t\mu$ and $dt\mu$. The total $t\mu$ atomic spin is given by F, S is the total molecular spin, I is the total spin of the nuclei, and $\mathcal{J}$ is the total angular momentum of the system (orbital angular momentum J + total molecular spin S). All energy values are given in meV. Taken from [5, 20].*

only when the condition

$$\varepsilon_0 + \varepsilon_{11} = \Delta(E_\nu) \tag{2.12}$$

is satisfied for an incident kinetic energy ε_0, where ε_{11} is the binding energy of the (J, ν)=(1,1) state of the $dt\mu$ molecule and $\Delta(E_\nu)$ is the energy difference between the initial state of the DA molecule and the final state of the $[(dt\mu)aee]$ molecular complex. The binding energy of the $dt\mu$ molecule is so small (ε_{11}=−632 meV) that it is insufficient to separate an electron from the DA molecule or cause dissociation of the molecule. The energy released from $dt\mu$ molecular formation is small enough that the DA molecule can absorb this energy provided that a rotational-vibrational level exists in the right place. It is because the

rotational-vibrational (1,1) state is bound very loosely that it corresponds to the energy released and so resonant molecular formation takes place. Shown in Fig. 2.4 are the fine and hyperfine splitting schemes of the $t\mu$ atom and $dt\mu$ molecule with all values given in meV [5, 20]. The original calculations for the level schemes shown in Fig. 2.4 used a non-relativistic approximation of the three-body problem with point nuclei [24,25]. Corrections to these calculations have now been included in the values in the figure. The total shift in energy level (ε_{11}) due to the corrections is 28.3 meV. The binding energy, which includes corrections due to relativistic effects, is given by ε_{11}= −631.9 meV [5]. In the hyperfine structure, F represents the total $t\mu$ atomic spin while S is the total $dt\mu$ molecular spin. The fine structure splitting into level $\mathcal{J}$ gives the total angular momentum of the system ($\vec{\mathcal{J}}$=$\vec{S}+\vec{J}$).

The calculated formation rate of $[(dt\mu)aee]$ is quite sensitive to the precise value of the binding energy of the $(dt\mu)_{11}$. The binding energy of $(dt\mu)_{11}$ has been obtained using a nonrelativistic spinless Hamiltonian,

$$H = -\frac{1}{2m_{13}}\nabla_1^2 - \frac{1}{2m_{23}}\nabla_2^2 - \frac{1}{m_3}\nabla_1\cdot\nabla_2 + \frac{1}{r_1} - \frac{1}{r_2} - \frac{1}{r_{12}}\,, \tag{2.13}$$

where subscript 1 refers to the deuteron, 2 the muon, and 3 the triton; m_{ij} is the reduced mass of particles i and j; r_i is the distance from particle i to the triton; and r_{12} is the distance between the muon and the deuteron [17]. Various methods employed to calculate the binding energy converge on a value of 660 meV. For a satisfactory comparison between theory and experiment, an accuracy of $\sim$ 1 meV in binding energy is required because the calculated molecular formation rate is very sensitive to this value [17]. Theorists aware of the need for an extremely accurate value have made corrections for relativistic, QED, and hyperfine effects, among others [26–28]. The corrections reduce the binding energy of the lowest hyperfine level by $\sim$ 64 meV; however, the uncertainty in this correction is thought to be a few meV [15]. Other uncertainties under investigation include the imprecise knowledge

of the potential arising from deuteron polarizability and the triton charge form factor [26].

Due to the finite lifetime of the molecular complex, the contour of resonance formation has been found to be described best by a Breit-Wigner form and not a delta function corresponding to zero width as previous theories assumed [29,30]. Replacing the delta function form of the resonance by the Breit-Wigner form has led to nonvanishing contributions to the cross section for resonances below threshold which become important at low temperatures. This provides a non-zero probability of $dt\mu$ formation by a $t\mu$ atom in the F=0 hyperfine state interacting with D_2 as the temperature approaches 0 K [31]. Previously, the use of a delta function to model the contour of the resonance formation led to a temperature dependence that produced very small values of the formation rates as the temperature approached zero, in contradiction to experimental results.

The cross section for resonant formation leading to fusion is given by the Breit-Wigner relation

$$\sigma_r = \frac{\pi}{k^2} \sum_{\ell=0}^{\infty} \frac{\Gamma_e^\ell \Gamma_r^\ell}{(\varepsilon - \varepsilon_r)^2 + \frac{1}{4}(\Gamma_e^\ell + \Gamma_r^\ell)^2} \tag{2.14}$$

where Γ_r^ℓ is the partial decay width of $[(dt\mu)_{11}aee]$; Γ_e^ℓ is the elastic scattering width and ℓ is the incident angular momentum; ε is $t\mu$ energy and k is $\sqrt{\frac{2\mu\varepsilon}{\hbar}}$ with μ being the reduced mass of $t\mu$ [22,32,33]. Direct fusion from the state $(dt\mu)_{11}$ is slow ($< 5 \times 10^6$ s^{-1} [17]) and the dominating process is Auger deexcitation into the $(dt\mu)_{01}$ state followed by fusion [22]. Thus, the partial decay width contains both contributions, the partial width for Auger decay and the fusion width

$$\Gamma_r^\ell = \Gamma_A^\ell + \Gamma_f^\ell. \tag{2.15}$$

The Auger decay rate has been calculated to be $\sim 10^{12} s^{-1}$ [30].

Transitions from an initial state with the $t\mu$ atom of total spin F to a final state in which the $dt\mu$ system has spin S, have a transition matrix element given by

$$T_{if} = \langle \psi^i | \hat{V} | \psi^f \rangle \tag{2.16}$$

where ψ^i is the wave function representing the $t\mu$ atom in its ground state and the DA molecule in the initial state while ψ^f is the final state wave function [20]. The transition matrix element can also be represented as a sum of the contributions from matrix elements due to monopole, dipole, and quadrupole contributions:

$$T_{if} = T_{if}^M + T_{if}^D + T_{if}^Q. \tag{2.17}$$

Dominant contributions to Eq. (2.17) come from regions where the deuteron in the $dt\mu$ molecule is much further from the $t\mu$ system than the typical separation between the muon and the triton in either the 1s state of the $t\mu$ or the (11) state of the $dt\mu$ [22]. Thus, the $dt\mu$ wave function valid for infinitely separated $t\mu$ and d is employed. This wave function assumes the distance between the muon and triton is negligible and this distance is set to zero in the calculation of the quadrupole contribution T_{if}^Q.

The $[(dt\mu)aee]$ molecular complex can return to its initial state $(t\mu + DA)$. This process of reversing molecular formation, sometimes called "back decay", must be taken into account when calculating the effective rate for muon molecular formation. The effective formation rate depends on the forward rate for molecular formation as well as the reverse rate. The effective formation rate averaged over initial rotational states and summed over final rotational, vibrational, and spin states can be expressed as

$$\overline{\lambda}^F = \sum_{\nu_f, S, K_f} \omega_{\nu_f}^F(K_f) \lambda_{\nu_f}^{S\,F}, \tag{2.18}$$

where $\omega_{\nu_f}^F(K_f)$ is the Boltzmann distribution of final rotational states given by

$$\omega_{\nu_f}^F(K_f) = \frac{\overline{\lambda}_f}{\overline{\lambda}_f + \Gamma_{\nu_f, K_f}^{S\,F}}. \tag{2.19}$$

Here $\Gamma_{\nu_f, K_f}^{S\,F}$ is the elastic scattering width [22]. The effective fusion rate $\overline{\lambda}_f = \lambda_f + \lambda_{dex}$ is the complex $[(dt\mu)aee]$ stabilization rate, with λ_{dex} being the rate of $dt\mu$ molecule deexcitation from the $J = \nu = 1$ state [34].

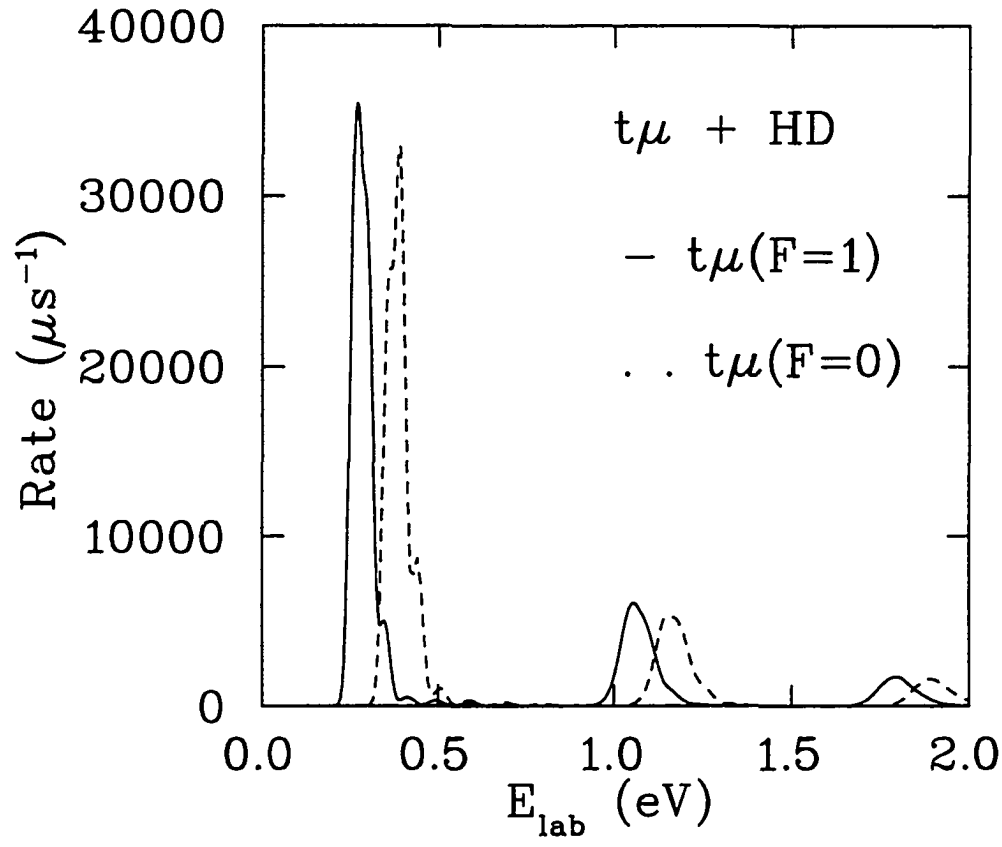

Figure 2.5: *The theoretically predicted formation rate as a function of $t\mu$ lab energy for the resonance structure of $t\mu$+HD→ [$(dt\mu)pee$] calculated at 3 K and normalized to liquid hydrogen density (4.25 $\times 10^{22}$ nuclei/cm^3) by M.P. Faifman.*

For $t\mu + HD \rightarrow [(dt\mu)pee]$ in the energy range $0 < E_{Lab} < 1\ eV$ of $t\mu$ atoms in the hyperfine state F=0, the main contribution to the molecular formation rate at T=0 K comes from the resonances which correspond to the transitions $\nu_f = 2$ and $K_f = 1, 2$ [29]. The predicted resonance structure for $t\mu + HD \rightarrow [(dt\mu)pee]$ at T=3 K is shown in Fig. 2.5 for the two hyperfine states of $t\mu$. The different resonant peaks correspond to different vibrational excited final states of [$(dt\mu)pee$] [35]. The individual rotational transitions cannot be resolved due to averaging over the thermal motion of HD molecules

[18].

The largest peak of $\lambda^F_{dt\mu-p}$ (the molecular formation rate for $t\mu + HD$) comes from the transition from the triplet state F=1 of the $t\mu$ atom and initial vibrational state ν_i=0 of the HD molecule to the final vibrational state ν_f=2 of $[(dt\mu)pee]$ [36]. Shown in Fig. 2.6 is the resonant structure for $t\mu + D_2$ (ortho-states having a symmetric nuclear spin component) for the two hyperfine states. The largest peak of $\lambda^F_{dt\mu-d}$ (the molecular formation rate for $t\mu + D_2$) comes from the transition from the triplet state F=1 of the $t\mu$ to the final vibrational state ν_f=3 of $[(dt\mu)dee]$. Note that the normalization of the molecular formation rates shown in Fig. 2.5 and Fig. 2.6 is not straight forward and is discussed in Appendix A of the thesis.

To calculate the temperature dependence of the resonance reaction rates, the energy dependent formation rates must be averaged over the Maxwellian distribution

$$f(E,T) = 2\left(\frac{E}{\pi}\right)^{1/2} T^{-3/2} e^{-E/T} \ . \tag{2.20}$$

In thermal equilibrium, E is the energy of the particles in thermal equilibrium ($t\mu$ atoms and molecules in the target) and T is the temperature of the scattering medium, both in degrees Kelvin. However, when the $t\mu$ atoms are not thermalized, E represents the energy of the molecules of the target (D_2 or HD). In general, for a $t\mu$ atom of given energy, the formation rate will depend on E_{cm} which includes the energy of both the $t\mu$ atom and the target molecules. The temperature dependence of the resonance reaction rates is given by

$$\lambda^F_{dt\mu-p}(T) = \int_0^\infty \lambda^F_{dt\mu-p}(E) f(E,T) dE \tag{2.21}$$

and the populations of rotational states K_i of HD at a given temperature must also be taken into account [36]. At T=3 K, the maximum formation rate $\lambda^0_{dt\mu-p}$ is on the order of 10^{10}s^{-1} for $t\mu$ atoms of $E_{Lab} \sim$ 0.4 eV [29]. As the temperature increases, the resonance values will decrease due to Doppler broadening. At T=30 K, this rate drops to $6.7\times10^9\ \text{s}^{-1}$

and at T=300 K it is down to 2.31 $\times 10^9$ s^{-1} [29].

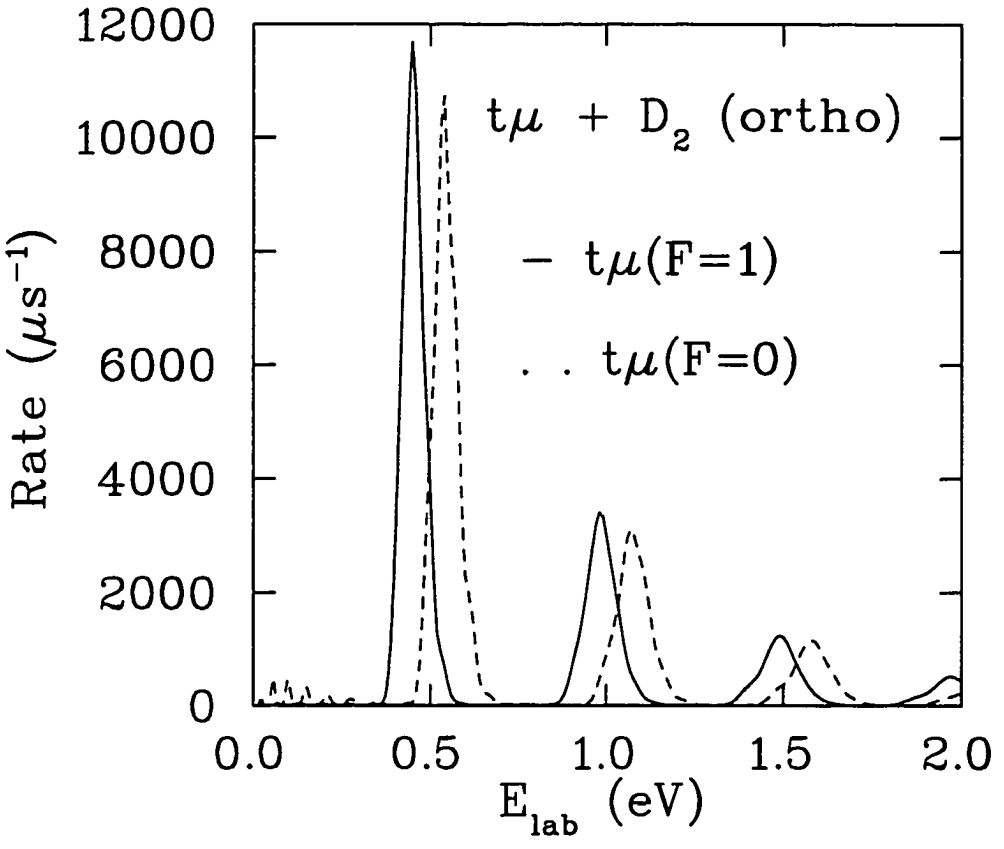

Figure 2.6: *The theoretically predicted formation rate as a function of $t\mu$ lab energy for the resonance structure of $t\mu + D_2 \rightarrow [(dt\mu)dee]$ calculated at 3 K and normalized to liquid hydrogen density by M.P. Faifman.*

The kinetic energy distribution of $t\mu$ atoms before resonant formation occurs has not been measured directly and is not precisely known due to the presence of epithermal muonic atoms (discussed in section 2.1) [15,17,18]. When $t\mu$ atoms are formed in a transfer reaction, they have kinetic energies above thermal. Muon transfer due to the interaction of a triton with a $d\mu$ or $p\mu$ atom occurs at distances of order one muonic atomic unit (2.55×10^{-11} cm), approximately 45 times smaller than the diameter of electron shells in a hydrogen atom. As

electrons do not play a role in this transfer process, the excess binding energy released in the transfer goes into translational motion of the colliding nuclei, not into Auger electrons. If resonant molecular formation occurs before the $t\mu$ atom has thermalized, then the theory needs to account for a non-Maxwellian distribution of muonic atoms which contribute to the molecular formation process.

In order to understand and estimate the fusion yield, it is essential to accurately determine the molecular formation rates since these limit the number of fusions which can occur. However, molecular formation is not the only process involved in the muon catalysis cycle which determines fusion. A muonic atom must first be formed and maintain enough energy to continue in the cycle. Thus, it is important to determine the scattering cross sections for different muonic atoms scattering on various hydrogen isotopes. These cross sections are discussed in the following section.

2.3 Emission Physics and Scattering

The emission of $t\mu$ atoms from solid layers of protium containing a small admixture of tritium is explained by the Ramsauer–Townsend effect (described below) in the scattering cross section for $t\mu$ on H_2. Shown in Fig. 2.7 is the cross section for two different scattering processes. The minimum in the $t\mu + p$ scattering cross section allows $t\mu$ atoms to travel macroscopic distances in protium without undergoing a large number of interactions.

The amplitude for scattering by a spherically symmetric potential is given by

$$f(\theta) = (2ik)^{-1} \sum_{l=0}^{\infty} (2l+1)(e^{2i\delta_l} - 1) P_l(\cos\theta) \tag{2.22}$$

where $P_l(cos\theta)$ is a Legendre Polynomial with θ being a spherical polar coordinate, δ_l is the phase shift of the lth partial wave and k is $\sqrt{\frac{2\mu E}{\hbar^2}}$ for a particle of mass μ and energy E [37]. In low energy collisions which are dominated by $l = 0$ (s-wave) scattering, if the attractive

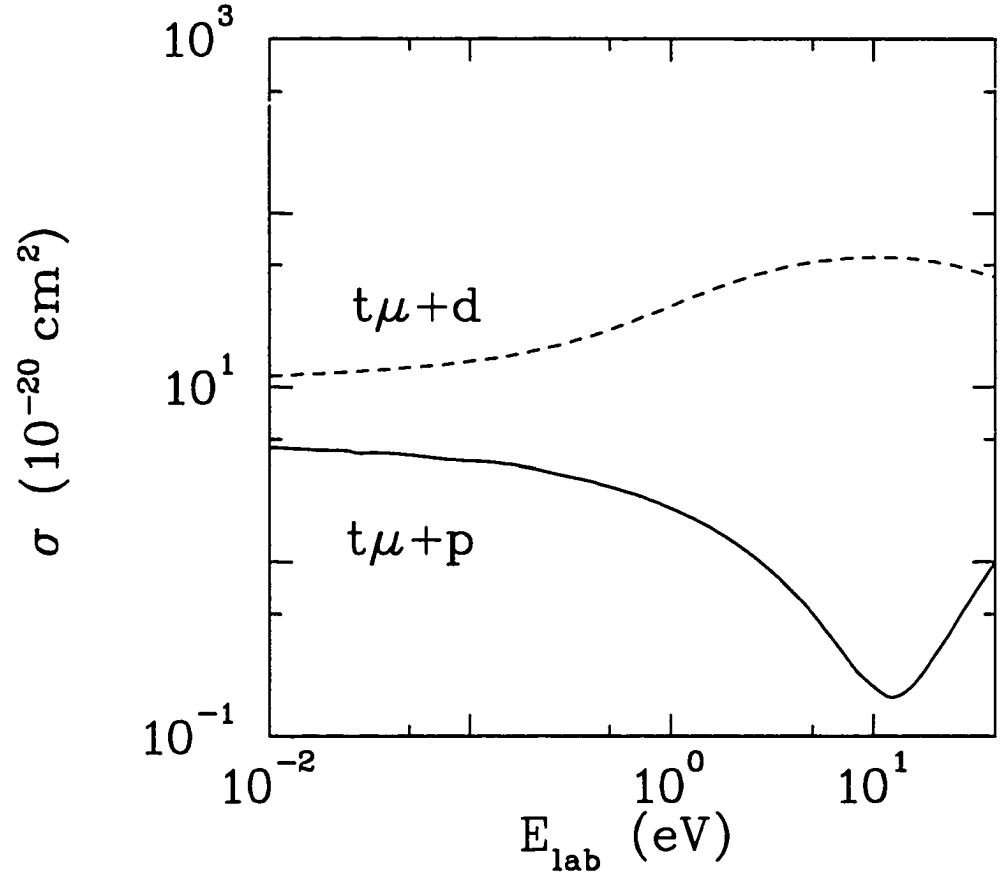

Figure 2.7: *A plot of two asymmetric scattering processes the $t\mu$ atom can take part in. Notice the Ramsauer–Townsend minimum in the $t\mu + p$ reaction.*

potential is strong enough, the $l = 0$ partial wave can be pulled in by the potential and undergo a phase shift of π. In this situation, the scattering amplitude given in Eq. (2.22) vanishes for contributions due to the l=0 partial wave. This is the explanation of the Ramsauer–Townsend minimum [37].

Some of the competing processes in which the $t\mu$ atom can interact are depicted in Fig. 2.7 and Fig. 2.8. The processes shown in Fig. 2.7 are described as asymmetric scattering processes due to the different target and projectile nuclei. The $t\mu$ atom undergoes

a substantial energy loss from scattering on deuterons compared with protons due to the absence of the Ramsauer–Townsend minimum.

The spin flip cross sections shown in Fig. 2.8 for $t\mu + t$ scattering indicate the change in hyperfine state by (i, f) where i is the initial spin state of the $t\mu$ and f is the final spin state after scattering. All plotted spin flip cross sections are for symmetric scattering. The hyperfine splitting of a $t\mu$ atom is ΔE=0.24 eV. There are two possible type of processes: collisions with energy less than ΔE and those collisions with energy greater than the threshold energy ΔE. In the first case, only elastic scattering in the lower state of the muonic atom hyperfine state is possible because spin flip is not allowed for $E < \Delta E$ [38]. In the second case, elastic scattering $(t\mu)_F \rightarrow (t\mu)_F$ can occur as well as inelastic processes $(t\mu)_F \rightarrow (t\mu)_{F'}$. For all cross sections, a peak occurs at an energy of $\sim$ 3 eV which comes from the $J = 2$ partial wave contribution to the cross section. For the reaction $(t\mu)_0 \rightarrow (t\mu)_0$ a threshold peculiarity occurs at the collision energy of 0.241 eV (ΔE), the energy gained or released in the scattering to allow a change of hyperfine state.

The number of fusions occurring is determined by two competing processes: molecular formation and the slowing down of $t\mu$ atoms due to scattering. For $t\mu$ atoms in the energy range of the dominant $dt\mu$ resonant molecular formation peak, molecular formation is the most important of all possible reactions. The molecular formation rate can be expressed as a cross section by the formula

$$\sigma = \frac{\lambda}{\nu \phi N_0} , \tag{2.23}$$

where σ is the cross section, λ is the rate, ν is the speed of the incident $t\mu$ for a target at rest, and ϕN_0 is the atomic number density of the scattering medium. In HD at 3 K (see Fig. 2.5), the resonant rate $\lambda_{dt\mu}$ is on the order 10^{10} s^{-1} for a $t\mu$ of incident energy 0.3 eV (speed=4.3 mm/μs) which corresponds to a cross section $\sigma_{dt\mu}$ of order 10^{-18} cm^2 and clearly dominates over the $\sigma_{t\mu+d}$ and $\sigma_{t\mu+p}$ scattering cross sections shown in Fig. 2.7.

However, an incident $t\mu$ energy of $\sim$ 1.1 eV which corresponds to the second resonance for molecular formation (for HD) and a rate $\lambda_{dt\mu}$ of order 10^9 s^{-1} corresponds to a cross section $\sigma_{dt\mu}$ of $\sim 10^{-19}$ cm^2. This is now in direct competition with the $\sigma_{t\mu+d}$ scattering cross section shown in Fig. 2.7. As the $\sigma_{t\mu+p}$ scattering cross section is lower than the $\sigma_{t\mu+d}$ scattering cross section, it is the latter which contributes more to the scattering in HD.

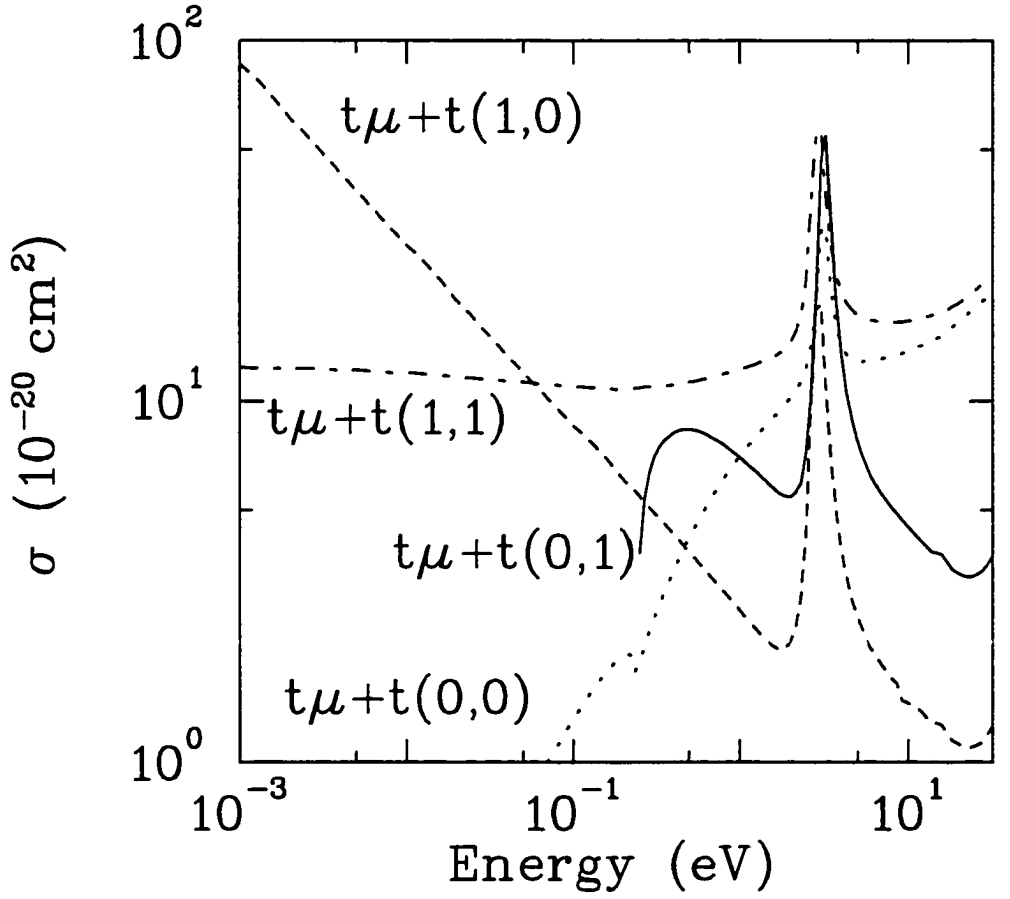

Figure 2.8: *The spin flip cross sections for $t\mu+t$ scattering. The hyperfine state is indicated by (i, f) where i is the initial spin state of the $t\mu$ and f is the final spin state after the scattering occurred. Note that the energy is in the center of mass frame.*

Due to the Ramsauer-Townsend minimum, muonic tritium atoms can be emitted from a solid layer of protium containing an admixture of tritium. By moderating the energy of the emitted $t\mu$ atoms, an optimum situation for muon catalyzed fusion arises by having the atoms reach a solid layer of HD with an energy corresponding to one of the molecular formation resonances.

2.4 Solid HD

Deuterium hydride (HD) has been studied in only a few muon catalyzed fusion experiments and mainly in the gaseous state [39–46]. These previous experiments have been conducted with both non-equilibrated and equilibrated HD ($25\%H_2$, $25\%D_2$, $50\%HD$). The experimental values of the $dd\mu$ molecular formation rates for $d\mu$ atoms scattering on HD versus scattering on D_2 were found to be different (by a factor of approximately 10 [41]), prompting theorists to reexamine HD more closely. Recently the resonant molecular formation rate $\lambda_{dt\mu}$ for an HD target in the solid state at 3 K has been calculated using the methods discussed in [22, 29].

The theoretical analysis of HD makes the assumption that the molecules do not interact with their neighbours in the crystal lattice. The solid hydrogens (H_2, D_2, T_2, HD, HT and DT) are crystalline, bound together by the Van der Waals force. The crystals have a close-packed structure where each molecule is surrounded by 12 molecules (nearest neighbours) at an equal distance from the central molecule. Although an infinite variety of disordered close-packed structures exist in nature, two of the most efficient packing schemes are the face-centered cubic (f.c.c.) and hexagonal close-packed (h.c.p.) ordered structures [4]. The volume per molecule in both of these structures is the same and thus there is no way to predict which structure is most probable for hydrogen. Depending on the technique used to freeze hydrogen, it has been shown that both crystal structures can be produced [4].

Solid hydrogen is a quantum crystal (described below). Due to the small mass of hydrogen molecules and relatively weak intermolecular forces, the amplitude of the zero-point lattice vibrations is an appreciable fraction of the lattice constant (numbers specifying the size of a single cell) [47] . The spatial width of a single particle distribution is approximately 18% of the nearest neighbour distance due to the zero-point motion of the molecules (zero-point energy=$\frac{1}{2}\hbar\omega$ [48]) . A simple description of a quantum crystal is to picture the stable ground state as an arrangement of large, single molecule, zero-point distributions around the sites of a regular lattice, and the low-lying excitations of the crystal as collective oscillations of the distributions around their equilibrium positions. The zero-point motion of a molecule can create small distortions in lattice packing, causing the structure to have broken symmetry and deviate from a perfect packed lattice.

Deuterium hydride is a heteronuclear molecule because of the distinguishably different atoms H and D and so has features which are not found in the homonuclear hydrogens. Heteronuclear hydrogens can have thermal energy flow between any rotational levels with the change in the rotational quantum number $\Delta J = \pm 1$ being the most common. The heteronuclear hydrogens adjust instantaneously to changes in temperature. Homonuclear hydrogens cannot have $\Delta J = \pm 1$ thermal transitions due to quantum symmetry and interactions with nuclear magnetic moments [4]. For H_2, D_2, and T_2 molecules, the thermal deexcitation rule is $\Delta J = \pm 2$. Low concentrations of a $J = 1$ molecule in a lattice of $J = 0$ molecules can be regarded as impurities. The electric quadrupole field of a $J = 1$ molecule can polarize surrounding $J = 0$ molecules, creating excess binding energy of the impurities in the lattice. This results in a fluctuating Van der Waals interaction which produces an anisotropic distortion varying with impurity orientation, causing some neighbours to move closer while others move further away from the $J = 1$ molecule. The fractional population of $J = 1$ molecules in HD at 4.2 K is 1.6×10^{-13} and increases to 0.11 at 40 K.

Deuterium hydride, until recently, had to be synthesized and purified. Now the commercial availability of HD means that only purification is necessary [4]. Despite its current availability, it is not a substance for which an abundance of data exists. The work presented herein is the first for which a solid deuterium hydride target was employed to study muon catalyzed fusion. Not only is that exciting in itself, but the resonant molecular $dt\mu$ formation rate which has only recently been calculated can now be compared to experimental results.

Chapter 3

Apparatus and Procedure

The processes involved in muon catalyzed fusion reactions, discussed in the previous chapter, are indeed complex and conventional experimental techniques are not always able to separate the processes of interest. The target system developed at TRIUMF and discussed in this chapter is a novel approach to disentangling the complex processes. Instead of the conventional liquid or gas targets used to study μCF, different hydrogen isotope concentrations are frozen onto two separated target foils. Because the hydrogen isotopes are frozen, it is possible to deposit multilayer structures and have the different isotope concentrations and layers remain separate. The geometrical separation of the concentrations can then be used to spatially confine different reaction processes.

3.1 The M20 Beam Line at TRIUMF

The experiment was conducted at TRIUMF, in Vancouver, Canada using the M20B beam line shown in Fig. 3.1. The creation of a negative muon beam begins with the 500 MeV proton beam striking a 10 cm beryllium production target producing pions. These pions decay close to the beryllium production target through the electroweak process $\pi^- \rightarrow$

$\mu^- + \overline{\nu}_\mu$. Negatively charged muons with a momentum of 26.9 MeV/c and a Δp/p (FWHM) of $\sim$ 5 % are selected by the B1 magnet and this muon beam was used in the muon catalyzed fusion experiment discussed in the thesis. The M20B beam line contains an 80 kV Wien filter which is used to remove (separate) electrons from the muon beam [49,50]. The filter consists of two parallel high voltage plates which create an electric field and a coil which creates a magnetic field perpendicular to this electric field. Final focusing of the beam is done by quadrupole magnets which deliver a beam size of $\sim$30 mm (FWHM). These muons exit the beam port and strike the experimental target at a typical rate of $\sim$ 3700 s^{-1}.

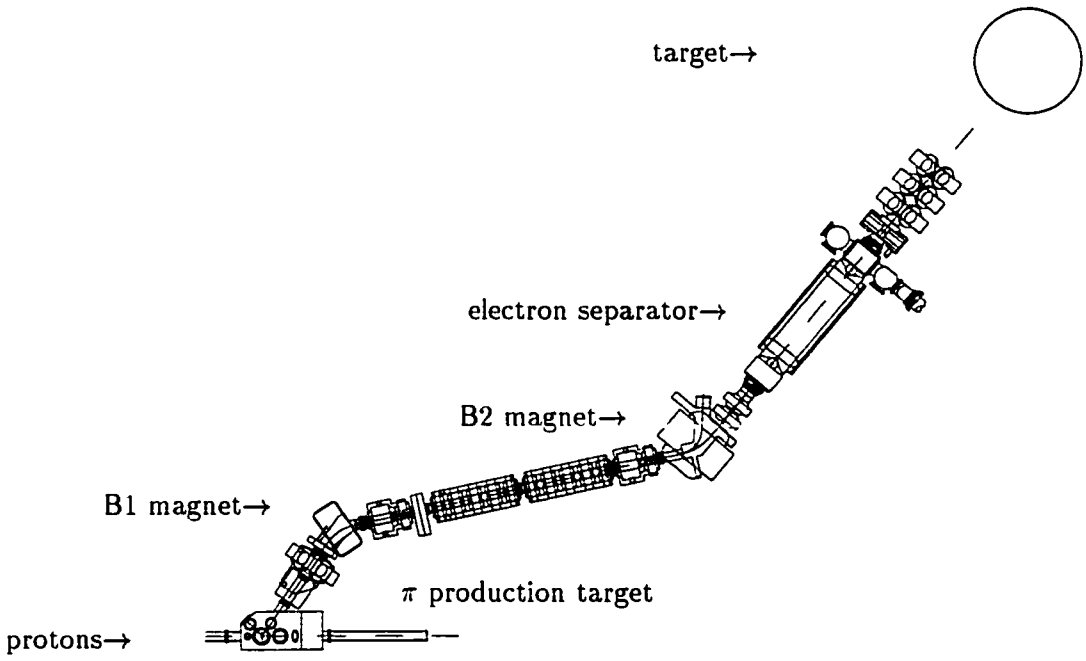

Figure 3.1: *The M20B beam line at TRIUMF.*

3.2 The Target System

3.2.1 The Cryostat

The target system used for the experiment consisted of two 65 mm diameter gold foils onto which gaseous mixtures of hydrogen isotopes were deposited and frozen. In order to freeze the gas and keep it frozen on the foil where it was deposited, the target temperature had to be maintained between 3 and 4 K. If the temperature rose much above 4 K, the solidified gas became unstable and vaporized extremely rapidly.

The cryogenic system was designed in cooperation with Quantum Technology Corporation in British Columbia, Canada. The cryostat shown in Fig. 3.2 operates with a continuous flow of cold helium gas extracted from a storage dewar through a transfer line, into the cryostat, and removed with a pump. A manual needle valve on the transfer line regulated the flow of helium from the storage dewar while the pump provided low pressure to allow the helium to vaporize and cool. Steel wool was placed in the helium gas flow path of the cryostat to slow the flow of gas and increase the cooling power of the 70 K heat shield (see Fig. 3.2) [51].

The cryostat was enclosed in a steel tube of 500 μm wall thickness. The vacuum region between the outside of the cryostat and the inside of the steel tube is referred to as the tritium barrier space (TBS) and acted as a barrier between helium flow in the cryostat and the region of the vacuum system which was exposed to tritium. This space was constantly monitored for leaks and was put in place as a safety precaution to reduce the chance of tritium contaminating the recycled helium gas. Cylindrical copper blocks provide good thermal contact between the cryostat and outer steel enclosure by having a surface area large enough to overcome the limited thermal conductivity of the steel tube. Indium was placed in all joints to increase thermal conductance [51].

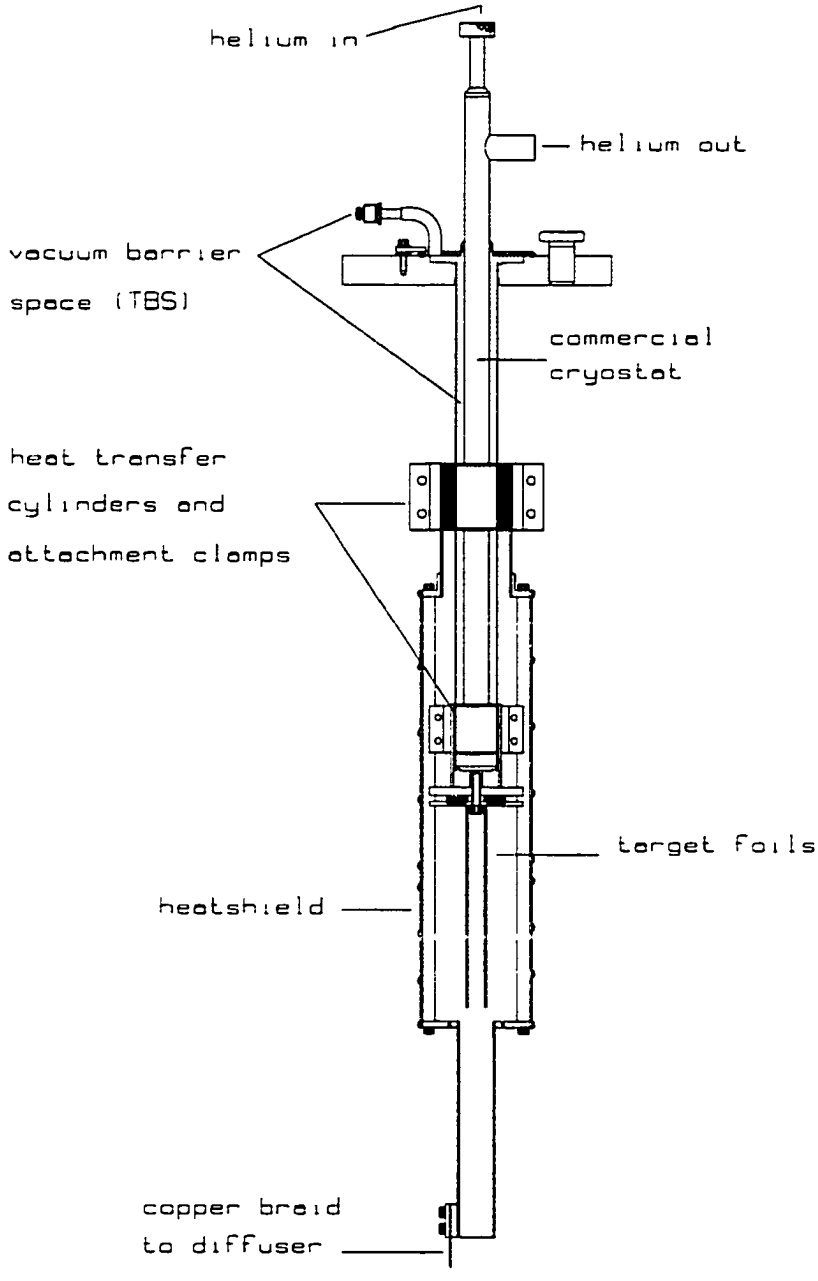

Figure 3.2: *A schematic drawing of the cryostat. Helium is brought in through the top, circulated through the cryostat and pumped out. A 70 K heat shield surrounds the two gold target foils which remain at* $\sim$ *3 K.*

Gold foil was chosen for the target support because its low emissivity reduces the radiative heat load from other surfaces. It also has other advantages. Muons react with gold by a capture process emitting a spectrum of neutrons. This spectrum is well understood in both energy and time. Gold was plated onto all exposed surfaces surrounding the target foils to ensure that the background present in the experiment was well understood and for emissivity purposes. The two 50 μm thick gold target foils were cold soldered with indium to gold-plated copper frames. These copper frames were mounted with clamps to the coldest part of the cryostat.

A heat shield surrounded the target foils to absorb thermal radiation produced by the room temperature vacuum system. This shield was attached to the cryostat at the 70 K cooling stage. The 10 W heat load coming from the vacuum system was removed by utilizing the cold exhaust gas from the 3 K cooling stage of the cryostat. The temperature was monitored at several places in the cryostat using constant-current silicon diodes. For very low temperatures, carbon-glass resistors (low temperature sensors provided by LakeShore Cryotronics Inc., Westerville, Ohio) were placed on the target frames to measure the temperature more precisely.

3.2.2 Gas Deposition System

Gaseous mixtures of hydrogen isotopes were deposited onto the gold target foils using the diffuser shown in Fig. 3.3. A diffuser chamber (labelled N) was mounted on each side of a gold plated copper support plate (labelled L). Each diffuser had an independent gas supply line to deposit gas which then froze in a solid ~60 mm diameter layer onto each of the two cold gold foils separately. Each diffuser deposited $< 0.1\%$ of gas onto the target foil furthest from it [52]. The gas exited the diffuser through a 500 μm thick layer of porous sintered stainless steel. The characteristic diameter of the largest particle which can pass through

the pores was 2 μm. The total diffuser thickness (*i.e.*, the assembly of two chambers and support copper) was 9 mm which limited the distance between the target foils to $\sim$ 16 mm when target thickness and thermal distortions were taken into account [51].

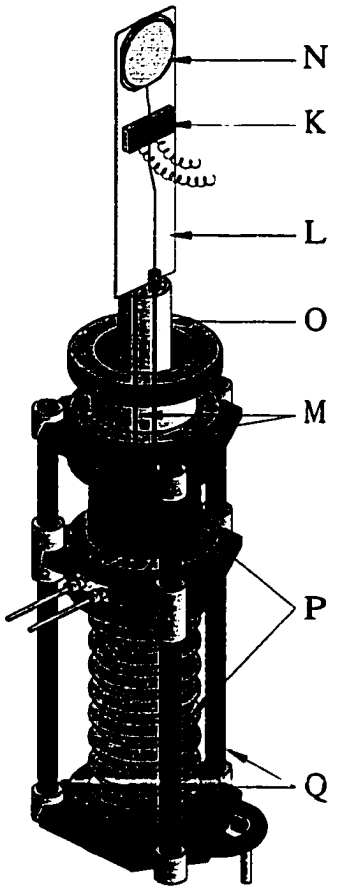

Figure 3.3: *A depiction of the diffuser from one side, labelling the diffuser chamber (N), copper braids to connect to the heat shield (K), copper support plate (L), support cylinder (O), bellows and vertical displacement guides (P,Q).*

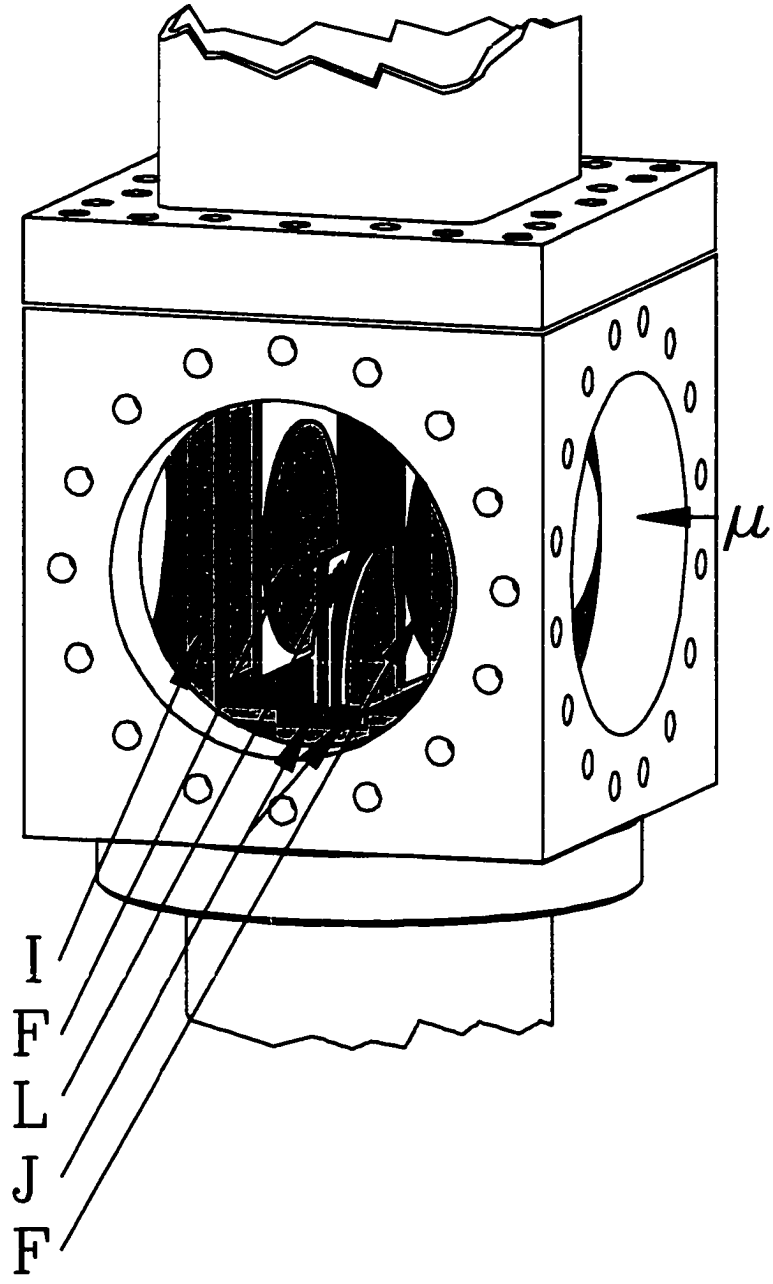

Figure 3.4: *A view of the target system with the stainless steel windows removed. The muons enter the target as indicated. The silicon detectors are not shown but are mounted perpendicular to the target foils. Shown are the heat shield (I), the gold target foils (F), the half-inserted diffuser (L) and its guide rails (J).*

The diffuser's copper support plate was mounted on a thin-walled stainless steel cylinder connected to a movable flange for insertion and removal of the diffuser between the target foils. Two flexible copper braids connected the copper support plate to the cryostat radiation shield (see Fig. 3.2). This allowed for a vertical displacement of 160 mm while maintaining the diffuser temperature around 100 K to reduce the heat load on the target.

Both the cryostat and gas deposition system were attached to a stainless steel cube as shown in Fig. 3.4. The cryostat was inserted through the top port while the deposition system and pumps were attached through the bottom port. Muons entered the target vacuum system through a 25 μm stainless steel window located on one side of the cube. Stainless steel windows covered the remaining three ports. Two silicon detectors were located inside the cube mounted on the thermal shield and placed perpendicular to the target foils. The port opposite the beam entrance window contained a 3 mm thick window behind which a neutron detector was located. Another neutron detector and one germanium detector were placed facing the remaining two ports (see Fig. 3.9).

3.2.3 The Gas Rack

The target gases were prepared in the gas rack before deposition onto the cold target foils. The gas rack was designed for the preparation of high-purity mixed hydrogen isotope gases but also has been used for neon gas. A schematic drawing of the gas rack, vacuum pumps, hydrogen isotope storage, and gas storage beds along with valves used to regulate gas flow is shown in Fig. 3.5.

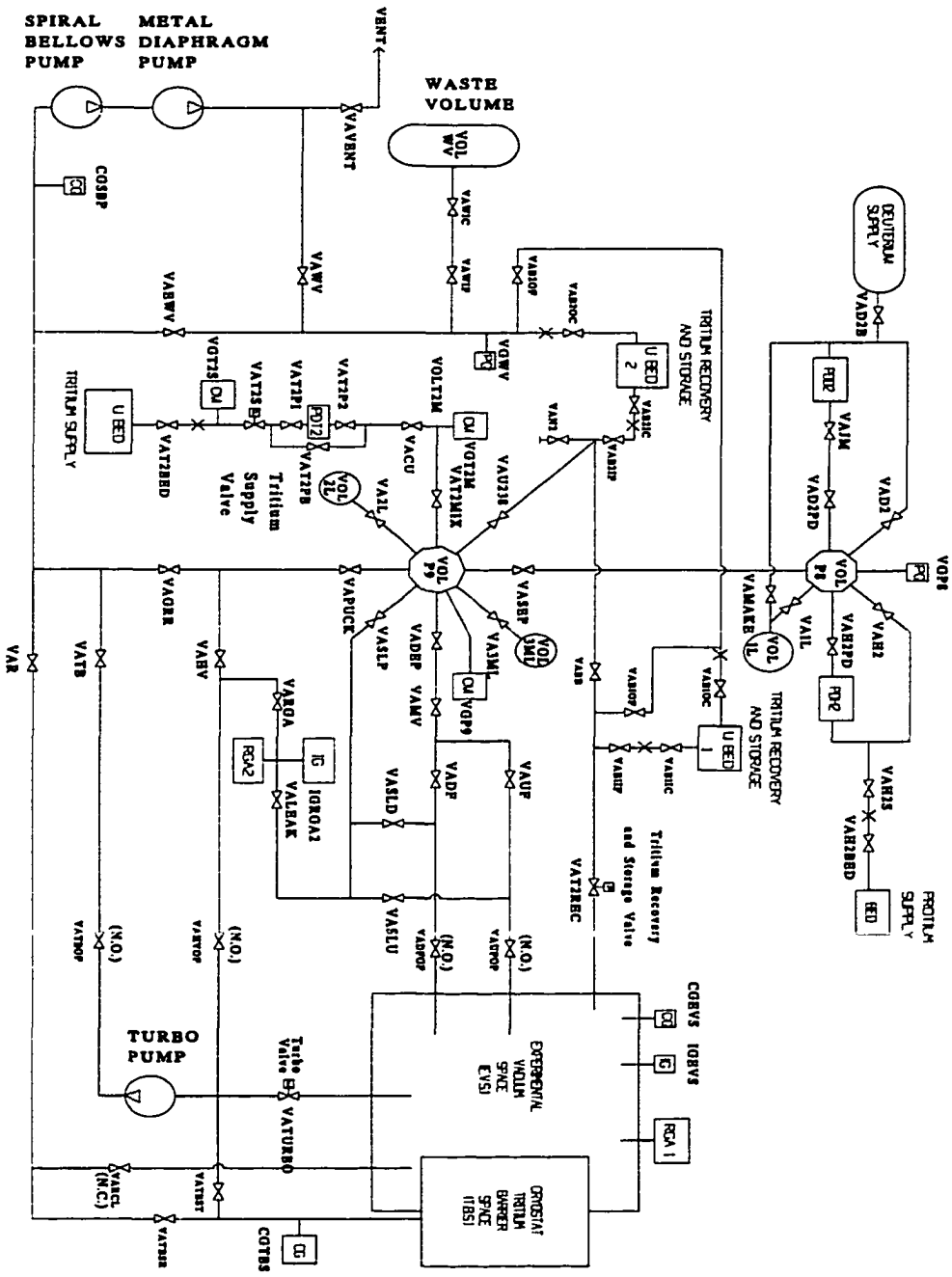

Figure 3.5: *A schematic drawing of the gas rack, vacuum pumps, hydrogen isotope storage and supply beds, along with valves to regulate gas flow. Valves are labelled by the prefix VA, volumes by VOL, palladium filters by PD, vacuum gauges by VG, ion gauges by IG, and residual gas analyzers by RGA.*

For this experiment, four gases were prepared for use as targets: protium, deuterium, tritium, and deuterium hydride. Isotopically pure protium was generated by the electrolysis of deuterium-depleted water. Because the electrolysis apparatus malfunctioned during the experiment, a bottle of protium was mounted onto part of the gas rack and the gas was passed through a commercial palladium filter for purification. The deuterium gas used was passed through a Johnson-Mathey palladium filter for purification. The tritium gas supply was stored in a uranium bed and the bed was heated to activate the release of tritium. The tritium was passed through a palladium (Pd) filter (designed by the Muonic Hydrogen collaboration and discussed in the following paragraph) to remove ^{3}He gas which was produced in the uranium bed due to tritium decay ($t \rightarrow {}^3\mathrm{He} + \beta^- + \overline{\nu}$).

A great deal of planning was needed in the construction and design of the filter to ensure that the tritium gas passed through the palladium filter quickly. Hydrogen is highly soluble and mobile in the face centered cubic Pd lattice structure. The transfer of hydrogen gas into the Pd lattice consists of two steps: the adsorption of hydrogen molecules at the Pd surface and the passage of hydrogen atoms from the surface sites into the lattice [53]. Heating the Pd expands the crystal lattice and allows hydrogen atoms to pass through the lattice by occupying octahedral sites between the Pd atoms. As the coefficient for hydrogen to permeate and travel through the Pd depends on the pressure of unfiltered hydrogen gas contained before the Pd membrane, the volume of tubing the unfiltered gas travelled through before entering the filter was minimized. Previous testing of the Pd filter indicated that tritium would escape through the stainless steel containment which housed the filter if the temperature rose above 320 °C. Thus, during the experiment the filter was heated to only $\sim$ 300 °C.

The deuterium-hydride gas used was supplied by Cambridge Isotopes with a composition of 96% HD with a nonhydrogen contamination of less than 100 ppm. A palladium

filter to purify the gas could not be used since it would equilibrate the HD and the resultant mixture would be composed of $H_2 + D_2 + HD$. Instead, a molecular sieve (zeolite) contained in $\sim$ 125 cm^3 of copper tubing placed in a liquid nitrogen bath was used to remove nonhydrogen impurities from the HD. Zeolites are composed of aluminum and silicon and the chemistry involved to adsorb other elements which pass through the zeolite is based on its tetrahedron structure [54]. By varying the Si/Al ratio in the zeolite composition, gases are separated based on the size and shape of their atoms; some atoms are trapped in the zeolite while others move freely through the sieve. The spacing between the atoms making up the zeolite is governed by windows composed of rings of linked tetrahedra in the Al/Si crystal structure. Zeolites having a hexagonal (6 ring) crystal structure can be traversed by only the smallest molecules [54] and are suitable to allow HD molecules to pass through them.

The amount of gas used for target deposition was measured by allowing the hydrogen gas (protium, deuterium, tritium, deuterium hydride) to be bled into a container of known volume in the gas rack, filling that container to a predetermined pressure and sealing the volume. An accurate measurement of the pressure along with the known container volume and temperature allowed the amount of gas to be determined. All target thicknesses were measured in Torr-liters. The volumes (containers) used in the gas rack are labelled in Fig. 3.5 as VOL1L, VOL2L, VOL3ML, VOLT2M, VOLP8 and VOLP9. The capacities of these volumes are 1005.0$\pm$ 2.0 cm^3, 1996.2$\pm$ 0.3 cm^3, 3.42$\pm$ 0.04 cm^3, 9.30$\pm$ 0.06 cm^3, 21.41$\pm$ 0.14 cm^3 and 31.2$\pm$ 0.2 cm^3 respectively. Two containers, VOL1L and VOL2L, were measured by filling them with water and measuring the difference in weight. The remaining volumes were measured by the expansion of gas from a known volume (VOL1L or VOL2L) to the volume in question; by measuring the pressure of the gas in the known volume and the pressure of gas after expansion, the unknown volume was calculated.

These volumes were used to prepare gases for deposition onto the target foils. The gas targets were prepared as follows. Depending on the amount of gas required, and if more than one gas was to be used, more than one volume was needed. To prepare a gas mixture, the first volume was evacuated and filled with gas to the desired pressure and then sealed by closing a valve (*e.g.*, protium). An adjacent known volume was then filled with another gas and sealed (*e.g.*, tritium). By opening valves which connect the two volumes, the gases were mixed. For safety reasons the pressure of the gas mixture was kept below one atmosphere due to the possibility of pressurized tritium escaping in the event of a small leak. If the above procedure required the gas mixture to exceed one atmosphere then a different procedure to mix the gases was needed. Instead, the second gas was bled directly from its source into the large volume which already contained the first trapped gas. When the total pressure of the mixture reached its desired pressure the volume was sealed. Using this procedure, the gas concentrations are accurate to about 1%.

To deposit the gas onto the gold target foils, the deposition line leading to the foil was opened. For deposition onto the upstream (US) foil (the foil closest to muon entry), valve VAUF (VAlve Upstream Foil) was opened. Equivalently, valve VADF (VAlve Downstream Foil) would be opened for gas deposition on the DS (downstream) foil. The valve VADEP (VAlve DEPosition) used for gas deposition was then opened and the gas flow was regulated manually with a metering valve (VAMV). The gas then passed through the deposition line, out through the diffuser, and onto the cold gold foil. During a gas deposition, the target temperature must remain around 3 K (no higher than $\sim$ 4 K) and the deposition must be slow enough to prevent pressure in the target vacuum from rising above 10^{-6} Torr. If the pressure strays too far above this value, heat conduction from the 100 K shield occurs and the entire target can sublimate in a few seconds. It is essential for the cryostat to have a high cooling power to allow quick deposition of a target. The measured cooling power of

the cryostat at 3 K is $\sim$ 100 mW, large enough to freeze about one liter of hydrogen to the target foil in 1/2 hour [51].

A schematic drawing of the target foils after gas deposition is shown in Fig. 3.6. The gold foils (**a**) shown are separated by 17.9 cm. The incoming muons enter through the US (upstream) gold foil. The upstream formation and emission layer is deposited onto the US foil and consists of $H_2 + 0.1\%\ T_2$ (**b**). A frozen layer of D_2 (**c**) placed over the first layer acts as an energy moderator for the emitted $t\mu$ atoms. The reaction layer (**d**), consisting of HD, is placed on the DS gold foil.

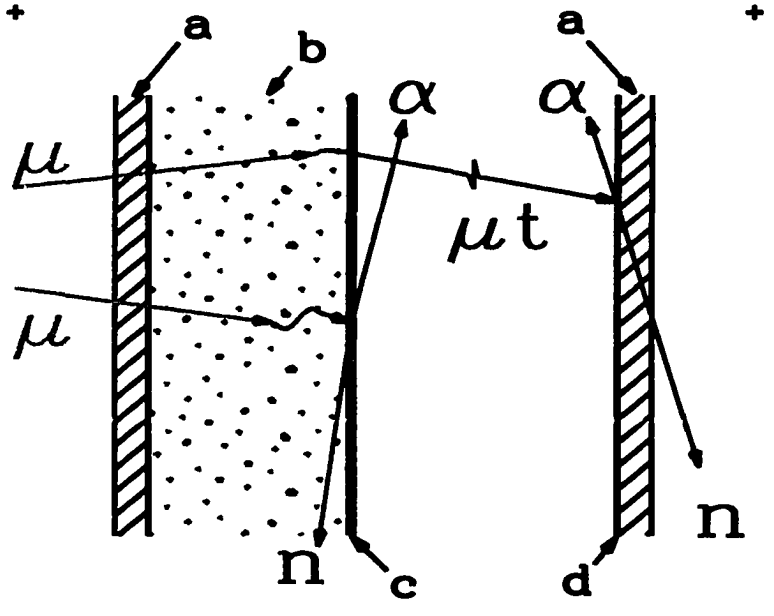

Figure 3.6: *A schematic drawing of the gold target foils with frozen hydrogen isotopes placed on them. Shown are the two gold foils (labelled* **a**), *the upstream formation and emission layer* $H_2 + 0.1\%\ T_2$ *(labelled* **b**) , *the moderation layer* (D_2) *(labelled* **c**), *and the downstream reaction layer* (HD) *(labelled* **d**). *Note that the horizontal spacing is not to scale.*

To maintain the same solid target for up to a week a 500 l dewar of liquid helium was required. The long duration permitted the study of physics reactions occurring with low event rates. The liquid helium consumption rate was $\sim$ 2.5 l/h. A pressure of $\sim 10^{-7}$ Torr was achieved in the target area at room temperature by pumping the apparatus with a magnetic levitation turbo pump. Because of the large surface area of the thermal shield the cryostat, when cold ($\sim$ 3 K), pumped more rapidly than the turbo pump. Under these conditions a vacuum of 10^{-9} Torr was maintained in the target area and the turbo pump was isolated from the vacuum space [51].

3.2.4 Tritium Safety

Because the experiments were conducted with the radioactive isotope tritium, a major consideration for the construction of the target was compatibility with tritium. Tritium exposure to the experimenters and contamination of the apparatus needed to be minimized. Steps were taken to ensure that the entire system was leak tight and a secondary enclosure was placed surrounding the apparatus in case a leak developed. Contamination considerations required that no compounds containing hydrogen be used in the construction of the target because tritium can take the place of protium through replacement reactions and contaminate the apparatus. Tritium decays by the reaction $t \rightarrow {}^3\mathrm{He} + \beta^- + \overline{\nu}$ and the beta particle can act as a catalyst to cause exchange between protium bound in the compound and the free tritium [4]. An all-metal construction minimizing the use of elastomers satisfied the safety requirements.

3.3 Data Collection and Electronics

The detector signals were processed by NIM and CAMAC electronics. A CAMAC STARBURST processor was used to read the digitized data which was then sent to a VAXstation. The VDACS data acquisition system developed at TRIUMF was used for data collection and transfer to 8 mm EXAbyte storage tapes. The data histogramming program MOLLI (also developed at TRIUMF) was used to create histograms for data analysis.

Figure 3.7 is a diagram of part of the electronic logic used in the experiment and Fig. 3.8 depicts the timing of the critical modules. The entire electronic diagram is referred to as the trigger circuit. Note that the logic notation in the diagram defines an overline on a symbol as "not". Incoming particles pass through and deposit some energy in a thin scintillator T1 (the muon beam counter) near the beam entrance window. At a beam momentum of 27 MeV/c, the incoming muons are nonrelativistic and strongly ionizing. The T1 threshold is set to detect these muons and ignore events due to electrons. This is done by increasing the threshold on T1 to allow all signals from muons to pass the threshold condition while signals due to electrons are below threshold. When a muon has passed through the entrance scintillator and deposited sufficient energy to pass the energy loss cut, a pileup gate (PUG) busy (B) output is locked on for 10 μs ($\overline{\text{B}}$ is off for 10 μs). If a second muon arrives during this time, it is considered as a pileup event and the busy output which is already locked on is extended to 10 μs after the arrival of this later muon. An event gate (EVG) opens to accept a fusion event candidate when T1 fires, there is no pileup($\overline{\text{B}}$), and STARBURST and VDACS are able to accept data ($\overline{\text{I}}$). Referring to Fig. 3.7, this is symbolized by the coincidence $\text{T}\overline{\text{BI}}$, sent into $\text{T}\overline{\text{BI}}\text{F}$ which opens the event gate EVG. The fanned-out coincidence $\text{T}\overline{\text{BI}}\text{F}$ provides the start signal for the CAMAC TDCs. The event gate signal EVGF is sent to all detectors (as described in the next section). When any detector, n, records an event while EVG is open, the detector gate TRGn is opened. The end of the event gate (EEVG) is

placed in coincidence with the logical sum of all TRGn trigger detector events to determine if there was an event trigger (EVTR). When an EVTR occurs, the hardware inhibit (HINH) is immediately activated to prevent loss of data already measured. This inhibit disables the $T\overline{BI}$ coincidence and is maintained while the data is read and modules cleared. An event-clear signal EVCL (no coincidence between detector trigger and event gate) would activate the clear pulse inhibit (CPINH), and TDCs and ADCs would be cleared of any accidental recorded values.

To determine that the detectors and electronics are functioning correctly during the experiment, scalers record the values and frequencies of certain events. Among these scalers are T1, $T\overline{BI}$, EVCL, EVTR, and TRGn. The good-muon scaler (GMU) is important (see below) and is incremented each time an EEVG is in coincidence with EB (see Fig. 3.8). The end-of-busy-gate, EB, signal in coincidence with the end-of-event-gate, EEVG, signal implies there is no pileup and the "muon" is referred to as a good muon. The GMU scaler gives the number of nonpileup muons because, if a second muon triggered T1, the $\overline{B}$ gate would have extended beyond 10 μs, and the EB signal would no longer be in coincidence with EEVG (see Fig. 3.8).

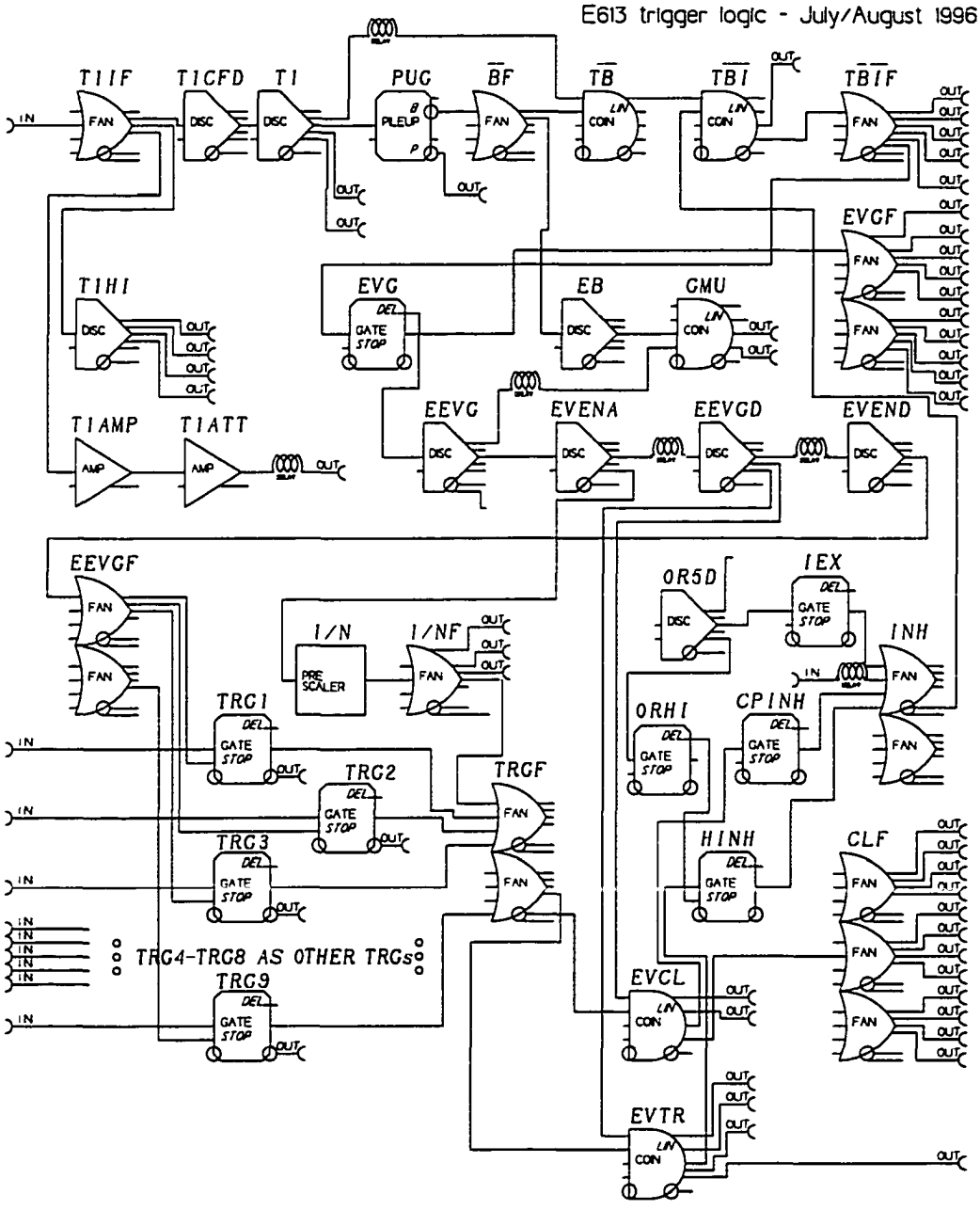

Figure 3.7: *The electronic schematics of the trigger circuit. The input to T1IF comes from the beam entrance scintillator T1. The inputs to all trigger signals are supplied by various detectors and labelled as TRG1 through TRG9.*

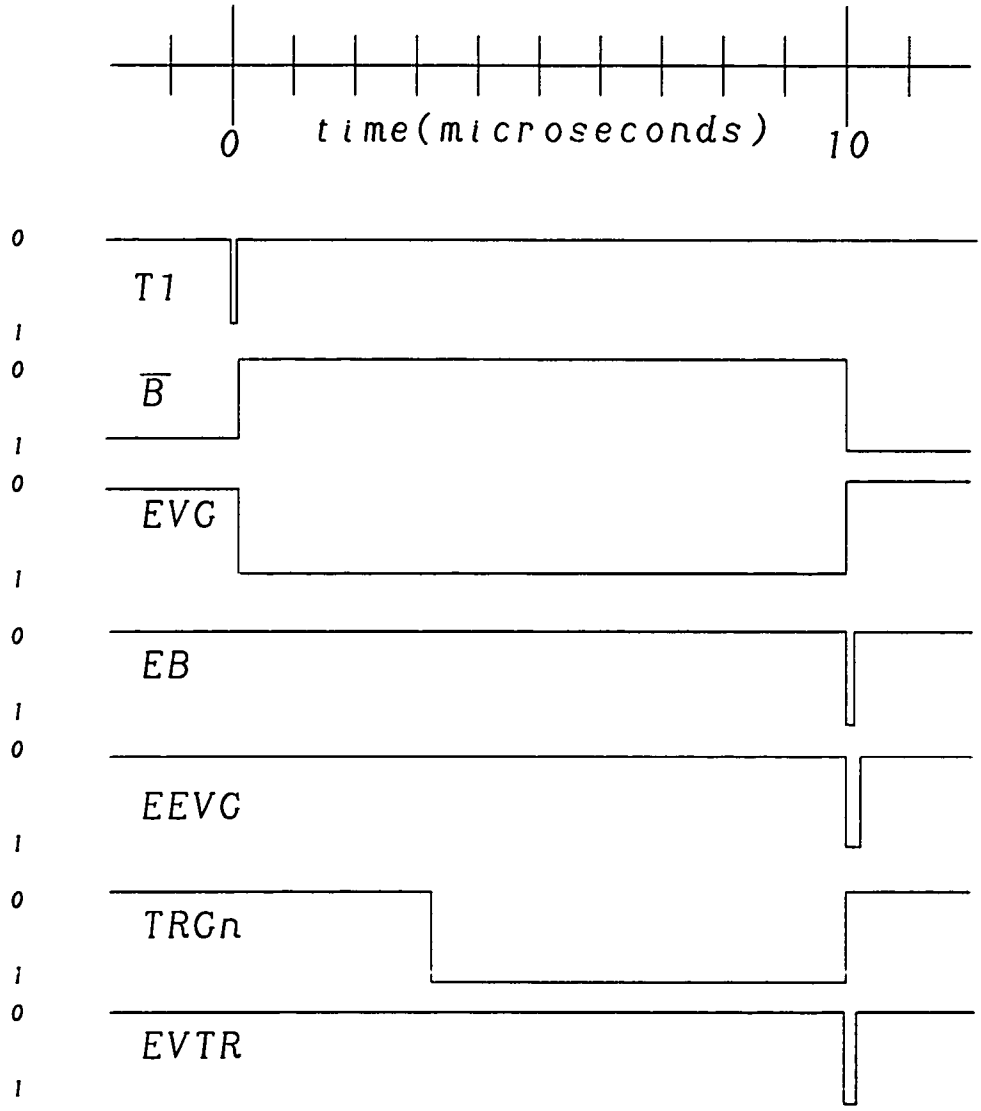

Figure 3.8: *The electronic timing for the main trigger circuit logic. A zero represents the gate as closed while a one implies the gate is open. Pulse widths depicted as less than 1 μs are for illustrative purposes only. Notice that the event gate EVG opens when the signals from T1 and pileup gate busy* $\overline{\text{B}}$ *are in coincidence. The end of the event gate (EEVG) fires when EVG closes. If EEVG and EB are not in coincidence then a possible pileup event has occurred. When EEVG coincides with the detector trigger TRGn, it produces a coincidence in the event trigger, EVTR.*

The GMU scaler is used to normalize different data sets for comparison as it keeps track of the number of muons per run which contribute to recorded fusion events. The GMU value permits comparisons of different runs despite fluctuations in beam intensity. Under identical experimental conditions, the ratio of GMU to any other type of event (fusions, muons stopping in the Au foil, *etc.*) should remain constant. As a consistency check on the electronics, the GMU scaler can be predicted from other recorded scaler values by using the following relation:

$$\mathrm{GMU} = \mathrm{T\overline{BI}} \times \left[\frac{\mathrm{T\overline{BI}}}{\mathrm{T1}} \times \frac{\mathrm{MON}}{\mathrm{MON} \cdot \bar{\mathrm{I}}} \right] \quad . \tag{3.1}$$

This relation is derived through the following reasoning. A difference exists between GMU and $\mathrm{T\overline{BI}}$ because a muon pileup may occur after the muon which generated the T1 event. In this case, GMU is not recorded but $\mathrm{T\overline{BI}}$ is. In order to calculate GMU from $\mathrm{T\overline{BI}}$ we must multiply $\mathrm{T\overline{BI}}$ by the factor given in brackets in Eq. (3.1). This factor represents the fraction of events which do not have a muon pileup. The fraction of events which do not have a muon pileup is also given by $(\mathrm{T\overline{B}})/(\mathrm{T1})$ since, when a muon pileup occurs, it is recorded in T1 but not in $\mathrm{T\overline{B}}$. Unfortunately, $\mathrm{T\overline{B}}$ is not a scaler which is recorded during the experiment. But, the fraction of events which do not have an inhibit is given by $(\mathrm{T\overline{BI}})/(\mathrm{T\overline{B}})$ or equivalently by $\mathrm{MON} \cdot \bar{\mathrm{I}}/\mathrm{MON}$ and these scalers are recorded during the experiment. By using this equivalency, the unknown scaler $\mathrm{T\overline{B}}$ was transformed by multiplication into the factor given in brackets in Eq. (3.1).

3.4 Detectors

To measure the neutrons, alpha particles, x rays, muons, muon decay electrons, *etc.*, occurring in the experiment, various detectors were used. The detector arrangement is shown in Fig. 3.9. For each EVTR condition, the status of every detector was monitored by reading

all signals coming from the detectors, not just the triggered detector. This ensured that all electronics were cleared before another EVTR signal occurred.

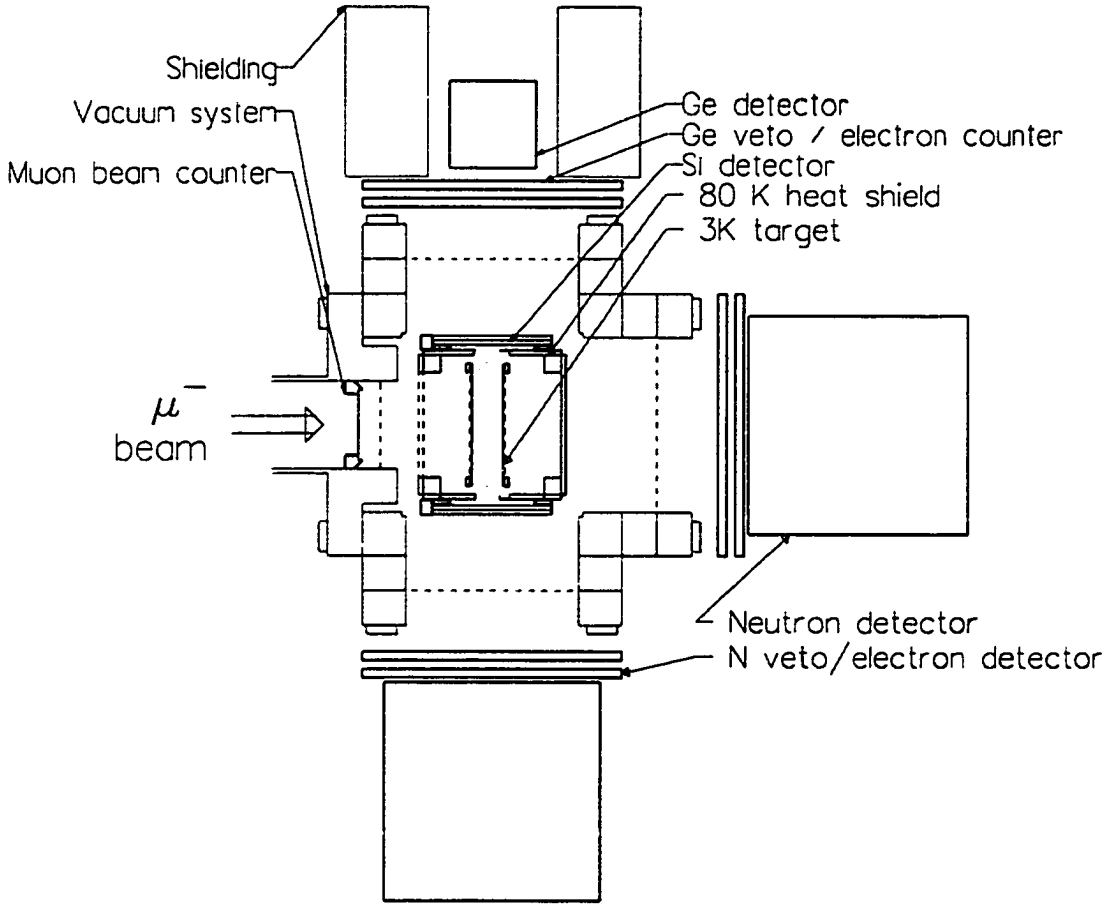

Figure 3.9: *A top view of the detector setup around the target. The incoming muon beam shown strikes the upstream target foil first. Neutron detector N1 is placed downstream of the target foils while N2 is placed to the right of the incoming muon beam.*

3.4.1 Silicon Detectors

Charged Particle Detection

Two silicon charged particle detectors purchased from Canberra Industries Inc. were used to detect the 3.5 MeV alpha particles produced by $dt\mu$ fusion. They were mounted on both sides of the thermal shield, perpendicular to the target foils. Both detectors used had an active area of 2000 mm^2 with a nominal depletion depth of 300 μm. The bias voltage placed on silicon detector 1 (Si1) was 40 V and on silicon detector 2 (Si2) was 110 V.

The silicon detectors used were Passivated Implanted Planar Silicon (PIPS). Ion-implanted junctions were formed in the semiconductor crystal by bombarding it with a beam of acceptor ions to form p-type silicon (having an excess of hole carriers) at the surface [55]. At the junction between the implanted region and the normal region, there is a repulsion of majority charge carriers such that a depleted region exists. The difference in concentration of holes and electrons between the two regions causes diffusion across the junction. An electric field gradient across the junction will eventually stop the diffusion and the result is a region of immobile space charge. This area of changing potential is called the depletion zone and is free from mobile charge carriers [56]. By applying a reverse-bias voltage to the junction (a negative voltage to the p side), the holes in the p region will be attracted towards the p contact (away from the junction). The net effect is that the depletion zone, which is the region sensitive to radiation, is enlarged. Ionizing radiation which enters this region will create electron-hole pairs which are swept out by the electric field created by the gradient. A current signal proportional to the ionization can then be detected.

Silicon Detector Electronics

The schematic diagram for the silicon detector electronics is shown in Fig. 3.10 for silicon detectors Si1 and Si2. The current signal from detector SiN (N=1,2) was collected by a charge-sensitive preamplifier and then sent to a linear shaping amplifier which amplified the signal while preserving the proportionality of input and output signal amplitudes. Pulse height information then allowed a determination of the energy of the detected particles. The preamplified signal was also sent through a timing filter amplifier and constant fraction discriminator into the discriminator SiNT to obtain timing information. The delayed signal from SiNT was placed into coincidence with the event gate fan out (EVGF) to form a silicon detector trigger. The trigger signal was then sent to CAMAC scalers, a TDC unit, and a TRGn gate (see Fig. 3.8).

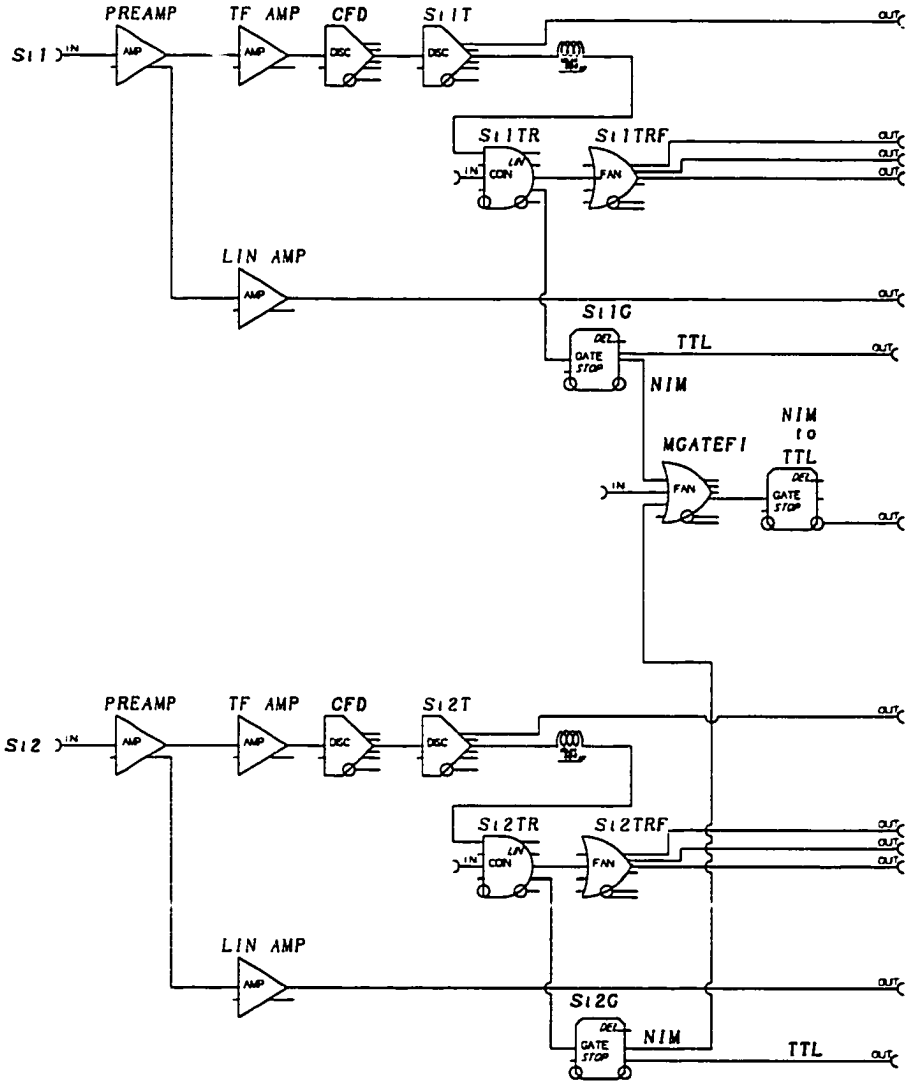

Figure 3.10: *The electronics diagram for the silicon detectors Si1 and Si2. The electronics contained in the dashed box were located beside the M20B experimental area, close to the location of the detectors to reduce electrical noise. The energy and time signals were sent to the counting room where coincidences with EVGF were employed to stop the TDC and open the gate on the ADC to record the energy signals.*

3.4.2 Neutron Detectors

Neutron Detection

Neutrons produced by $dt\mu$ fusion were detected by two enclosed cylinders of NE213 liquid organic scintillator five inches in diameter by four inches in depth. Two scintillator paddles connected to two photomultipliers were placed in front of each neutron detector. The scintillators were used to veto incoming charged particles. A method is needed to distinguish between the uncharged neutrons and photons. The liquid scintillator NE213 was used because of its pulse shape discrimination properties. Pulse shape provides a method to distinguish the event types based on the interactions of the particles and the scintillation properties of the detectors.

The non-vetoed interactions occurring in the neutron detectors are due either to a photon or to a neutron. A photon will scatter from the electrons in the NE213 material by a Compton process, transferring some of its energy to the recoil electron. Incoming neutrons however, interact only with nuclei in the NE213 scintillator. NE213 has a high ratio of hydrogen to heavier elements (the H/C atom ratio is 1.213) so there is a resonable probability of an incoming neutron interacting with a single proton [57]. The recoiling proton in the (n,p) scattering process can interact with electrons in the NE213, causing excitations which produce scintillations and signals in the detector.

Pulse-shape discrimination (PSD) techniques were employed to distinguish between the light emission curves for Compton scattered electrons and for recoil protons, both of which lose energy in the scintillator. The light pulse produced by a slowing electron has a different time structure than that produced by a slowing proton and it is this time structure which is exploited to distinguish neutrons from photons [56]. This difference in time structure is due to the fast and slow time decay components of the light pulse arising from the deexcitation of different states in the NE213. A Link Systems PSD-5010 was used to determine if the

produced light pulse was due to a gamma ray or a neutron entering the detector. The PSD-5010 integrates the signal pulse over two time ranges (a shorter interval of $\sim$ 50 ns and a longer interval of $\sim$ 500 ns) both of which start at the beginning of a pulse. The short interval contains most of the signal produced by gamma rays as the slowing Compton electrons will deposit energy quickly. The long time interval will not only include the signal produced by the slowing electrons but also much more of the signal produced by the slowing proton. The PSD value is the weighted difference of the two time integrals of the signal and gives a quantitative measure of the pulse shape [56]. The PSD value for gamma rays will be close to zero as most of the energy was deposited quickly. For neutrons, this is not the case thus the PSD value will not be close to zero. It is this value which tells us what entered the detector— a neutron or a gamma ray.

Neutron Detector Electronics

A schematic drawing of the electronics for neutron detector N1 is shown in Fig. 3.11. The two signals (E1N1, E2N1) from the pair of charged-particle scintillators placed in front of the detector were used to form an anticoincidence (GN1) with the signal from the neutron detector. The condition $GN1 = \overline{E1N1} \cdot \overline{E2N1} \cdot N1$ (where "$\cdot$" signifies the Boolean "AND") implied the particle detected in N1 carried no charge. The event gate fan out (EVGF) signal along with the time delayed signal from GN1 formed a neutron trigger N1TRG. The signal from N1TRG starts a 10 μs gate which imposes a veto on the neutron trigger as soon as the trigger signal passes through the gate. This prevents a second neutron signal from getting through in this time. The trigger signal was passed to a gate generator (ADC GATE on Fig. 3.11) and the gate signal was sent to the ADC, enabling the energy signal from the neutron detector to be digitized. The PSD voltage was also sent to another channel of the ADC but was first sent through a level adapter (PSD SHIFT) to shift the signal into the

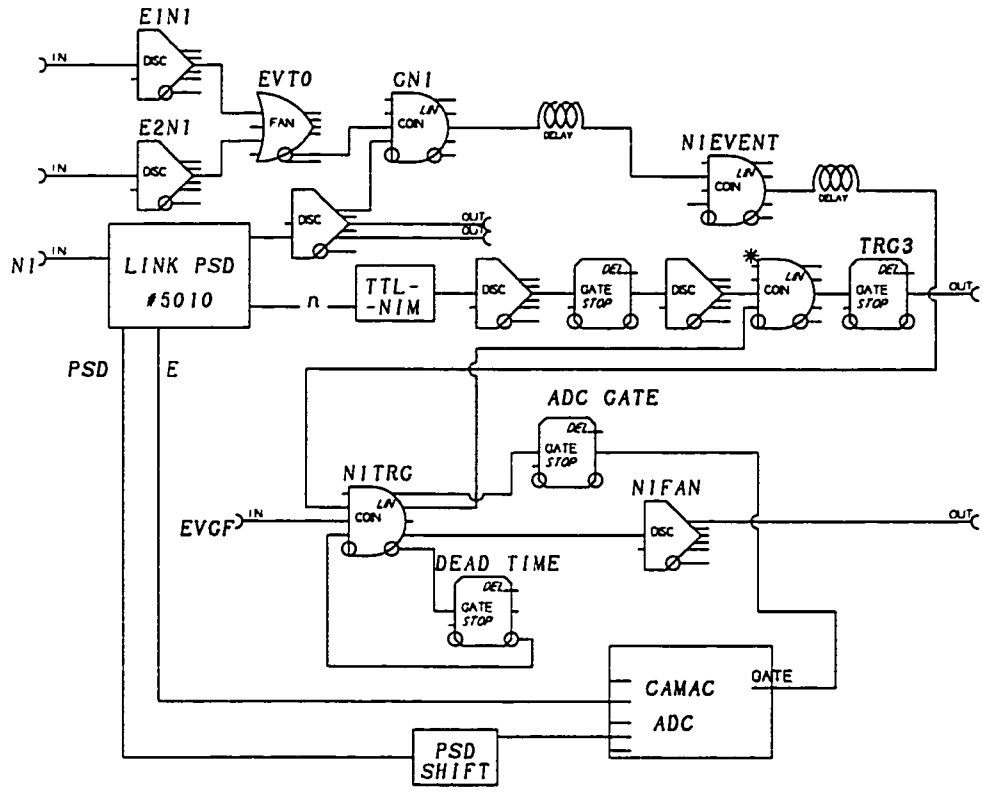

Figure 3.11: *The electronics diagram for neutron detector N1. The inputs E1N1 and E2N1 are from the charged particle veto scintillators in front of neutron detector N1 (see Fig. 3.9). The * depicts the place in the logic where the neutron signal from the PSD 5010 can be removed for calibration purposes.*

range accepted by the ADC.

3.4.3 Germanium Counter

A germanium detector was used to detect muon-related atomic cascade x rays generated from muon transfer to high-Z nuclei as well as gamma rays from nuclear capture. The detector was used to examine the purity of the target gases and proved invaluable during efforts to purify the HD gas. The spectrum obtained during the experiment was used to

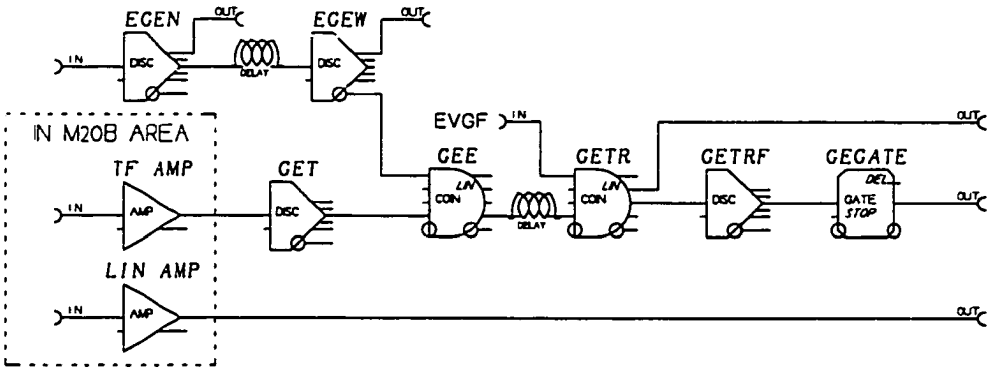

Figure 3.12: *The electronics schematic for the germanium detector. The setup was similar to that of the silicon detectors (see Fig. 3.10) except for the requirement that the signal from the detector be in anticoincidence with the signals from charged particle scintillators.*

determine x rays from any impurities present in the target. These impurities because of their high atomic number could quickly capture muons in the target through muon transfer reactions from muonic hydrogen atoms. The germanium detector was calibrated using a ^{182}Ta x ray source. From this calibration, the FWHM of the energy peaks in the detector was found to be 9.5 channels and the energy calibration was determined to be 0.127(1) keV/channel with a 5.6 $\pm$ 7.3 channel offset. Peaks in the germanium spectra for the HD gas were fit by a Gaussian curve with a mean fixed at 800 channels (corresponding to x rays from nitrogen) and width of 9.5 channels, plus a flat background. The upper limit of counts in the Gaussian was normalized to the number of good muons in the target (along with the detector efficiency of 0.1%). This number was compared to a Monte Carlo simulation in which various concentrations of nitrogen impurities had been input. When the number of muon transfers to nitrogen reached the value determined in the experimental peak an upper limit on the nitrogen contamination of the HD target was determined. The nitrogen contamination of the HD target was found to have an upper limit of 0.1% within a one

sigma confidence level (68%).

The germanium detector signal was placed in anticoincidence with signals from charged veto scintillators. As the germanium detector was used strictly to detect x rays, any charged particles travelling through the scintillators which could possibly strike the germanium detector (due to background events or reactions in the target) were vetoed. The detector was shielded from background events in M20B by enclosing it in a 1.5″ thick copper cylinder, which in turn was inside a 1.5″ thick tungsten cylinder (see Fig. 3.9).

An electronic schematic of the germanium detection system is shown in Fig. 3.12 and is clearly similar to the silicon detector electronics (see Fig. 3.10). To determine energy information on the interaction which triggered the detector, the output current pulse from the detector was passed through a linear amplifier in order to determine pulse height information, before being digitized. To determine timing information the pulse was passed through a timing filter amplifier and discriminator to make an anticoincidence with the charged particle scintillator. The delayed anticoincidence GEE was placed in coincidence with the event gate fan (EVGF) signal and used to determine when the ADC gate and TDC stop were activated to record the event.

3.4.4 Electron Counters

The plastic scintillators discussed in section 3.4.2 were also used to detect electrons produced by muon decay. The schematic of the electronics for the scintillators in front of neutron detector N1 is shown in Fig. 3.13. Signals from scintillators E1N1 and E2N1 were brought into coincidence and passed through to EN1 where the time of a muon decay electron ($\mu^- \rightarrow e^- + \overline{\nu}_e + \nu_\mu$) detected by these scintillators was recorded by a TDC.

In order to reduce background events coming from nuclear muon capture ($\mu^- + (N, Z) \rightarrow (N+1, Z-1) + \nu_\mu$) where N represents the number of neutrons in a nucleus and

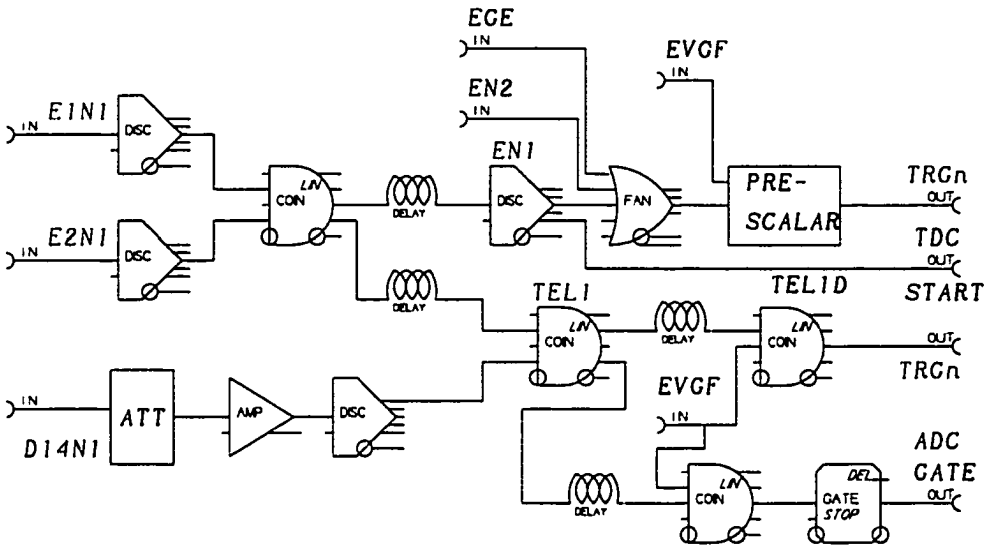

Figure 3.13: *The electronic diagram for the del-e and del-tel logic circuit showing the signals from N1, E1N1 and E2N1. Coincidence signals from the remaining charged particle scintillators are depicted as inputs EGE and EN2.*

Z the number of protons) the electronics were set to detect the muon decay electron after the candidate fusion event. This section of the electronics is called the del-e or delayed electron coincidence. A del-e event is a muon decay electron coincidence delayed in time with respect to the candidate fusion event (del-e events will be discussed in detail in section 4.5.2). The electronics consist of the signals EN1, EN2 and EGE (signals from the veto counters in front of N1, N2 and the germanium detector) fed into a fan-in unit. When a signal was provided by EVGF, a del-e trigger signal was produced for every fourth event (prescaler set to 1:4 due to large statistics).

A dynode signal from the neutron counter photomultiplier was used as a fast independent signal from the detector. After being attenuated and amplified, this signal was placed into coincidence with E1N1 and E2N1 to determine an energy signal from a charged particle. The TEL1 signal was then delayed and placed in coincidence with the EVGF to

provide a del-tel (delayed telescope) trigger. The digitized amplitude of the dynode signal gave a measure of the energy deposited due to the charged particle [56].

As we have seen in this chapter, the apparatus and electronics needed to perform muon catalyzed fusion experiments are quite detailed and involved. The experiment requires many people to execute and is not a project that could succeed without a great deal of man power. While most of the information proved to be invaluable during the course of data analysis, some of the precautions and data taken turned out to be unnecessary, as we will see in the upcoming chapter.

Chapter 4

Data Analysis

4.1 Experimental Data Runs

The experimental data were collected over a three week period during July and August in 1996. In Table 4.1 the solid target characteristics are given; we have to pay special attention to the location of the target (upstream US or downstream DS), the thickness measured in Torr·liter[1], and the composition. Due to the wide use of this thickness unit throughout the thesis the abbreviation of Tl will be used from this point forward. The conversion value between Tl and thickness in mm was previously measured using the energy loss of alpha particles traversing the layer [52], and the calculation will be discussed in section 4.2.3.

[1]The amount of gas in a one liter volume at one Torr at ambient temperature (20 $^{\circ}C$).

Run #	Target Type US (Tl)	DS (Tl)	Elapsed time (hrs)	GMU (10^6)
1898-1899	SET(1000 $H_2 + 0.1\%T_2$)	-	5.3	49.2
1900	SET	10 D_2	1.7	15.4
1901-1902	SET	(10+5=15) D_2	0.5	0.5
1903	SET	(10+5+5=20) D_2	2.4	21.3
1908	SET $\oplus$ 3 D_2*	(10+5+5=20) D_2	2.4	23.4
1910	SET $\oplus$ (3+3+4=10) D_2*	(10+5+5=20) D_2	2.7	22.4
1911-1912	SET $\oplus$ (3+3+4+4=14) D_2*	(10+5+5=20) D_2	4.6	36.0
1944-1945	SET(1000 $H_2 + 0.1\%T_2$)	-	4.6	22.1
1946-1947	SET $\oplus$ 3 D_2	-	1.1	7.7
1948	SET $\oplus$ (3+5=8) D_2	-	0.7	5.0
1949-1956	SET $\oplus$ (3+5+2=10) D_2	-	29.6	220.3
1958-1969	SET $\oplus$ (3+5+2=10) D_2	3 HD	70.8	565.8
1970-1971	SET $\oplus$ (3+5+2=10) D_2	(3+4=7) HD	6.9	55.8
1973-1974	SET $\oplus$ (3+5+2=10) D_2	7 $HD \oplus$ 20 D_2	10.3	79.6
1975-1976	SET $\oplus$ (3+5+2=10) D_2	7 $HD \oplus$ 20 $D_2 \oplus$ 300 HD	7.7	62.9
1977-1979	SET $\oplus$ (3+5+2+4=14) D_2	7 $HD \oplus$ 20 $D_2 \oplus$ 300 HD	8.2	68.2

Table 4.1: *Summary table of the targets for emission data. Also given are the Good MUon (GMU) scalers (see section 3.3). All thicknesses are in Tl. The Standard Emission Target (SET) is 1000 Tl of a tritium doped protium mixture with a tritium concentration of* $c_t = 10^{-3}$. *The* $\oplus$ *is used to indicate that the* D_2 *layer was frozen on the surface in the increments summed in brackets. The * indicates runs in which there may have been some difficulties with gas deposition–see the text for details.*

A summary of emission data runs used in the analysis is given in Table 4.1. In each case a Standard Emission Target (SET) of 1000 T*l* protium with a tritium concentration of $c_t = 0.1\%$ was deposited onto the upstream gold target foil. Muons stopped in the SET layer then participate in the physics processes discussed in Chapter 2. Runs 1898-1899 and 1945-1946 consisting solely of an US SET target are used as background runs because no dt fusion occurs in the target. The target thicknesses were chosen to begin with a minimal amount of deposited gas and were slowly increased by depositing more gas on top in order to perform time efficient measurements on the same SET. Since a target can be maintained for approximately one week, runs 1898-1912 come from one SET target and runs 1944-1979 contain another SET target. Runs 1900-1912 were taken in order to study $dt\mu$ molecular formation occurring in the D_2 moderation layers. The additional layers of D_2 were chosen to be identical to targets used for data taken in a similar run during 1994. However, due to some difficulties with gas deposition, less gas was deposited onto the target foils than had been planned. These problems are taken into account and corrected for in section 4.7. Runs 1949-1956 are used to study fusion occurring in the US target. These runs will also be used as a background for determining fusion occurring in the DS target in the subsequent runs from 1958-1969 to 1975-1976. These last runs used a solid HD target downstream and thus fusion from $dt\mu$ molecular formation on HD can be investigated. Note that changing the thickness of the D_2 overlayer on top of the SET changes the energies with which the $t\mu$ atoms are emitted from the overlayer, thus providing us with several different energy distributions with which to test the theoretical cross sections. The majority of data taken was with a D_2 moderation layer at a thickness for which the escaping $t\mu$ will reach the DS target at an energy favourable for molecular formation.

Histogram creation for data analysis was done using MOLLI [59] (Multi OffLine Interactive analysis) which was developed at TRIUMF. The MOLLI program read the data

from tape and then processed it by a user-defined subroutine which created the required histograms. These histograms were saved in Fiowa format (also developed at TRIUMF) [60] so they could be accessed by either the Replay viewing package [61] or the Physica analysis package [62].

4.2 Detector Calibration

Calibrations of both neutron and silicon detectors were used to define the energy scale for 14 MeV fusion neutrons and 3.5 MeV alphas. Table 4.2 is a summary of the neutron and silicon detector calibration runs for the July and August 1996 experiment.

Run #	Detector	Source	Interval Between Calib. (hours)	Americium Peak Position	
				Si1	Si2
1885	Neutron	^{60}Co	—	n/a	n/a
1887	Neutron	^{137}Cs	—	n/a	n/a
1931	Si1 & Si2	^{241}Am	—	5481.7(3)	5483.2(3)
1933	Si1 & Si2	^{241}Am	0.05	5482.1(3)	5483.1(3)
1934	Si1 & Si2	^{241}Am	0.4	5482.2(2)	5485.3(2)
1957	Si1 & Si2	^{241}Am	68.7	5484.8(3)	5478.7(3)
1972	Si1 & Si2	^{241}Am	85.7	5483.8(3)	5481.2(3)
1981	Si1	pulser	31.3	5483.5(2)	n/a
1982	Si2	pulser	31.3	n/a	5489.4(3)

Table 4.2: *Summary table for the neutron and silicon detector calibration runs. The silicon detectors were calibrated throughout the course of the experiment. The last two columns give the channel number of the 5.486 MeV alpha peak from americium.*

4.2.1 Silicon Detectors

Calibration data for both silicon detectors (Si1 and Si2) were taken by using a precision pulser and two small americium sources. Sending a precision pulser signal of various amplitudes to each silicon detector preamplifier for a defined time produced the spectrum shown

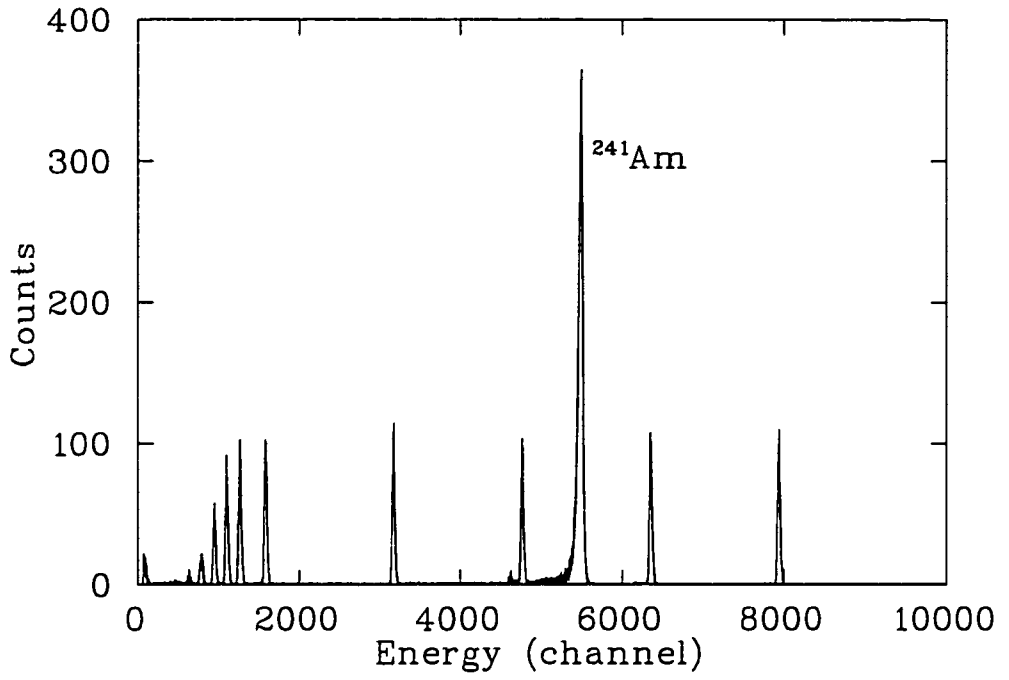

Figure 4.1: *The pulser and americium spectra in silicon detector 1 (Si1). All peaks less than or approximately at 100 counts are due to the pulser. The large peak is from the americium source and corresponds to an alpha particle energy of 5.486 MeV.*

in Fig. 4.1. The positions of the pulser peaks give a measure of the electronic linearity while the widths of the pulser peaks measure the effect of the electronics on the detector resolution. Since the centroid values of the peaks define a linear scale, they allow the origin of the energy scale to be accurately determined. The centroid values for Si1 are given as an example in Table 4.3.

Two ^{241}Am sources were placed on top of the gas diffuser, each one facing a silicon detector. They were mounted on the diffuser to allow them to be withdrawn when fusion measurements were made so no contamination of the silicon spectra occurred. Americium decays by alpha emission and 86% of the alphas have an energy of 5.486 MeV [63]. The peak from ^{241}Am is shown in Fig. 4.1 and is used to determine an absolute scale for the

Pulser Amplitude	Centroid(channels)	σ(channels)
40	630.9 ± 1.4	17
50	788.2 ± 0.6	17
60	949.3 ± 0.4	13
70	1105.3 ± 0.3	12
80	1266.3 ± 0.3	14
100	1585.3 ± 0.4	14
200	3175.0 ± 0.4	14
300	4766.0 ± 0.3	14
400	6354.2 ± 0.2	14
500	7941.0 ± 0.2	12
intercept	-5 ± 1	

Table 4.3: *Centroid values and widths from the pulser data for Si1. The intercept value indicates where the scale begins and the σ measures the intrinsic width of the electronics.*

energy calibration.

The y-intercept listed in Table 4.3 is derived from a linear fit to the calibration data shown in Fig. 4.2. The intercept, the value of the centroid for a pulser amplitude of zero, gives the zero offset value for the detector. The calibration equations (4.1) and (4.2) for the detectors are determined by subtracting the zero offset from the centroid value of the known energy peak (from the α source). In the calibration equations for Si1 and Si2 the values in round brackets indicate the error in the final digit. The multiplicative factors are derived from the ratio of the known americium centroid energy value to the (zero offset corrected) measured americium centroid value in channels. Based on the widths of the americium peaks, the FWHM energy resolution was about 50 keV for Si1 and 53 keV for Si2 when tritium was in the target deposited on the gold foils.

$$E(Si1) = 0.998(1)\left[\frac{keV}{channel}\right]\{channel\ number + 5(1)\} \tag{4.1}$$

$$E(Si2) = 1.000(1)\left[\frac{keV}{channel}\right]\{channel\ number - 3(2)\} \tag{4.2}$$

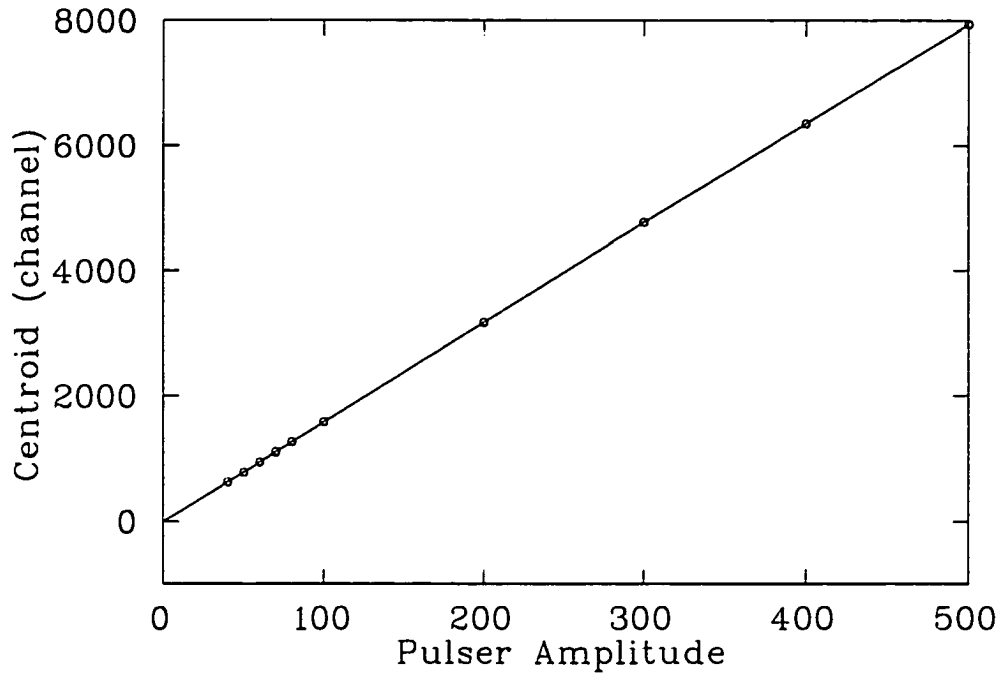

Figure 4.2: *A linear fit of the calibration data for detector Si1. The zero offset is given by the intercept between the line and channel number, corresponding to a pulser amplitude of zero.*

The solid angle of each detector was calculated by a Monte Carlo simulation. The Monte Carlo discussed in section 4.4 (SMC–Super Monte Carlo) was used. The SMC simulation, with an initial muon beam distribution which best describes the experimental muon beam, was performed for a SET $\oplus$ 10 T*l* D_2 US and bare DS target. This target was chosen because the majority of data for the July 1996 run was taken with this upstream target. The results of the simulation gave the beam distribution incident on the downstream bare target foil.

The SMC was then adapted specifically for the purpose of determining the solid angle of each silicon detector; this simulation will be referred to as SMC_{Ω}. The above generated beam distribution from SMC was then used as input into the SMC_{Ω} program and a new simulation

Source	Uncertainty	Relative Change in Ω_{Si}	Average
distance between detectors	+5 mm	−1.7 % ± 1.5 %	
	−5 mm	+2.4 % ± 1.4 %	2.1 %
collimator width	+2 mm	+1.6 % ± 1.5 %	
	−2 mm	−1.2 % ± 1.2 %	1.4 %
collimator height	+2 mm	+0.3 % ± 1.5 %	
	−2 mm	−0.2 % ± 1.5 %	0.3 %
gaussian beam FWHM	+1 mm	+0.4 % ± 1.5 %	
	−1 mm	−0.7 % ± 1.5 %	0.6 %
beam X position shift	+1 mm	−3.5 % ± 1.3 %	
	−1mm	+3.8% ± 1.3 %	3.6 %
beam Y position shift	+1 mm	−0.4 % ± 1.4 %	
	−1 mm	−0.5 % ± 1.5 %	0.5 %
Si Z position shift	+1 mm	+0.4 % ± 1.5 %	
	−1 mm	−1.3 % ± 0.7 %	0.9 %

Table 4.4: *Listed are the parameters which were varied in SMC_Ω, the amount by which they were varied, the resultant relative change in silicon detector acceptance and the average relative change in silicon detector acceptance.*

was run. Muon decay events were then histogrammed and the ones which occurred within the limits of the detector then determined the solid angle of each detector. This method was chosen as the most straightforward approach to calculating the solid angle of the silicon detectors with the assumption that the acceptance for these decay electrons is the same as the acceptance for fusion alpha particles.

In order to determine an error on the solid angle, the parameters listed in Table 4.4 were varied in the SMC_Ω program, one at a time, by the amount given in the chart. The physical distance between the detectors was varied as well as the dimensions of the copper collimator mask placed in front of each detector. Thermal contraction of the copper collimator has been taken into account by using the temperature corrected values of the collimator dimensions in all SMC_Ω runs. Thermal contraction gives an estimated 1.3% relative correction to the detector acceptance [63]. The muon beam distribution used in the program was a flat distribution with a Gaussian tail and the FWHM of the Gaussian was changed to determine

its effect on solid angle. The position of the beam spot on the target as well as the actual placement of the silicon detector along the beam axis were also varied. By defining the muon beam axis as the Z axis, the X axis is defined as the axis perpendicular to the surface of the silicon detectors and the Y axis is parallel to surface of the detectors. Shifting the beam along the Y axis in either direction was found to decrease detector acceptance as this moves the detectors out of the optimum alignment with the incoming particles. Shifting the beam closer to the detector (along the X axis) increases the acceptance because the solid angle is inversely proportional r^2, the distance between the source and the detector. Similarly, increasing the distance between the beam position and detector lowers the acceptance. Considering all the variations in the solid angle due to differences in geometry and beam distribution, the average errors have been added in quadrature and the solid angle was determined to be

$$\Omega_{Si} = (2.32 \pm 0.10) \times 10^{-2} \tag{4.3}$$

for each silicon detector.

4.2.2 Neutron Detectors

Source	Photon Energy (keV)	Compton Edge	
		(keV)	(Channel)
^{60}Co	1173,1332	963,1118	174
^{137}Cs	661	477	110
Au(3-2)	2303	2070	275
Au(2-1)	5596	5356	599

Table 4.5: *Photon energies, Compton energies, and Compton edge energies along with the corresponding channel in detector N2. Note the ^{60}Co has two lines of equal strength which are averaged to get the detector response.*

Since monoenergetic neutrons do not cause peaks in the energy spectrum, the calibration serves as a useful tool to determine the range of channels in which a 14 MeV neutron produced from $dt\mu$ fusion can be detected. Neutrons scattering from protons in the NE213 neutron detector leave an almost uniform pulse height distributed between zero and the end point energy, with zero energy corresponding to forward scattered neutrons and the end point energy corresponding to backward scattered neutrons.

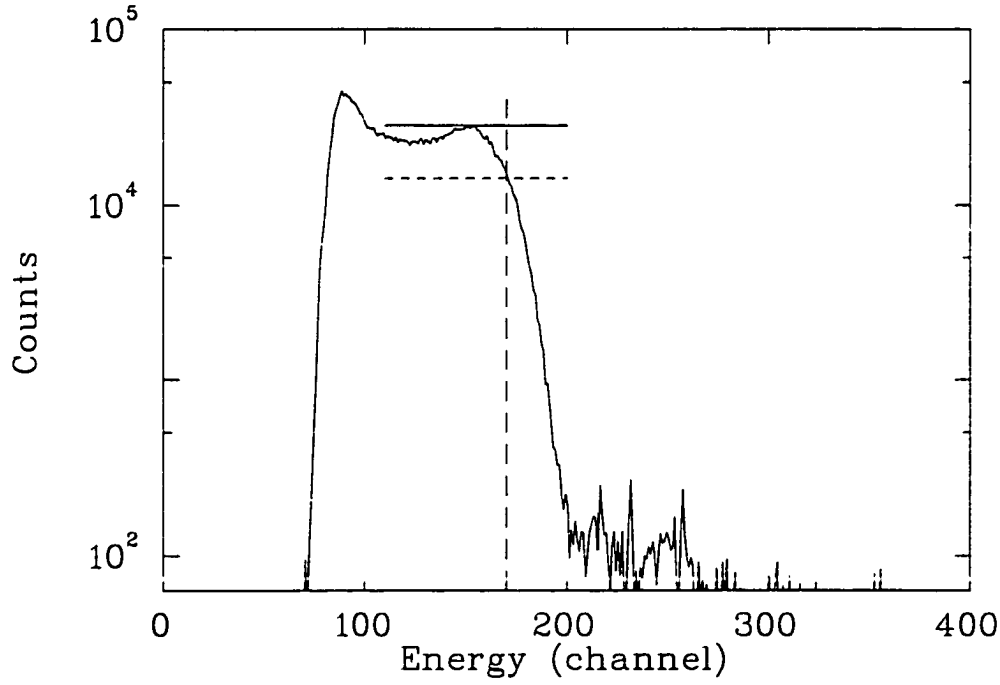

Figure 4.3: *The ^{60}Co photon energy spectrum as seen by neutron detector N2. The lines indicate the method used to find the half-height intersection point. The solid line is the effective Compton edge height. The dotted line is its half height. The intersection of the edge of the curve and the line plotted at half the average peak height determined the channel number (vertical dashed line).*

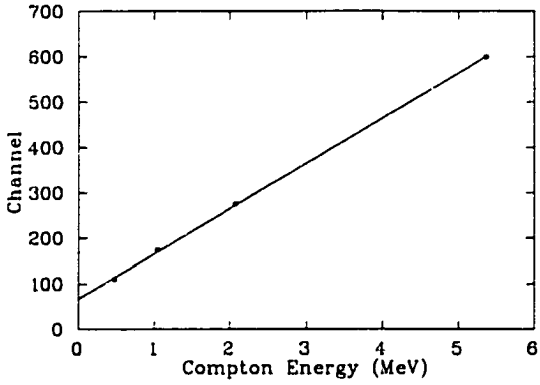

Figure 4.4: *A linear fit of the calibration data for neutron detector N2. The zero offset is given by the intercept of the line and channel number axis, corresponding to a Compton edge energy of zero.*

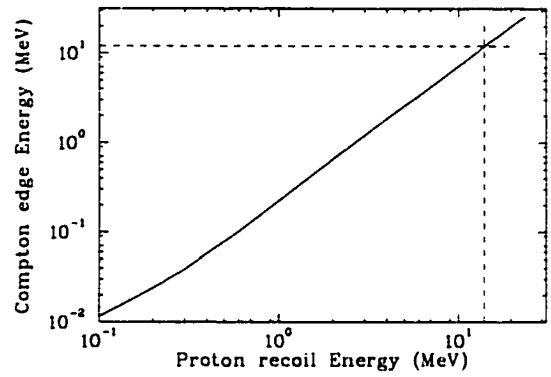

Figure 4.5: *A plot of the equivalent light output for NE213 scintillator. The data are taken from [64].*

The energy calibration of both neutron detectors (N1 and N2) was made by using the Compton edges of ^{60}Co, ^{137}Cs, and the x rays from atomic muon capture on gold. The sources, along with their energies, Compton edges, and the channel number where the Compton edge was detected are given in Table 4.5.

The energy calibration of the neutron detectors is not critically important to the experiment as the 14 MeV neutrons are quite easily identified. The calibration method [56], depicted in Fig. 4.3 is referred to as the Compton edge technique. One searches for the channel number which corresponds to the half height of the effective Compton edge (the horizontal dotted line in Fig. 4.3). The intersection of the Compton edge and the line plotted at half the average peak height determined the channel number.

To determine the calibration of the detectors, a fit of a linear function to the data shown in Fig. 4.4 gave the zero offset value for each detector. These offset values are 210 channels for N1 and 67 channels for N2. To convert gamma ray energy into the proton recoil energy

an equivalency curve relating Compton edge energy to energy response of the scintillator material (NE213) to protons was used (see Fig. 4.5). Assuming that a 14 MeV neutron transferred all its energy to a proton, the curve predicts an energy deposit equivalent to a gamma ray of energy $\sim$ 12 MeV. The equations for the gamma calibration of the neutron detectors are given below. The values in round brackets are the errors.

$$E_\gamma(N1) = 9.0(9)\left[\frac{keV}{channel}\right]\{channel\ number - 210(9)\} \tag{4.4}$$

$$E_\gamma(N2) = 15(2)\left[\frac{keV}{channel}\right]\{channel\ number - 67(4)\} \tag{4.5}$$

4.3 Target Thickness Determination

Since the uncertainty in target thickness propagates directly into the data analysis results, the thickness must be determined precisely. This then permits accurate Monte Carlo simulations of the experiment. The thickness of solid hydrogen thin film targets was previously studied in detail by M.C. Fujiwara [52] and will be only briefly summarized with more detail given to the calculation relevant to the data analysis. For a full description see [52].

To determine the thickness, the energy of alpha particles which traversed the target film was measured and converted into a range. The source of alpha particles was a linear array of five ^{241}Am sources, 3 mm in diameter, deposited onto a gold-plated copper plate (see Fig. 4.6). This plate was then cooled to 3 K and used as a target support in place of the target foils discussed in Chapter 3. The alpha particles penetrating the hydrogen film were detected by a passivated, ion-implanted planar silicon detector mounted on the frame of the gas diffuser which allowed the detector to move vertically (discussed in Chapter 3). Thus, measurements of the target thickness at different positions were done by detecting the alpha particles from each of the source spots. A collimating device consisting of an array

of small holes restricted the alpha particles striking the silicon detector to those particles originating from one source spot at a time.

By using the collimator, we can neglect the angular dispersion of alpha particles and determine the thickness of the target from the following:

$$T = R(< E_{init} >) - R(< E_{fin} >) \tag{4.6}$$

where $R(< E >)$ is the range of the alpha particle as a function of the mean energy $< E >$, $< E_{init} >$ is the initial energy of the alpha particle (with no target layer) and $< E_{fin} >$ is the energy of the alpha particle after traversing the target [52]. Because no range tables were available for $\sim$ 2-5 MeV alpha particles in solid hydrogen, a compilation for gaseous hydrogen was used [52]. The dominating uncertainty in the analysis stems from the uncertainty in the stopping power and range tables (5%). The measured film thicknesses at various distances from the center of the film for a protium target are given in Table 4.6.

Position with respect to film center (mm)	Thickness per unit gas input (μg cm^{-2} (Tl)$^{-1}$)
40	0.21 ± 0.08
30	1.52 ± 0.11
20	2.92 ± 0.17
15	3.10 ± 0.18
10	3.21 ± 0.16
5	3.33 ± 0.19
0	3.46 ± 0.17
−5	3.64 ± 0.17
−10	3.76 ± 0.19
−15	3.92 ± 0.21
−20	3.77 ± 0.19
−25	3.06 ± 0.17
−30	1.68 ± 0.09

Table 4.6: *Protium film thicknesses measured at different distances from the center of the film (taken from [40]).*

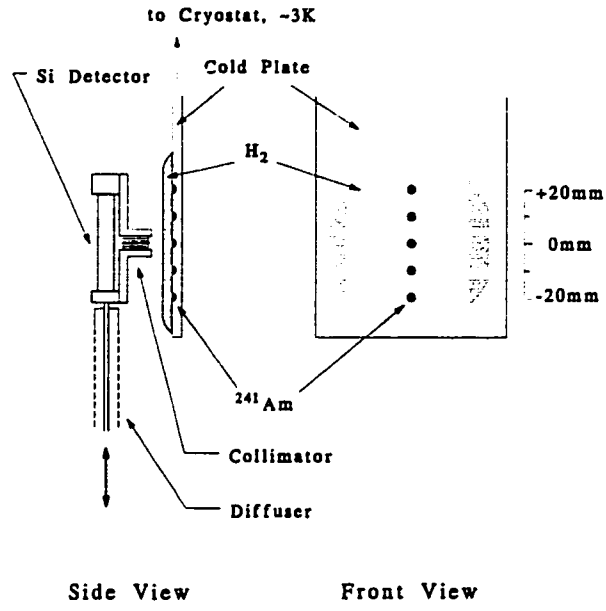

Figure 4.6: *A schematic drawing of the experimental setup used in the target thickness experiment. A solid hydrogen layer is shown frozen onto the americium source plate. Drawing taken from [40].*

The average layer thickness for a beam experiment was found to depend on the width and profile of the beam which stops in the protium target [52]. Only the vertical (Y) profile of the incoming muon beam was measured during an experiment which took place in 1993 (see Fig. 4.7) and hence the horizontal X profile must be assumed. A study of the beam profile and its effect on the effective thickness has been done by M.C. Fujiwara [65]. The effective target thickness is given by:

$$T^{eff} = \frac{\sum w_i T_i}{\sum w_i} \tag{4.7}$$

where T_i is the thickness at the *ith* measured spot and w_i is the weighting factor [52]. Because the target is being used to stop a particle beam from an accelerator, a flat-topped Gaussian distribution is used as a beam distribution [52].

To determine the effective thickness of the target during the 1996 experiment, the procedure discussed below was followed, which is very similar to the procedure discussed in [65]. First the muon beam distribution entering the target foil was parametrized. This has been done by M.C. Fujiwara [65]. The Y-distribution of muon decay electrons in the US target layer is shown in Fig. 4.7 (note: the beam axis defines the Z direction) [65]. The data points were taken from a run in November of 1993 in which a multi-wire proportional chamber system was used to track the Y position of muon decay electrons coming from the initial muon beam distribution in the XY plane. The histograms are from a Monte Carlo simulation which assumes an initial muon beam distribution of a flat-topped Gaussian. The flat-topped Gaussian is parametrized by two numbers (r,F), the first giving the flat-top radius of the beam distribution in mm and the second giving the Gaussian FWHM in mm. The histograms depict the simulated decay electron Y distribution for four different muon beam parametrizations. The four beam parametrizations used are for (8,8), (10,10), (12,12), and (15,15), flat-topped Gaussians [65]. The initial muon beam distribution which best simulates the decay electron Y distribution was a (10,10) flat-topped Gaussian.

This parametrized muon beam entering the US target was used as input to the SMC and this simulation will be referred to as SMC_{thick}. Using this initial beam distribution in the SMC_{thick} program for the present analysis, I defined the US target foil to be a SET with a 10 T*l* D_2 overlayer. Note that the DS $t\mu$ beam profile depends on the thickness of the US moderating layer since this layer changes the energy and angular divergence of the emitted $t\mu$'s [65]. Targets with different thicknesses of overlayer were studied in detail and found to have approximately a 6% effect on the effective thickness when the overlayer thickness was varied from 0 to 14 T*l* D_2.

The results of SMC_{thick} gave the number and spatial distribution of the simulated $t\mu$'s on the DS foil (see Fig. 4.8). The emitted $t\mu$ distribution is displayed as a density plot

in which the greatest number of $t\mu$'s is concentrated around the (0,0) target foil region. By sectioning the density plot into different annular disks we can determine the number of $t\mu$'s contained in each annular disk, and thus determine the weights w_i in Eq. (4.7). The annular disks were chosen to enclose the position points in Table 4.6 at which the target thicknesses were previously measured. If more than one point was enclosed in the annular disk, then an average of all enclosed points was taken to determine T_i.

It has been shown through film deposition simulations [52] that the layer thickness also depends on the distance between the diffuser surface and the target foil. A calibration factor is used to account for the difference in distance between the americium target foil and the gas diffuser in the measurements quoted in Table 4.6 versus the distance between the target foils and diffuser in the 1996 data. This scaling factor was determined to be 1.106 $\pm$ 0.034 [65]. Accounting for the scaling factor, the effective thickness of the target was found to be 3.65 $\pm$ 0.25 μg·cm^{-2}(Tl)$^{-1}$. The uncertainty in the effective thickness includes the uncertainty in the scaling factor, the 5% uncertainty in the measured target thicknesses in Table 4.6 and the statistical uncertainty on the weights w_i calculated from the SMC$_{thick}$ simulation. added in quadrature.

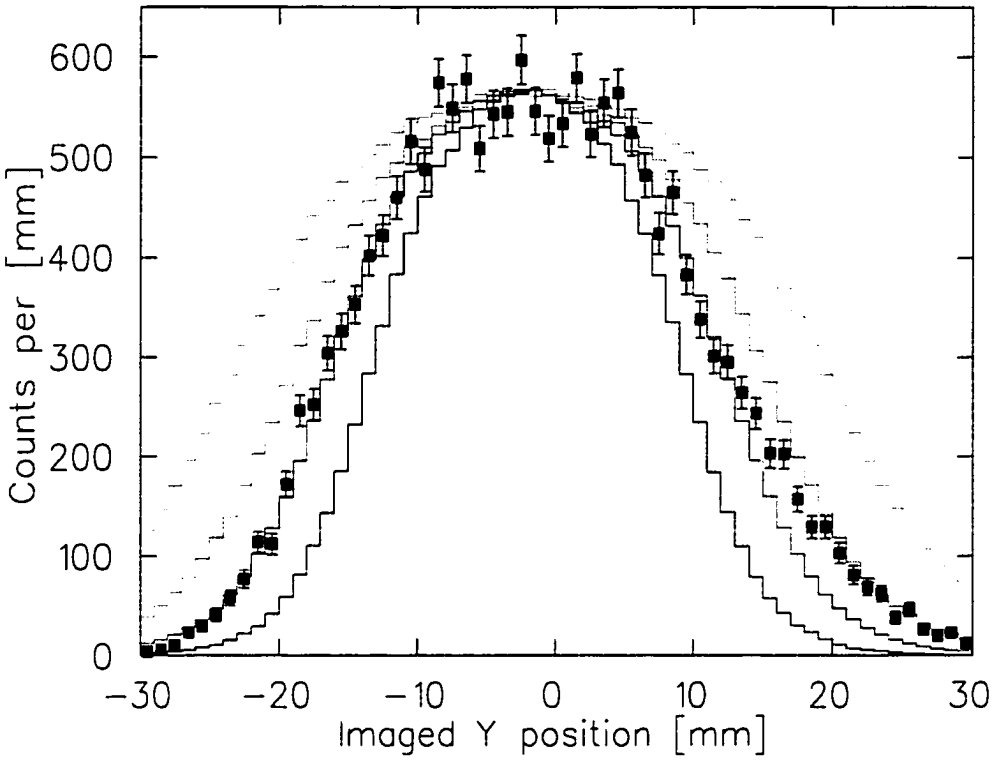

Figure 4.7: *The Y distribution of decay electrons in the US target layer. The data points were taken in November 1993 with a multi-wire proportional chamber system and the histograms are from a Monte Carlo simulation in which the muon beam distribution was chosen to be a flat-topped Gaussian. The Gaussian is parametrized by two numbers, (r,F), the first giving the flat-top radius in mm and the second giving the FWHM in mm. The histograms are for a parametrization of (8,8), (10,10), (12,12), and (15,15) (from the inner most enclosed curve moving outwards). The parametrization which best simulated the decay electron data is taken to be (10,10). These results are taken from [41].*

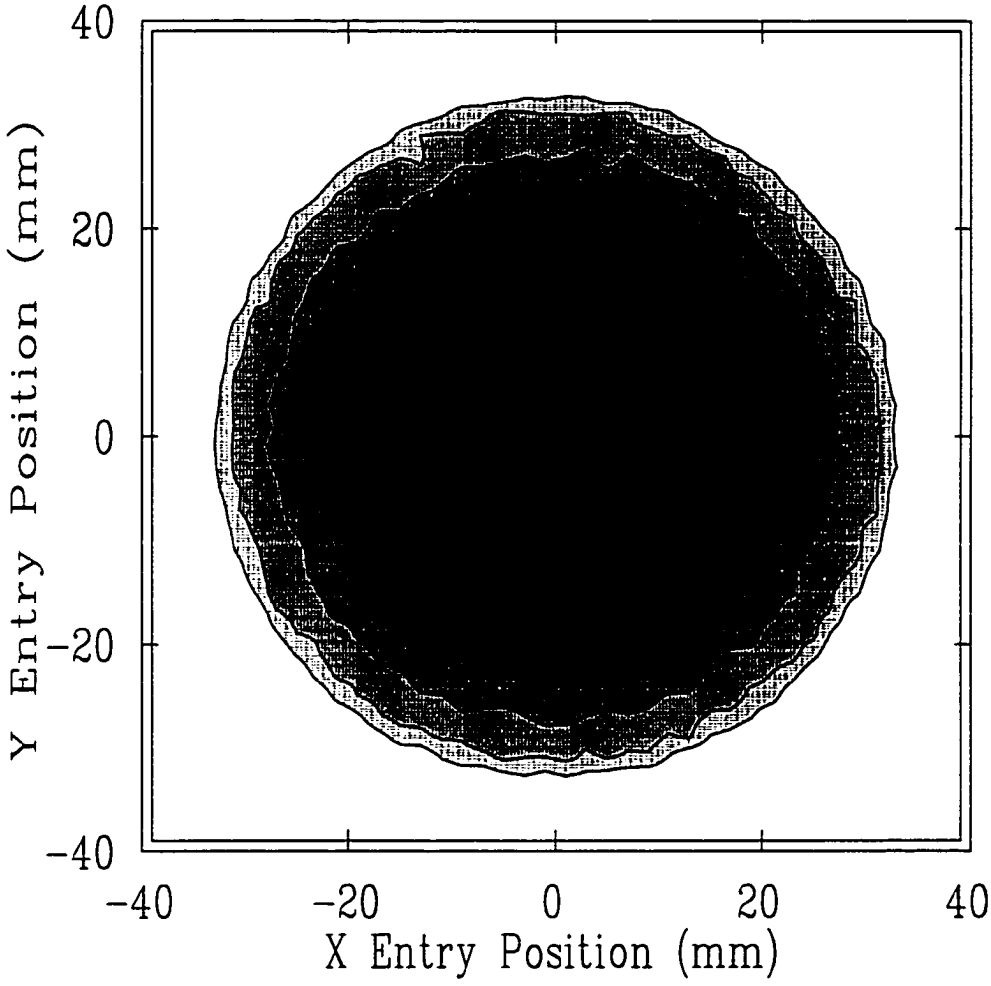

Figure 4.8: *A density plot of the simulated spatial distribution of $t\mu$ atoms arriving on the DS gold foil. The muon beam which entered the US target foil was parametrized by a (10,10) flat-top Gaussian distribution put into the simulation SMC_{thick}. The origin position of entry contains 67% of the total counts in the plot (blackest region around the origin) while the outer most annular disk contains less than 1% of the total counts.*

4.4 Stopping Fraction Normalization

In order to directly compare the experimental data with the Monte Carlo SMC (discussed in an upcoming section) we need to normalize the simulated results to the conditions of the experiment. One normalization number needed is the fraction of beam muons which stop in the hydrogen layer. Only these muons can take part in the muon catalyzed fusion cycle discussed in Chapter 2. The fraction of muons which stops in the hydrogen production target is referred to as the stopping fraction.

The stopping fraction has been intensively studied by M.C. Fujiwara [65]. A similar analysis procedure is followed in this section. To determine the stopping fraction three methods have been employed, two of which use the muon-decay-electron time spectrum. The first method uses the amplitude ratio of different lifetime components in the electron time spectrum while the second method is an absolute measurement of the number of electrons which decay in the hydrogen target. The third, an independent method which uses a complex computer simulation called GEANT, will be discussed at the end of this section.

The muon-decay-electron time spectrum is measured with scintillation counters which surround the target (EN1, EN2, and EGE in chapter 3). The time of the first detected electron among EN1, EN2, or EGE is referred to as the time of the first electron and is histogrammed in Fig. 4.9. A muon which travels in a medium and becomes captured in an atomic orbit will decay to produce an electron with a decay lifetime dependent on the stopping medium. The lifetime of a muon in gold is about 70 ns compared to 2.2 μs in hydrogen. Method 1 to determine the stopping fraction uses this difference in lifetimes and is discussed below along with a brief derivation of the fitting function used in the data analysis.

According to the theory of radioactive decay, the number of muons which decay per

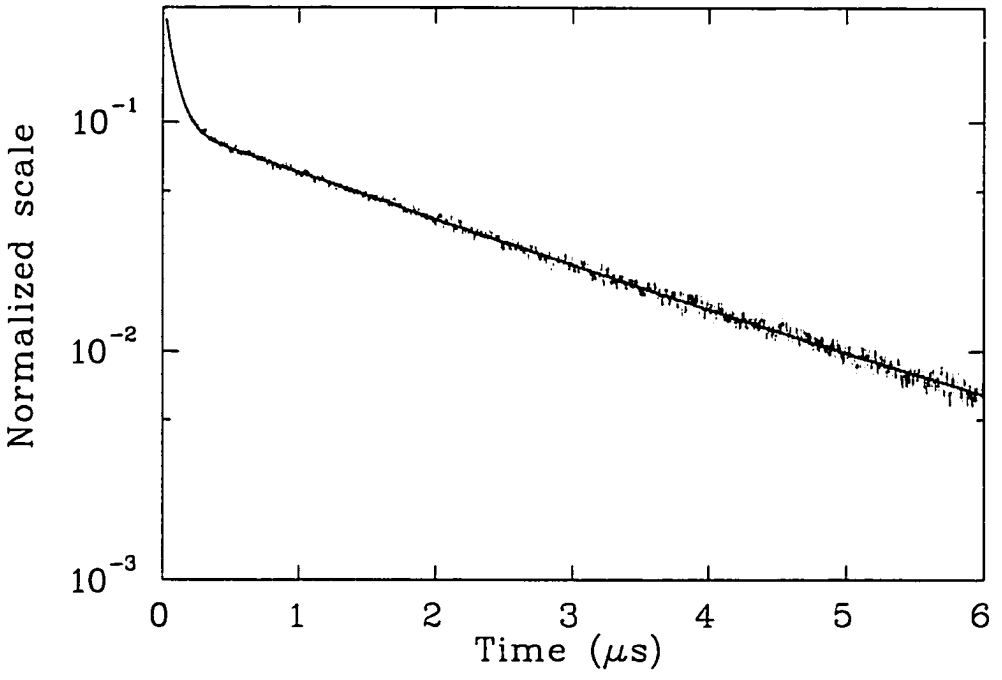

Figure 4.9: *Shown is the time spectrum plotted with error bars of the first electrons detected by scintillation counters surrounding the target (E1, E2, EGE). The solid line is a two exponential function fit with a constant background to the data. The fit is for the time interval [0.02,6] μs.*

unit time can be expressed by the differential equation

$$-dN^{\mu}(t) = \lambda N^{\mu}(t)dt, \tag{4.8}$$

where $N^{\mu}(t)$ is the number of muons at time t and λ is the decay constant [11] or muon disappearance rate. The integral of Eq. (4.8) is

$$N^{\mu}(t) = N^{\mu}(0)e^{-\lambda t}. \tag{4.9}$$

Replacing $N^{\mu}(t)$ in Eq. (4.8) we have

$$-dN^{\mu}(t) = \lambda N^{\mu}(0)e^{-\lambda t}dt. \tag{4.10}$$

However, if the decaying muons are stopping in more than one medium then we must account for the decays in all mediums, in our case, hydrogen and gold. The muon decay rate per unit time would then be the sum of the decay rates per unit time in each medium. Equation 4.10 then becomes

$$-dN^{\mu}(t) = \lambda_{Au} N^{\mu}_{Au}(0) e^{-\lambda_{Au} t} dt + \lambda_{H_2} N^{\mu}_{H_2}(0) e^{-\lambda_{H_2} t} dt. \tag{4.11}$$

The muon decay electrons are detected in the experiment and their detection rate differs from the muon decay rate per unit time of Eq. (4.11). The measured detection rate is given by

$$dN^{e}(t) = -dN^{\mu}[\epsilon_{Au}\beta_{Au} + \epsilon_{H_2}\beta_{H_2}] \tag{4.12}$$

where ϵ is the efficiency for detecting decay electrons in the medium and β is the branching ratio of muon decay rate to total muon disappearance rate. The branching ratio for gold is given by

$$\beta_{Au} = \frac{Q_{Au}\lambda_0}{Q_{Au}\lambda_0 + \lambda^{C}_{Au}} \tag{4.13}$$

where Q_{Au} is the Huff factor for gold, λ_0 is the muon decay rate in free space and λ^{C}_{Au} is the nuclear capture rate. The branching ratio for hydrogen is similar but with values which correspond to hydrogen. The Huff factor accounts for two effects. Because the muon is bound to the nucleus, the muon's decay rate is smaller due to the reduction in the accessible volume of phase space available for the decay. Secondly, a relativistic time dilation decreases the decay rate in the laboratory frame [66]. Noting that the muon disappearance rate, λ, equals $Q\lambda_0 + \lambda^{C}$, the measured electron detection rate per unit time becomes

$$\frac{dN^{e}(t)}{dt} = \epsilon_{Au} Q_{Au} \lambda_0 N_{Au}(0) e^{-\lambda_{Au} t} + \epsilon_{H_2} Q_{H_2} \lambda_0 N_{H_2}(0) e^{-\lambda_{H_2} t}. \tag{4.14}$$

The experimental decay-electron time spectra are histogrammed in finite time bins Δt, implying a discrete function of t_i where $i = 1, 2, 3, ..., n$ and n is the total number of bins

in the histogram. Thus Eq. (4.14) is integrated over Δt to give

$$\int_{t_i-\frac{\Delta t}{2}}^{t_i+\frac{\Delta t}{2}} \frac{dN^e(t)}{dt}dt = \frac{\epsilon_{Au}Q_{Au}\lambda_0 N_{Au}(0)}{\lambda_{Au}}[e^{-\lambda_{Au}(t_i-\frac{\Delta t}{2})} - e^{-\lambda_{Au}(t_i+\frac{\Delta t}{2})}] + \frac{\epsilon_{H_2}Q_{H_2}\lambda_0 N_{H_2}(0)}{\lambda_{H_2}}[e^{-\lambda_{H_2}(t_i-\frac{\Delta t}{2})} - e^{-\lambda_{H_2}(t_i+\frac{\Delta t}{2})}]. \quad (4.15)$$

The above equation, plus an assumed flat background term, is fit to the experimental decay electron time spectra shown in Fig. 4.9. Results of this fit give us a means to calculate the stopping fraction. Results of the fit determine the measured lifetimes of both muon decay in hydrogen and in gold, along with the amplitudes $A_{Au} = \epsilon_{Au}Q_{Au}N_{Au}(0)$ and $A_{H_2} = \epsilon_{H_2}Q_{H_2}N_{H_2}(0)$. Assuming all the muons stop either in hydrogen or gold, the fraction of muons which stop in hydrogen (S_F) is defined as

$$S_F = \frac{N_{H_2}}{N_{H_2}+N_{Au}} = \frac{\frac{A_{H_2}}{\epsilon_{H_2}Q_{H_2}}}{\frac{A_{Au}}{\epsilon_{Au}Q_{Au}}+\frac{A_{H_2}}{\epsilon_{H_2}Q_{H_2}}}. \quad (4.16)$$

Using $Q_{H_2} = 1.00$ and $Q_{Au} = 0.85$ [67] along with the assumption that $\epsilon_{Au} = \epsilon_{H_2}$ [65], the above expression reduces to

$$S_F = \frac{A_{H_2}}{\frac{A_{Au}}{0.85}+A_{H_2}}. \quad (4.17)$$

Shown in Fig. 4.9 is the electron time spectrum and the fit using the two exponential function of Eq. (4.15) with a constant background. Plotted with error bars are the times of first electrons detected by scintillators surrounding the 1000 T*l* H_2 target. The solid line is the fit over a time interval of [0.02,6] μs.

The results of the fits to two different targets are given in Table 4.7. Runs 1830 through 1837 consist of a 1000 T*l* H_2 target while runs 1889 through 1897 consist of a 1000 T*l* D_2 target. Listed are the fit amplitudes ($A_{Au}/0.85$, A_{H_2}, background) normalized to GMU (the number of Good MUons), the lifetimes of muon decay in gold and hydrogen ($1/\lambda_{Au}$, $1/\lambda_{H_2}$), as well as the calculated stopping fraction and goodness of the fit. Two fits have been performed to sums of runs 1830-37 and 1889-97. The values given in round brackets are the errors on the last 2 (or 3) quoted significant figures.

Run	Amplitudes $\times 10^{-2}$/GMU			$1/\lambda_{Au}$	$1/\lambda_{H_2}$	S_F	χ^2/dof
	$A_{Au}/0.85$	A_{H_2}	b[$\times 10^{-2}$]	(ns)	(μs)	(%)	{cl}
1830	15.24(37)	4.785(29)	7.4(31)	73.7(22)	2.126(31)	23.90(52)	1.03{32%}
1831	15.33(100)	4.656(83)	−4.6(100)	80.5(67)	2.239(100)	23.30(135)	1.00 {48%}
1832	15.48(33)	4.797(25)	9.7(26)	72.4(18)	2.105(26)	23.66(44)	1.07{11%}
1833	15.27(42)	4.728(32)	9.2(35)	72.8(24)	2.121(34)	23.64(58)	0.944{83%}
1835	14.67(74)	4.757(68)	8.6(72)	83.5(54)	2.129(71)	24.49(110)	1.02{35%}
1836	15.15(42)	4.763(33)	3.8(38)	75.1(26)	2.156(36)	23.92(58)	1.07{12%}
1837	14.88(44)	4.798(35)	8.5(36)	74.4(27)	2.090(35)	24.38(63)	1.04{26%}
1830-37	15.21(15)	4.774(14)	7.7(15)	74.1(11)	2.121(15)	23.89(25)	1.16{0.50%}
1889-97	15.09(19)	4.777(15)	7.0(15)	73.6(11)	2.084(15)	24.04(27)	0.993{54%}

Table 4.7: *The results of the two-exponential function fits to the electron time spectrum. Runs 1830 through 1837 consist of a 1000 Tl protium target while runs 1889 through 1897 consist of a 1000 Tl deuterium target. Given are the amplitudes, lifetimes, background, stopping fraction and goodness of the fit results for independent runs as well as for runs summed together. The protium target fit result is S_F=23.89(25)% while the deuterium target fit result is S_F=24.04(27)%, in agreement with each other.*

run	δt (ns)	S_F (%)	χ^2/dof	cl (%)
1830-37	−4	24.78(30)	1.16	0.463
(1000 Tl H_2)	−2	24.29(30)	1.16	0.463
	0	23.89(25)	1.16	0.496
	2	23.42(25)	1.15	0.572
	4	22.96(25)	1.15	0.572
1889-97	−4	25.33(32)	0.999	56.2
(1000 Tl D_2)	−2	24.86(33)	0.999	56.2
	0	24.04(27)	0.993	54.1
	2	23.56(27)	0.988	58.0
	4	23.10(27)	0.988	58.0

Table 4.8: *The sensitivity of the stopping fraction to shifts in time zero (δt) for the time of the first detected electron for both 1000Tl H_2 and 1000Tl D_2 targets.*

The majority of fits in Table 4.7 are of good quality. The gold lifetime of 74.3 ± 1.5 ns measured by Suzuki, Measday, and Roalsvig [67] is consistent with the fitted values. However, their measured value for hydrogen of 2.195 μs is slightly larger than our fitted values. Variations of the fit and background used were studied in detail [65] but do not explain this difference. Fixing the muon lifetime in hydrogen to the measured value of 2.195 μs was also tried with both a constant and an exponential background, each resulting in an unsatisfactory fit [65]. This suggests that the difference in the lifetime is not due to incorrect modelling of the background. It has been observed recently by our collaboration [68] that muonic protium $p\mu$ is emitted from the solid layer. Thus, muonic protium emitted back into the gold foil would allow the muon to transfer from protium to gold. This muon loss mechanism could in part be responsible for the lifetime discrepancy. A small amount of nonhydrogenic contamination in the target would also serve as a muon loss mechanism.

The sensitivity of the stopping fraction to the choice of zero time in the decay electron time spectra has also been investigated. Time zero (δt) was shifted from its original value by up to ± 4 ns and the results are given in Table 4.8. The variation in A_{H_2} was found to be completely negligible on this time scale and the change in stopping fraction is solely due to the difference in A_{Au}.

Method 2, which does not rely on the amplitude of the gold component A_{Au} in the decay electron time spectra can also be used to determine the stopping fraction. A similar fit as the one performed in Method 1 is applied to the decay electron spectra, however, only the amplitude for the hydrogen component A_{H_2} is used. By determining the absolute electron detection efficiency $\epsilon_e\Omega_e$ and using A_{H_2}, the stopping fraction can be determined via the following:

$$S_F = \frac{A_{H_2}}{\epsilon_e\Omega_e}. \tag{4.18}$$

The absolute efficiencies for electron detection are calculated by using the delayed

electron coincidence (del-e) cut discussed in detail in section 4.5.2—Neutron Fusion Data. The del-e cut is a time cut of 200 ns to 5.05 μs and is used to ensure that the recorded event in the detector of interest (either silicon or neutron) is due to a muon catalyzed fusion process. The del-e cut suppresses background due to neutrons released in capture processes in which the muon is converted into a neutrino and does not decay into an electron. By imposing the del-e cut, it is demanded that the electron which is observed in the scintillator is recorded only if it occurs within a given time window after a hit is recorded in the detector of interest (either silicon or neutron), thus ensuring with a high probability that fusion was detected and subsequently the muon decay electron was detected. The del-e cut is essential to suppress background in the neutron detectors but this is not necessary in the silicon detectors due to the good energy resolution of the detector and excellent detection efficiency for alpha particles from $dt\mu$ fusion. The detection efficiency for the 3.5 MeV alpha particles we measure from $dt\mu$ fusion in the silicon detectors is assumed to be 100%. By utilizing this feature of the detectors, we are able to measure the efficiency of the del-e cut and hence determine the absolute efficiency of the electron scintillators (fusion particle detection in both the neutron and silicon detectors will be discussed in the upcoming sections).

The del-e cut efficiency ϵ_{del} is given by the product of electron scintillator detection efficiency and solid angle $\epsilon_e\Omega_e$, the branching ratio for electron emission β_e, and the del-e time cut efficiency ϵ_{time}

$$\epsilon_{del} = \epsilon_e\Omega_e\beta_e\epsilon_{time} = \epsilon_e\Omega_e\beta_e \int_{0.2}^{5.05} \lambda_{del}\ exp(-\lambda_{del}t)\ dt, \tag{4.19}$$

where the total electron disappearance rate λ_{del} is the sum of the free muon decay rate λ_0 and the muon loss rate λ_X [65]. The branching ratio for electron emission is given by

$$\beta_e = \frac{\lambda_0}{\lambda_0 + \lambda_X}. \tag{4.20}$$

The del-e cut efficiency ϵ_{del} is given by the ratio of the experimental yield for alpha fusion with the del-e condition Y^{α}_{del} to the experimental yield for singles alpha fusion (with no del-e condition) Y^{α}_{sing}. The electron disappearance rate λ_{del} can be obtained from the time spectrum of the electrons which are recorded after the fusion alpha signal is detected in the silicon detectors. The electron detection efficiency can be determined by using the following relations

$$\epsilon_e \Omega_e = \frac{\epsilon_{del}}{\beta_e \epsilon_{time}} = \frac{Y^{\alpha}_{del}}{Y^{\alpha}_{sing}} \frac{\lambda_{del}}{\lambda_0} [exp(-\lambda_{del} t_1) - exp(-\lambda_{del} t_2)]^{-1} \tag{4.21}$$

where $t_1 = 0.2$ μs and $t_2 = 5.05$ μs. Thus, the muon stopping fraction in hydrogen given in Eq. (4.18) can be expressed as

$$S_F = A_{H_2} \frac{\beta_e \epsilon_{time}}{\epsilon_{del}}. \tag{4.22}$$

The delayed electron disappearance rate λ_{del} was determined by fitting, with a single exponential function and a flat background, spectra of the time between an alpha fusion event in Si1 or Si2 and the first following electron telescope event. A time cut of 0.02 to 0.4 μs was placed on the silicon fusion spectra to select prompt fusion events which occurred in the upstream D_2 moderator layer, where the ratio of signal to background events was maximized. Two separate energy cuts were applied: the cut of channel 2000 to 3800 was used to contain the entire fusion peak and the other cut of channel 2000 to 3000 was chosen to avoid fusion events which occurred near the surface of the D_2 layer, thus losing little energy in the layer. The smaller energy cut was chosen to test for possible systematic effects which depend on where the fusion event took place in the layer.

Given in Table 4.9 are the results of a fit of a single exponential with a flat background to the del-e time spectra. Runs 1946-56 were used in which a 1000 Tl SET $\oplus$ 10 Tl D_2 target (due to the frequent use of such a target, the notation Standard Emission Moderator Target (SEMT) will be used) had been deposited. For the wide energy cut of channel 2000-3800

Energy cut	1st E after Si1			1st E after Si2		
	$1/\lambda_{del}$ (μs)	χ^2/dof	cl(%)	$1/\lambda_{del}$ (μs)	χ^2/dof	cl(%)
2000-3800	1.972(45)	0.987	61	2.016(43)	1.00	47
2000-3000	2.156(110)	1.06	9.4	2.242(110)	1.02	31

Table 4.9: *The results of the fits for a single exponential with a flat background to the del-e time spectra for Si1 and Si2. The energy cut of channel 2000-3800 covers the entire fusion peak while the smaller cut of channel 2000-3000 does not contain fusion events which occurred at the surface of the D_2 moderator layer.*

ϵ_{del}			β_e	ϵ_{time}	$\epsilon_e\Omega_e$	S_F
Si1	Si2	Average	(%)	(%)	(%)	(%)
11.6(2)	11.9(2)	11.8(3)	95.3(46)	81.9(6)	15.05(73)	31.7(17)

Table 4.10: *The del-e cut efficiency ϵ_{del}, branching ratio β_e, time cut efficiency ϵ_{time}, electron scintillator detection efficiency $\epsilon_e\Omega_e$ and muon stopping fraction S_F.*

the values of $1/\lambda_{del}$ for Si1 and Si2 are consistent with each other with the average being 1.994 ± 0.062 μs. For the smaller energy cut the $1/\lambda_{del}$ values for Si1 and Si2 are consistent with each other with the average being 2.199 ± 0.156 μs. Taking the average of these two values gives $1/\lambda_{del} = 2.096 \pm 0.102$ μs with the error covering the two extremes. It should be noted that using the smaller energy cut gives a value for λ_{del} that is 2 σ lower than the energy cut of 2000-3800, implying that the determination of λ_{del} is limited by systematic effects, one of which is perhaps due to the finite thickness of the moderator layer [65].

Given in Table 4.10 are the del-e cut efficiencies for Si1 and Si2 with the average value $\epsilon_{del} = 0.118(3)$. For the electron detection efficiency, the ratio of fusion yields with and without the del-e condition was used for a SEMT target. For both the singles and del-e fusion spectra, a background of 1000 Tl SET was subtracted to remove any non-fusion processes. The branching ratio for electron emission was determined to be β_e=0.953(46), the time cut efficiency ϵ_{time}=0.819(6) and electron scintillator detection ef-

ficiency $\epsilon_e\Omega_e$=0.1505(73). Using the average value of the hydrogen amplitude determined by Method 1, A_{H_2}=4.776(14)$\times 10^{-2}$, the muon stopping fraction in hydrogen calculated via Method 2 is S_F = 0.317(17).

Another method to determine the stopping fraction, independent from methods 1 and 2 has been performed by G.M. Marshall [69]. The program GEANT [70] was used to simulate the experimental muon beam momentum and beam width. This simulation package does not take into account any muonic atom or muonic processes, however the experimental apparatus had been modeled in great detail. GEANT can perform detailed energy loss simulations for complicated geometries and is an ideal method to determine the stopping fraction. By including information about the muon beam size and divergence in the code and adjusting the beam momentum and spread, a reasonable agreement with the experimental momentum scan (the distribution showing the amount of beam stopping in the target for changes in the momentum of the muon beam) and therefore an estimate of the stopping fraction can be obtained. Shown in Fig. 4.10 is the GEANT simulation of the muon beam momentum scan compared to the experimental momentum scan [69]. By this method. the maximum fraction of muons stopping in the hydrogen target occurs at the beam momentum of 26.8 MeV/c and has a Gaussian momentum spread of approximately 5.5% (FWHM). The estimate of stopping fraction is 0.32 with known systematic uncertainties of 0.02 [69]. It should be noted that the momentum spread which best describes the experimental momentum scan is 5.5% (FWHM) and not $\approx$ 4% (FWHM) which was quoted in Chapter 3. A possible reason for the discrepancy could be that the 4% value was calculated for a surface beam of μ^+ at 29 MeV/c rather than μ^-. The surface muons come from π^+ decay at rest in the surface layer of the production target and are not exactly the same as the negative muons we use in our experiment [71]. However this difference is not fully understood.

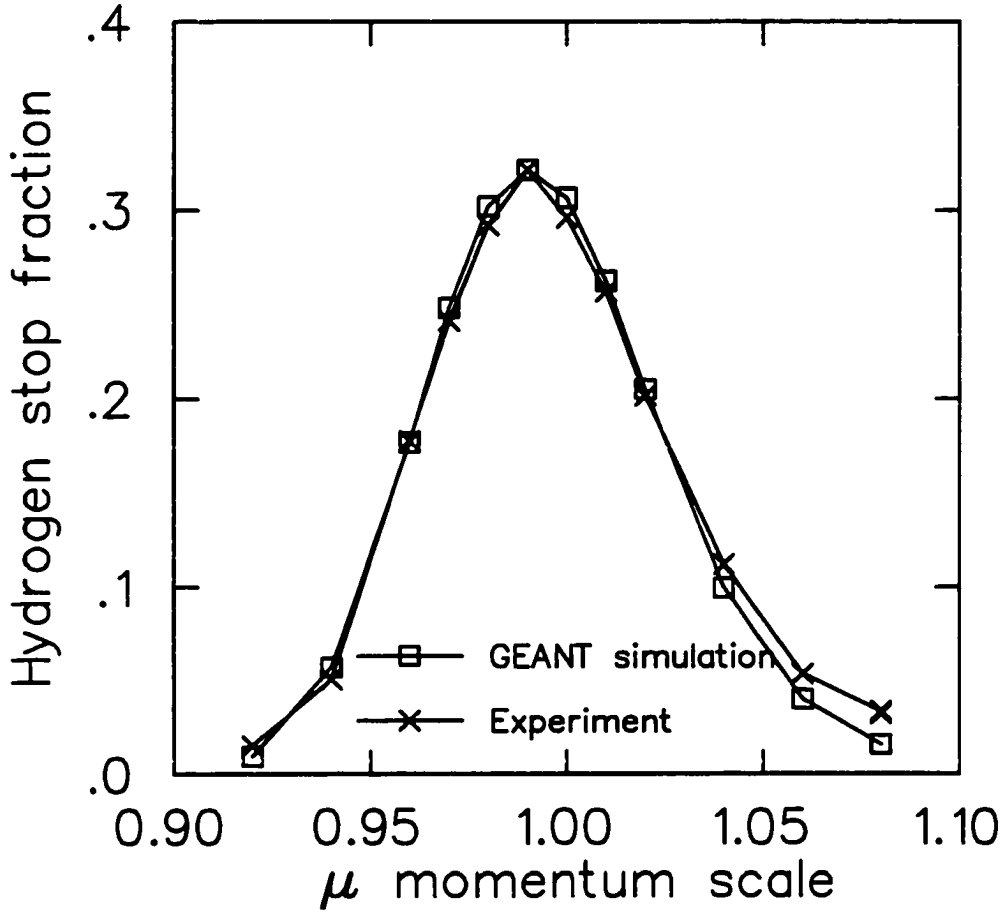

Figure 4.10: *The muon stop fraction as a function of momentum for a 1000 Tl protium target. The data is normalized to the simulation for comparison and the maximum point corresponds to a beam momentum of 26.8 MeV/c. Figure taken from [69].*

The results of the three different methods of determining the muon stopping fraction are given below:

$$Method\ 1 \qquad S_F = 23.89 \pm 0.25\ \% \tag{4.23}$$

$$Method\ 2 \qquad S_F = 31.7 \pm 1.7\ \% \tag{4.24}$$

$$Method\ 3 \qquad S_F = 32.0 \pm 2.0\ \%. \tag{4.25}$$

Methods 2 and 3 agree while the value obtained through Method 1 is much lower. It appears that using the amplitude of the gold component obtained through the two exponential fit to the electron time spectrum may not be reliable. It is not clear why this procedure consistently produces lower stopping fractions. Perhaps the muonic protium which is emitted back into the gold foil along with other muon loss mechanisms are in part responsible for an incorrect determination of A_{Au}. When methods which do not rely upon the value of A_{Au} are used to determine S_F, the values are consistent with each other. Thus, in the analysis to follow the value of Method 3, $S_F = 32.0 \pm 2.0$ %, which is consistent with the value obtained by Method 2, will be used.

4.5 Time-of-Flight Analysis

The solid targets provide spatially separated layers of different isotopic composition allowing interactions of the muonic system with different isotopes to be separated, providing an opportunity to measure the rate and energy dependence of resonant molecular formation using time of flight.

Muonic atoms which are emitted from the solid targets placed on the US gold foil will have a flight time to the DS gold foil which is related to their energy. A 1 eV $t\mu$ atom has a speed of approximately 0.8×10^6 cm $\cdot$ s^{-1}. The distance between the target foils is 17.9 mm. This corresponds to a flight time of the $t\mu$ atom of about 2 μs. For a $t\mu$ of several eV

(where transfer of a muon from a proton to a triton produces a $t\mu$ atom with 45 eV), the emission time from the US target layer is short (for a tritium concentration of 0.1%, the time is on the order of 0.1 μs) compared with the flight time to the reaction foil. Resonant $dt\mu$ molecular formation rates are on the order of 10^9 s^{-1}, with a fusion rate on the order of 10^{12} s^{-1}. Thus, for molecular formation occurring in the DS layer, the time interval from the detection of the muon arrival in the system to the detection of a fusion signal is dominated by the time of flight.

Using the flight time between muon detection in the US production layer and fusion signal produced in the DS layer, the energy distribution for muon molecular formation can be determined. Some difficulties do arise. Because it is not possible to invert the time-of-flight yield in a unique way, a Monte Carlo simulation is required to interpret the data [72]. The code, also necessary to calculate other important effects, will be discussed in a subsequent section. An added complication is the possibility of the $t\mu$ atoms scattering in the DS layer and losing energy before molecular formation occurs. These processes are referred to as indirect processes and present a complication when interpreting the time-of-flight data because the time of flight is not an indication of the energy at which molecular formation occurs.

In the following sections the time-of-flight data taken with both silicon detectors and neutron detectors will be discussed. Monte Carlo simulations of the data (using Super Monte Carlo described in section 4.6) will later be compared to the results presented in the silicon fusion data section.

4.5.1 Silicon Fusion Data

Energy Spectra Features

To isolate the 3.5 MeV alpha particles resulting from fusion in the US moderation layer, a time cut of 0 to 1.5 μs is used. By applying this time restriction, the broad asymmetric energy distribution shown in Fig. 4.11 is obtained. The solid circles correspond to a SEMT. The hollow circles correspond to background which consists of a 1000 T*l* SET target in which no fusions occur. The data is plotted in counts/GMU and data from both Si1 and Si2 have been added together despite the fact that the absolute count rates in Si1 and Si2 were dissimilar, with Si2 detecting more particles. Reasons for this will be discussed in detail at the end of this section. The observed alpha energy distribution is broad due to the thickness of the D_2 moderation layer since the alphas lose energy exiting the layer at the angles required for acceptance into the silicon detectors.

To isolate fusion reactions which occur in the DS layer, a time cut of 1.5 to 6 μs is used. This corresponds to relevant $t\mu$ atom flight times to the DS target and largely avoids fusion in the US moderation layer. Shown in Fig. 4.12 is the energy deposited in Si1 and Si2 per GMU. The target consists of SEMT upstream with 3 T*l* HD downstream. A background from the SEMT has been subtracted to eliminate fusion occurring US. Note that the errors shown on the data are statistical and include those from background subtraction. The systematic uncertainties will be discussed later. The energy distributions are nearly symmetrical and much narrower than the distribution plotted in Fig. 4.11 due to the thin DS HD reaction layer which results in a small energy loss of the alphas which reach the silicon detectors.

In past experiments the yield per GMU in each silicon detector has been identical within statistical uncertainty, due to the symmetry of the detector locations with respect to the target foils. In the July 1996 experiment, the yields of the detectors were not identical.

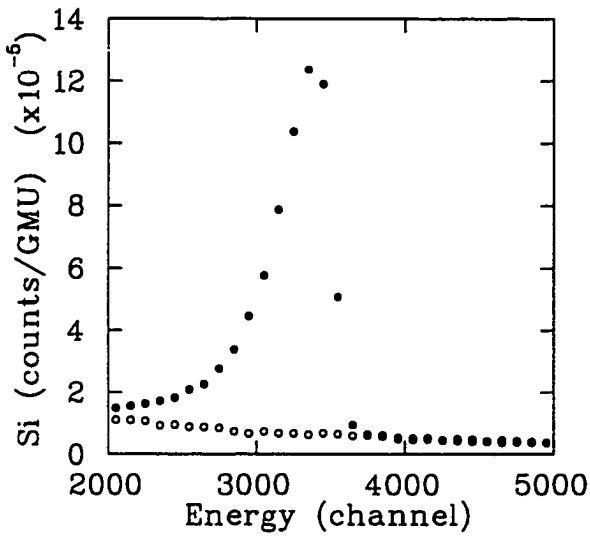

Figure 4.11: *Energy spectrum summed from both silicon detectors and normalized to GMU for a time range of 0 to 1.5 μs. The filled circles correspond to a SEMT in which fusion occurs in the overlayer. The background has also been plotted (hollow circles) and corresponds to a SET in which no fusion occurs. The background differs significantly from the fusion data only under the peak. Recall that the energy calibration is near 1 keV/ch (Eq. (4.1) and Eq. (4.2)).*

By applying an energy cut of channel 3200 to 3600 to the spectra shown in Fig. 4.12, the total intensity of each peak can be calculated. The values obtained are:

$$Si1 = (2.93 \pm 0.11) \times 10^{-6}, \tag{4.26}$$

$$Si2 = (3.28 \pm 0.12) \times 10^{-6},$$

with Si2 consistently exhibiting a higher yield than Si1. There are two possible reasons for this asymmetry. A metal foil installed before the 1996 data run to shield the detectors from beam muons could have shifted when the apparatus was moved into the experimental area. If the shield for Si1 was not correctly in place, it could stop some of the incoming fusion alpha

particles. However, we have no direct evidence that this occurred. The other possible cause is a failure in the mechanism which controlled the movement of the horizontal momentum slits in the M20 beam line at TRIUMF, resulting in the slits remaining open. The beam was optimised on the T1 beam counter after the slit failure occurred. The beam optimization was done several times throughout the course of the experiment, with consistent results. In July 1994 the horizontal momentum slits were set at 50 mm whereas during the July 1996 run they were inoperable and remained open at 302 mm. It is not clear what effect this would have on the symmetry with which the beam hits the center of T1. Perhaps the beam is optimized such that the spot is asymmetric along the target axis, although it is not clear why this would occur. The beam was optimized using the same procedure as in 1994, with the only known difference being the position of the horizontal momentum slits. Throughout the run the counts in Si2 are consistently higher than in Si1 by about 10-20%.

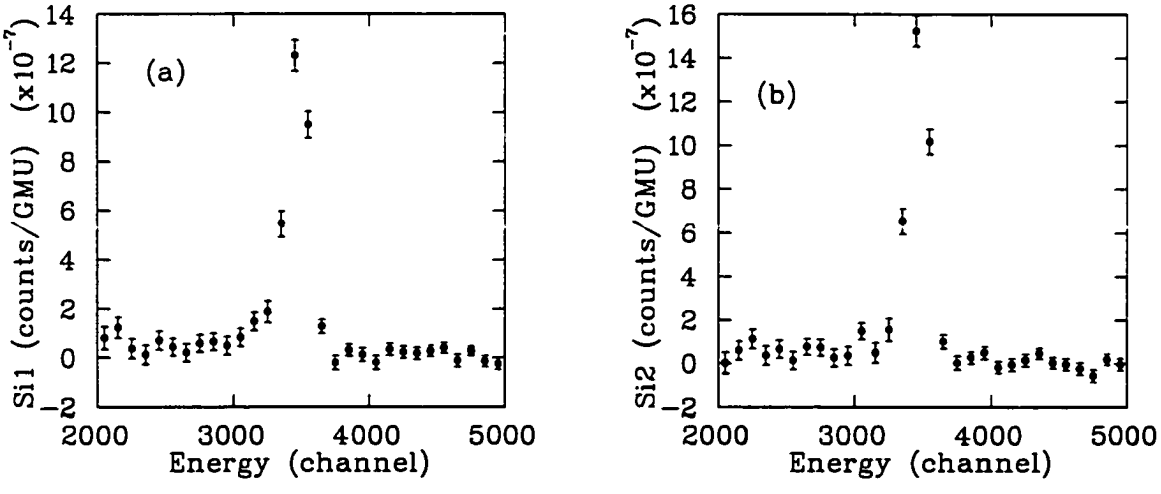

Figure 4.12: *Energy deposited in Si1 (a) and Si2 (b) normalized per GMU for a time range of 1.5 to 6 μs, corresponding to fusion occurring DS. The data plotted is for a target of 1000 Tl SET ⊕ 10 Tl D_2 US with 3 Tl HD DS. Background has been subtracted.*

Time Spectra Features

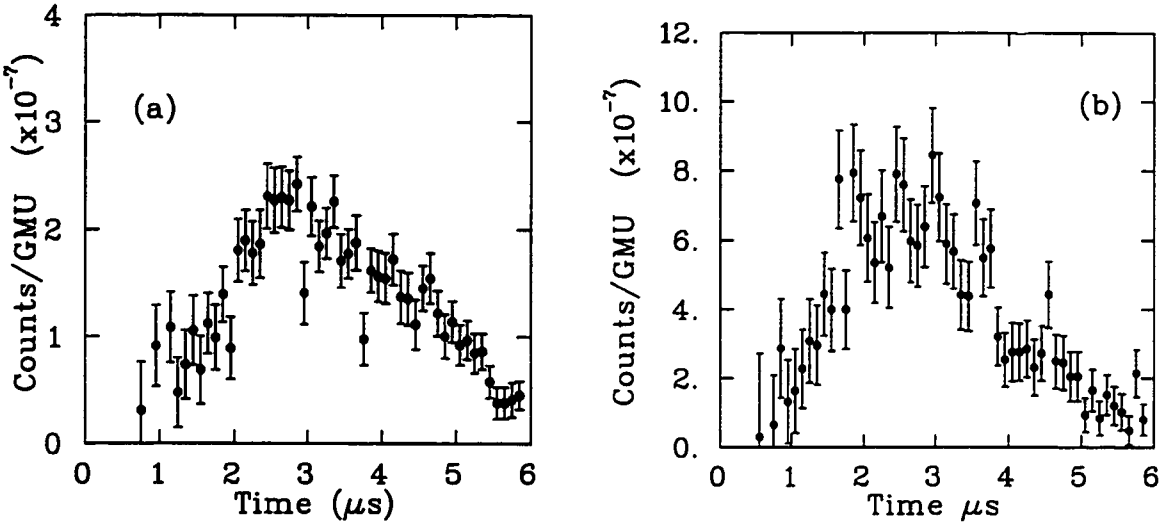

Figure 4.13: *The background subtracted fusion time spectra for a SEMT US and 3 Tl HD DS target (a) and a SEMT US and 7 Tl HD DS target (b), for the energy cuts* $3200 < E < 3600$ *(a) and* $2600 < E < 3800$ *(b). The data from Si1 and Si2 have been summed.*

Figure 4.13 depicts the time-of-flight spectra corresponding to fusion occurring in the downstream HD target reaction layer. The energy cuts placed on the fusion spectra were $3200 < E < 3600$ for the 3 T*l* HD DS and $2600 < E < 3800$ for the 7 T*l* HD DS. Both spectra were taken with the same US target, SEMT, with different thicknesses of the HD reaction layer DS. Both spectra have had background subtracted and the error bars reflecting this subtraction are statistical only. The visible structure corresponds to the predicted resonance of $t\mu + HD$ at 3 K as shown in Chapter 2. The flight time of the $t\mu$ atoms to the DS reaction layer enables us to infer the energy of molecular formation. The predicted resonance in the energy region from 0.3 eV to 0.5 eV appears at times greater than 3 μs in the fusion time spectra. The resonances at higher energies occur at earlier times. In Fig. 4.13 the 3 T*l* HD layer was chosen because it remains thick enough to be a

substantial fraction of the characteristic interaction length for molecular formation to occur (this was determined by SMC—discussed in section 4.4). In the 7 Tl HD reaction layer it is expected that the indirect processes of $t\mu$ scattering and energy loss will dominate. The resonance structure is thus expected to play a lesser role than in the 3 Tl data. By comparing the figures it is clear that the thicker reaction layer produces more fusions. A Monte Carlo comparison to data will be given in an upcoming section, along with a discussion of the dominant physics processes that are occurring.

Uncertainties

The energy spectra of the 3.5 MeV alpha particles produced in dt fusion are shown in this section. The time cut used to select fusion events originating in the downstream target is 1.5 to 6 μs for all spectra displayed. Background, determined from a SEMT spectrum, has been subtracted from all data. The statistical error bars reflect this background subtraction. Due to the very thick HD (300 Tl) deposited in runs 1975-59, these targets are described as having 300 Tl HD downstream, instead of the actual 7 $HD \oplus$ 20 $D_2 \oplus$ 300 Tl HD. Virtually all the downstream fusion occurs in the 300 Tl HD in these runs. The effect of widening the energy cut is investigated in this section. Systematic and statistical errors will be combined in Chapter 5 along with the time-of-flight spectra and final results.

The summed energy spectrum from both silicon detectors for 3 Tl HD is shown in Fig. 4.14 (a). The energy cut selected for the time-of-flight analysis was $3200 < E < 3600$. The normalized count under the peak for this energy cut is $(6.26 \pm 0.16) \times 10^{-6}$. By widening the energy cut by two bins on each side, $3000 < E < 3800$, the count increases to $(6.91 \pm 0.10) \times 10^{-6}$ (approximately 10% higher). Shown in Fig. 4.14 (b) is the equivalent spectrum for 7 Tl HD for which the energy cut is $2600 < E < 3800$, since the alpha peak is broader, due to the thicker HD layer. The count under the peak in this energy range is (1.86 $\pm$

$0.07)\times10^{-5}$ and by widening the cut to $2400 < E < 4000$, the count increases 8% to $(2.01 \pm 0.08)\times10^{-5}$.

Similar spectra for the 300 T*l* *HD* target are given in Fig. 4.15: (a) for a SEMT upstream and (b) for a SET $\oplus$ 14 T*l* D_2 upstream. The energy cut selected in (a) is $1800 < E < 3900$ and (b) is $2000 < E < 3800$.

Both spectra for the 300 T*l* *HD* target are very broad and distinctly different from the alpha spectra from thin targets. At high energy the background subtraction is satisfactory for all targets. However at lower energies the alpha spectrum for the 300 T*l* targets does not drop to zero, as is the case for the thin targets because the energy loss of the alpha particles is sometimes substantial. The source of the background at low energies around 1000 keV is in part due to muon decay electrons. It appears with varying intensity in all spectra, including that of a simple protium target deposited on the upstream gold foil.

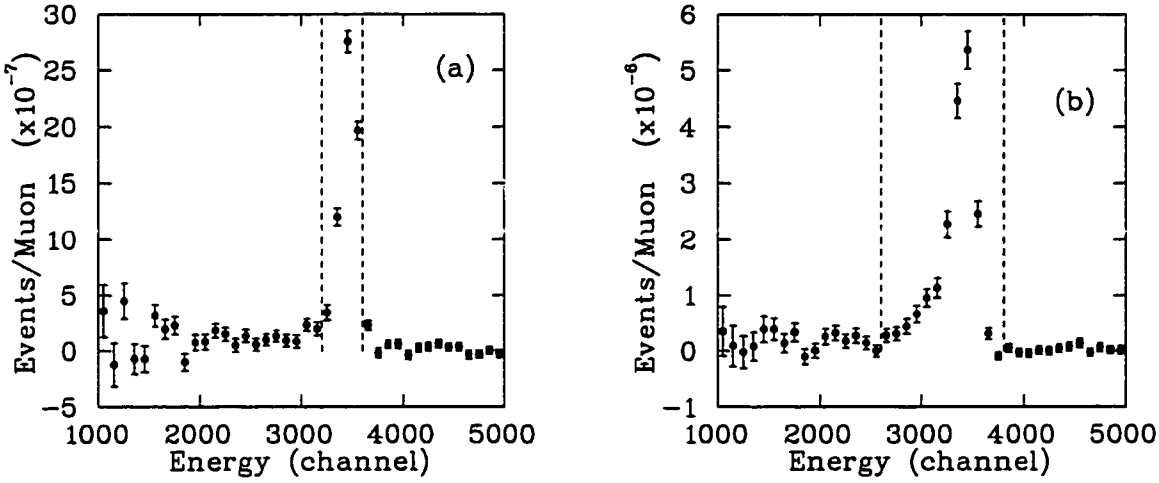

Figure 4.14: *Energy deposited in the silicon detectors (Si1+Si2) normalized per muon for (a) 3 Tl and (b) 7 Tl HD target downstream. The dashed lines show the energy cuts selected for the time-of-flight analysis.*

Another feature which appears in the thick target data is a possible small peak around channel 3000 possibly due to a 3 MeV proton emitted following dd fusion in the reaction:

$$dd\mu \rightarrow p + t + \mu \ . \tag{4.27}$$

Estimation of the strength of this peak is not straightforward as it requires a Monte Carlo calculation of the muon stopping rate in the downstream HD target, capture rate onto a d atom, formation of $d\mu$ muonic atoms, and then formation of a $dd\mu$ molecular ion. This will be described in detail in section 4.8.

For runs 1973-74, a 20 Tl layer of D_2 was deposited on top of the existing 7 Tl HD. The energy deposited in the silicon detectors is shown in Fig. 4.16. Again, the broadness of the peak is due to the thickness of the layer. The energy cut of $1800 < E < 3800$ contains $5.13(9)\times10^{-5}$ counts. By widening the cut to $1600 < E < 4000$, the count increases 5% to $5.39(11)\times10^{-5}$.

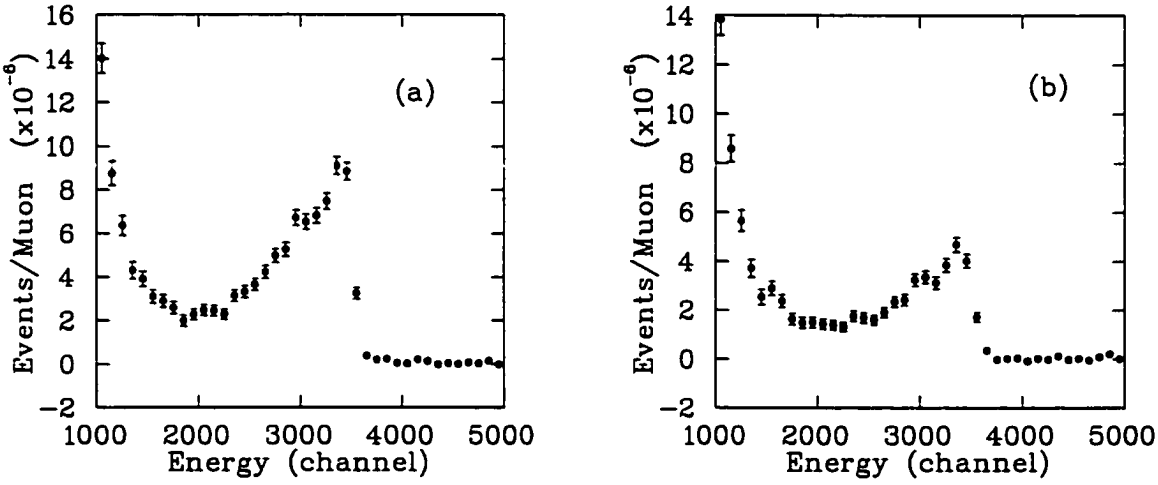

Figure 4.15: *Energy deposited in the silicon detectors (Si1+Si2) normalized per muon. (a) is for a SEMT upstream and 300 Tl HD targets downstream and (b) is for a SET* $\oplus$ *14 Tl* D_2 *upstream and 300 Tl HD target downstream.*

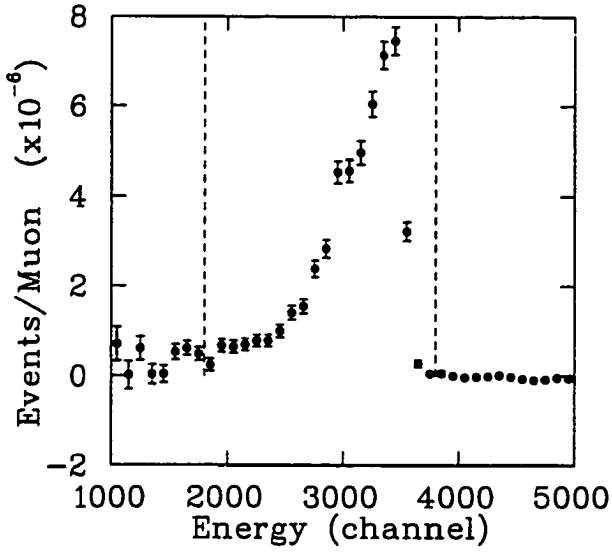

Figure 4.16: *Energy deposited in the silicon detectors (Si1+Si2) normalized per muon for a target of 7 HD ⊕ 20 Tl D_2. The dashed lines show the energy cuts selected for the time-of-flight analysis.*

4.5.2 Neutron Fusion Data

The Pulse-Shape Discriminator (PSD) value is a comparison of integrals of the incoming energy pulses due to either slowing recoil electrons (electrons from an interaction with a photon) or slowing recoil protons (protons from an interaction with a neutron) in the NE213 neutron detector material. To distinguish between photon and neutron events, an energy threshold is required before the PSD value becomes reliable. Low energy photon events occurring in the detector can be misidentified as neutrons (see Fig. 4.17). There exists a high background of low energy gammas which can be due to beam electrons, muon decay electrons or muon induced nuclear gammas; the tail of this photon peak can overlap the tail of the peak due to low energy recoil protons (neutrons hitting protons and scattering forward).

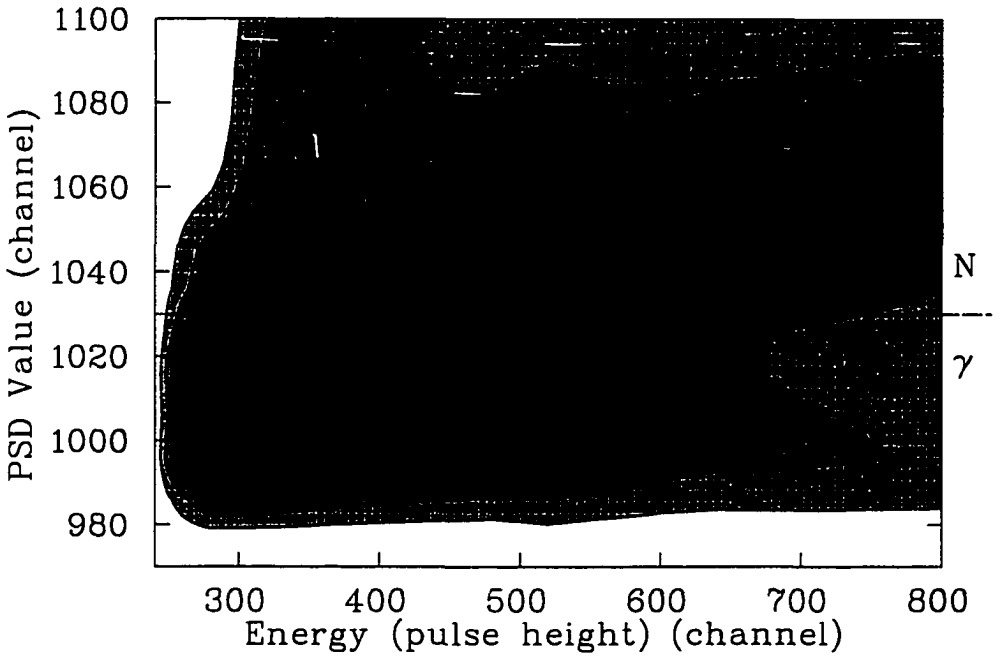

Figure 4.17: *A PSD versus pulse height density plot for N1. The two-lobed structure is clearly visible; the low horizontal band with PSD values around 1000 represent photon events. The horizontal line at PSD=1030 shows the cut value, events above this line are considered as neutron events. To allow all regions to be displayed, the fourth root of the number of counts was taken before plotting.*

To minimize misidentified events due to this breakthrough, an energy threshold must be exceeded for the PSD value to be recorded. This procedure provides accurate neutron detection with a reduction in background due to photons misidentified as neutrons [56].

Shown in Fig. 4.17 is a density plot of the PSD values and pulse heights of the signals coming from neutron detector N1. To allow all regions to be displayed, the fourth root of the number of counts was taken before plotting. The value of the PSD cut for N1 was chosen to be 1030 as shown by a solid horizontal line. Events above this value were considered to be neutron events while events below were attributed to photons. The distinct two lobed

structure is clearly visible in Fig. 4.17 and the cut imposed selects events due mainly to neutrons. The density plot for neutron detector N2 is similar but the PSD cut was 785.

The neutron events selected come not only from fusion reactions, but also muon nuclear capture on gold and from ambient neutron background. Since the experimental target foil is gold, muons that stop in the foil and capture produce neutrons within the capture lifetime of approximately 70 ns. The intensity of this capture background is so large that the fusion signal is difficult to see, thus a method is needed to suppress it [58]. The method employed to suppress events due to neutrons released in muon nuclear capture reactions is to impose the restriction that the event which created the neutron did not consume the muon. This can be achieved by requiring the detected neutron to be followed by the detection of a muon decay electron. The electron detection time is plotted in Fig. 4.18 (note that time zero is when the neutron is detected). The spectrum is shown (a) unexpanded and (b) expanded, to display the region of interest. If the time is negative it means the electron was detected before the neutron and this cannot be a valid fusion event. These events can be due to muons undergoing nuclear absorption on gold and the gold nucleus emitting a neutron which is detected just after the detection of an electron from an Auger process or other source.

The dashed line at 200 ns shows the cut chosen to define fusion events. A second time restriction imposed allows the event to be recorded only if the decay occurs within 5.05 μs after the neutron event. This restriction is greater than 2 muon lifetimes thus the majority of muons will decay in this time range. This time cut of 200 ns to 5.05 μs is referred to as the del-e (delayed electron) cut .

The del-e cut strongly suppresses background which is predominantly due to neutrons from nuclear capture followed by an accidental event in the delayed electron coincidence [58]. Figure 4.19 is a plot of the energy spectrum in N1 for events passing the PSD cut only (re-

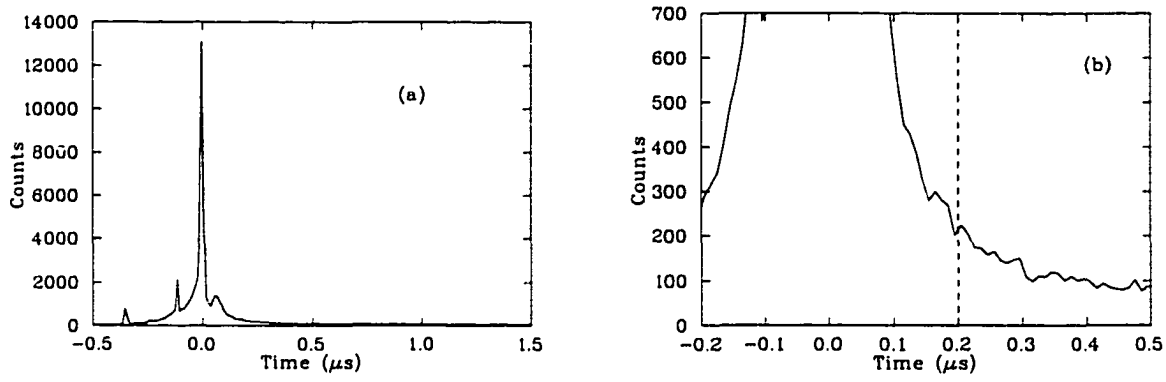

Figure 4.18: *Shown is the time spectra for electron detection after a neutron has been detected. The graph (a) has been expanded in (b) to show the time range of interest. Negative times correspond to an electron detected before a neutron and are not candidate fusion events. The dashed line gives the lower time cut chosen for fusion events.*

ferred to as "singles") and for del-e events which both pass the PSD cut and have an electron detected between 0.2 μs and 5.05 μs after the event. The spectrum due to single neutrons has a shape which is dominated by capture neutrons while the del-e spectrum results from monoenergetic neutrons along with a small background. Although the fusion signal is contained in both spectra, fusion counts in the singles spectra are greatly outnumbered by capture events. In the del-e spectra, the counts due to 14 MeV neutrons vanish at about channel 1540. The dashed lines in Fig. 4.19 show the chosen pulse height cut, and events between the dashed lines have little background neutron contamination in the fusion neutron data. The spectrum for N2 is similar to N1, with the maximum pulse height at about channel 870.

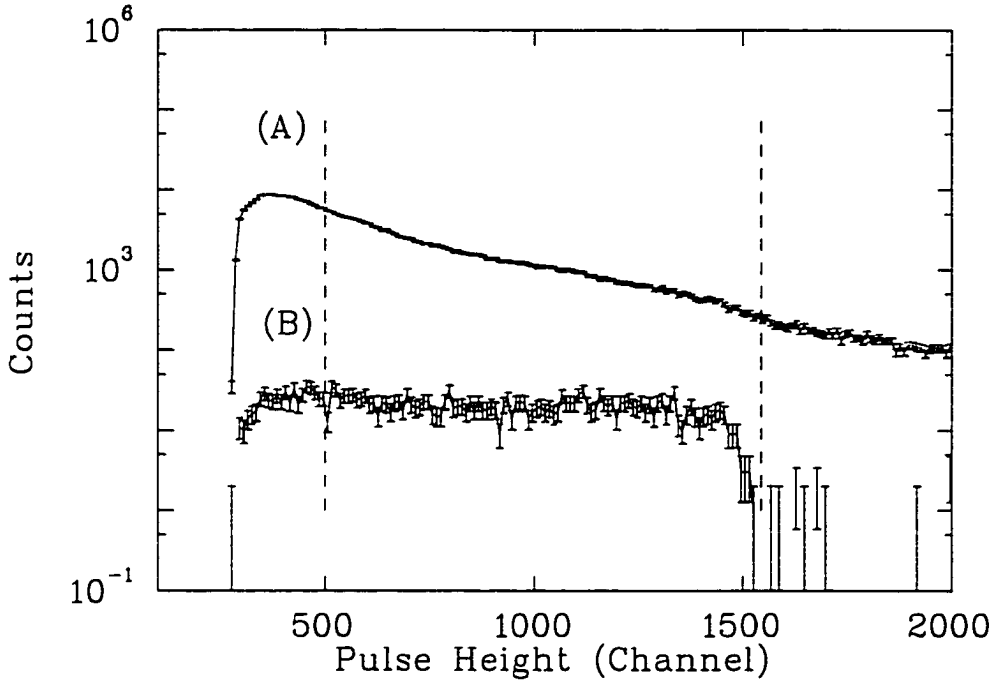

Figure 4.19: *A plot of counts versus energy pulse height for singles and del-e neutrons in N1 for a SEMT. Curve (A) is the spectrum of single neutrons and curve (B) is the spectrum of neutrons passing the del-e condition. The shape of curve (B) is characteristic of monoenergetic neutrons. Note that for N1, 14 MeV neutrons do not generate counts past channel $\sim$ 1540 in the del-e spectra. The dashed lines give the pulse height cuts chosen for the analysis.*

Energy Spectra Features

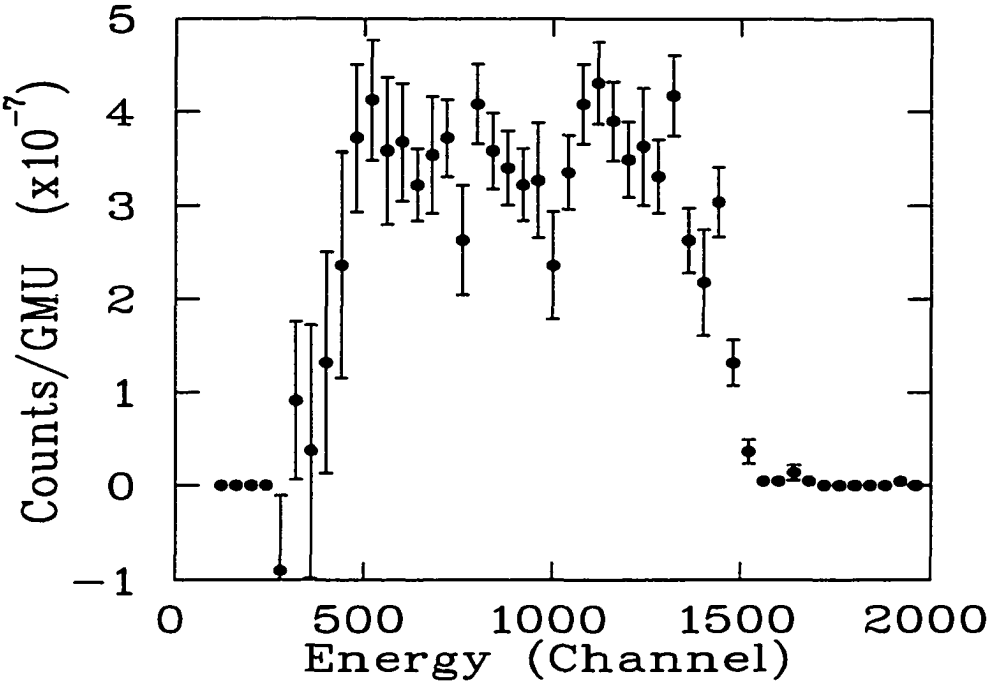

Figure 4.20: *An energy spectrum from detector N1 requiring the PSD and del-e conditions. The data shown are for runs 1949-56 in which the target consisted of a SEMT with a subtracted background determined by a SET target (runs 1944-45). The data are normalized per good muon (GMU).*

Figure 4.20 shows the energy spectrum from neutron detector N1 with the PSD and del-e conditions enforced. The data shown are from a target consisting of a SEMT with a subtracted background consisting of a 1000 T*l* SET target. The spectrum shown is due to fusions in the US target layer. The background was chosen to remove processes that may be occurring in the SET target which could contaminate the neutron fusion spectra. This is the same procedure followed using the silicon data to produce Fig. 4.11.

Shown in Fig. 4.21 is an energy spectrum from N1, again with the PSD and del-e

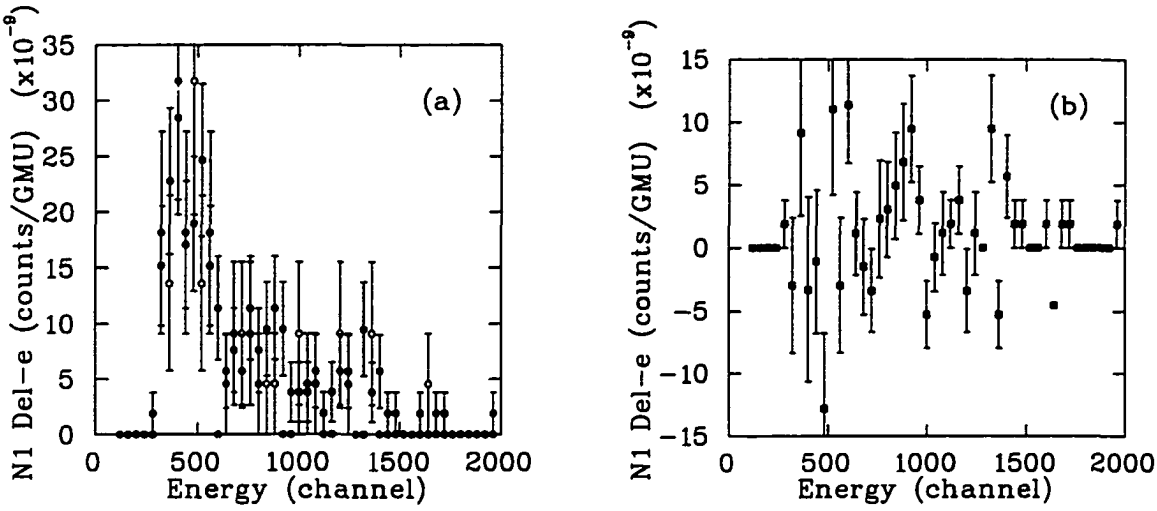

Figure 4.21: *Energy spectra from detector N1 with the PSD and del-e conditions met, (a), the filled circles correspond to a SEMT US and 3 Tl HD DS target. The hollow circles correspond to background (SEMT). Figure (b) shows the data depicted in (a) after background subtraction. Time cuts restricting all events between 1.5 and 6 μs after the arrival of the muon have been applied to all data shown.*

conditions applied. It is similar to Fig. 4.20 except for the time cut placed on the data and the different background subtraction. The fusion data is due to events occurring DS and. to ensure this, a time cut has been placed on the data, selecting only events which occur between 1.5 and 6 μs after the arrival of the muon in the target. The data and background have been plotted separately for comparison. The filled circles in Fig. 4.21 (a) depict data from a target consisting of a SEMT US and 3 T*l* *HD* DS. The hollow circles show the background corresponding to the SEMT target alone. The fusion signal and background seem indistinguishable. To clarify this, the background has been subtracted from the data and the result is shown in Fig. 4.21 (b).

This energy spectrum can be compared to the fusion spectra seen by the silicon detectors and depicted in Fig. 4.12. It is evident that the statistics for neutron fusion detection

are quite poor. The time-of-flight spectrum from detector N2 has similar statistics as N1 and does not add any new insight to the data already shown. When compared to the very large statistics seen with the silicon detector, it has been concluded that the neutron data will not add to the analysis of the DS time-of-flight fusion data. Therefore the neutron fusion data will not be analysed beyond this point.

4.6 Monte Carlo Code: Super Monte Carlo

The data acquired in the experiment must be compared to theory to gain a quantitative understanding of the energy-dependent rates which occur in the muon catalyzed fusion cycle. The most efficient way of making this comparison is through the use of a Monte Carlo code.

A Monte Carlo code called "Super Monte Carlo" (SMC) was developed by a Tom Huber at Gustavus Adolphus College in St. Peter, Minnesota; a collaborator of this experiment. The program simulates muonic processes which occur in the experiment, taking into account the dimensions and geometry of the apparatus, target thicknesses, and in some cases detector placement. The code relies on a user input file specifying the reactions which can occur in the simulation, the composition and location of solid targets used, along with either the energy dependent cross section or rate data for the reactions or, where applicable, energy independent reaction rates. The details are provided in the next sections.

4.6.1 Muonic Atoms

The first step in the simulation is the generation of a muonic atom. The creation takes place in the emission layer which consists of H_2 with a 0.1% T_2 concentration, thus the atoms created are either $p\mu$ atoms or $t\mu$ atoms according to the specified concentration. The creation of muonic atoms is uniform along the direction of the beam axis and the radial

distribution is a flat-topped Gaussian (see section 4.3). The initial energy of the muonic atoms is set to 1 eV and their initial direction is generated isotropically. The populations of hyperfine states is taken to be 75% F=1 $t\mu$ or $p\mu$ atoms and 25% F=0 $t\mu$ or $p\mu$ atoms due to the statistical filling of the hyperfine spin states.

4.6.2 Reactions In The Muon Catayzed Fusion Cycle

Given next is a description of the kinetic processes included in the Monte Carlo code. These processes are elastic scattering, spin flip, muon transfer, molecular formation (both resonant and nonresonant) and fusion. The theory employed to model these processes does not account for solid state interactions, where the muonic atoms interact with the crystal lattice. Solid state effects for energies above about 0.1 eV are expected to be minimal; however, under 0.1 eV these effects may become quite important [73]. Below 0.1 eV, the total cross sections do not correspond to those of free molecules and Bragg scattering from the crystal lattice occurs. In the energy range of interest for resonant muonic molecular formation on HD ($>$ 0.1 eV), nuclear scattering should supply a reasonable model for interactions occurring in the experiment and this has been used in the Monte Carlo.

The total and differential cross sections used in the simulation are from Refs. [38,74–76] and have been corrected for molecular effects [77,78]. The differential cross sections $\frac{d\sigma}{d\Omega}$ are given in terms of the derivative of the nuclear cross sections with respect to solid angle. This form is needed in order to simulate transport of the atoms and molecules through the target. Although solid state cross sections have been calculated, they are not yet in a form which permits inclusion in the Monte Carlo code. Experimentally measured energy-independent rates have been used for some processes, as detailed in the next sections.

Elastic Scattering

The symmetric elastic scattering reactions included in the Monte Carlo are:

$$\begin{aligned}
(p\mu)_F + p &\rightarrow (p\mu)_F + p \ , \ F = 0, 1 \\
(d\mu)_F + d &\rightarrow (d\mu)_F + d \ , \ F = \frac{1}{2}, \frac{3}{2} \\
(t\mu)_F + t &\rightarrow (t\mu)_F + t \ , \ F = 0, 1.
\end{aligned} \tag{4.28}$$

The reactions are considered symmetric due to scattering of equal mass nuclei (*i.e.* $p\mu$ on p, $d\mu$ on d, or $t\mu$ on t). The cross sections for these processes have been calculated for scattering on the nucleus itself with no electrons present.

The asymmetric collisions are also included in the code:

$$\begin{aligned}
(p\mu)_F + d &\rightarrow (p\mu)_F + d \ , \ F = 0, 1 \\
(p\mu)_F + t &\rightarrow (p\mu)_F + t \ , \ F = 0, 1 \\
(d\mu)_F + p &\rightarrow (d\mu)_F + p \ , \ F = \frac{1}{2}, \frac{3}{2} \\
(d\mu)_F + t &\rightarrow (d\mu)_F + t \ , \ F = \frac{1}{2}, \frac{3}{2} \\
(t\mu)_F + p &\rightarrow (t\mu)_F + p \ , \ F = 0, 1 \\
(t\mu)_F + d &\rightarrow (t\mu)_F + d \ , \ F = 0, 1.
\end{aligned} \tag{4.29}$$

Spin Flip

Only symmetric scattering causing a change of hyperfine state has been included in the simulation. This occurs by the transfer of a muon from one nucleus to the other involved in the collision. Asymmetric collisions causing spin flip on the other hand, can only take place due to a relativistic interaction which causes spin flip of the muonic atom. Calculations of the spin flip interaction show that asymmetric collisions contribute orders of magnitude less to spin flip than symmetric collisions so it is reasonable to disregard these interactions [14].

The following spin flip reactions have been included in the simulation:

$$\begin{aligned}
(p\mu)_{F=0} + p + 182\ meV &\rightarrow (p\mu)_{F=1} + p \\
(p\mu)_{F=1} + p &\rightarrow (p\mu)_{F=0} + p + 182\ meV \\
(d\mu)_{F=\frac{1}{2}} + d + 48.5\ meV &\rightarrow (d\mu)_{F=\frac{3}{2}} + d \\
(d\mu)_{F=\frac{3}{2}} + d &\rightarrow (d\mu)_{F=\frac{1}{2}} + d + 48.5\ meV \\
(t\mu)_{F=0} + t + 23.7\ meV &\rightarrow (t\mu)_{F=1} + t \\
(t\mu)_{F=1} + t &\rightarrow (t\mu)_{F=0} + t + 23.7\ meV.
\end{aligned} \tag{4.30}$$

Transfer

The muon transfer reactions in the computer code are:

$$\begin{aligned}
p\mu + d &\rightarrow d\mu + p + 135\ eV \\
p\mu + t &\rightarrow t\mu + p + 183\ eV \\
d\mu + t &\rightarrow t\mu + d + 48\ eV.
\end{aligned} \tag{4.31}$$

The transfer rate for the reaction $p\mu + t \rightarrow t\mu + p + 183\ eV$ has been measured by this collaboration to be λ_{pt}=5.86 $\times$ 10^9 s^{-1} and is used in the Monte Carlo [79]. The other transfer reactions in Eq. (4.31) use the nuclear cross section tables mentioned earlier.

Constant rates are used to represent muon transfer from a muonic atom to a nonhydrogenic atom. One such case is the muon transfer to gold, important since the experimental apparatus contains a large amount of gold. The transfer rate is taken to be 1 $\times$ 10^{12} s^{-1}, fast enough to ensure a rapid transfer in the simulation. Transfer to nitrogen has also been included in the code to estimate the effect of this contamination on the total fusion yield. The rate for transfer of the muon from a $t\mu$ atom to N_2 is not known as it has never been measured. Therefore, the value of muon transfer from $d\mu$ to N_2, measured to be 0.145 $\times$ 10^{12} s^{-1} [80] was used. With an upper limit of 0.05% nitrogen contamination in the

HD target (which corresponds to a value of 1.7×10^{-4} counts/GMU in the x ray spectra discussed in section 3.4.3), the simulation shows a 2% loss of fusion events due to muons transferring to nitrogen.

$$h\mu(h = p, d, t) + N \rightarrow N\mu + h \tag{4.32}$$

Nonresonant Molecular Formation

Nonresonant molecular formation can occur in the simulation by the following reactions

$$\begin{aligned}
p\mu + p &\rightarrow pp\mu, \ \lambda_{pp\mu} = 3.2 \times 10^6 s^{-1} \\
d\mu + p &\rightarrow pd\mu, \ \lambda_{pd\mu} = 5.6 \times 10^6 s^{-1} \\
t\mu + p &\rightarrow pt\mu, \ \lambda_{pt\mu} = 6.5 \times 10^6 s^{-1} \\
d\mu_{\frac{1}{2}} + d &\rightarrow dd\mu, \ \lambda_{dd\mu} = 0.052 \times 10^6 s^{-1} \\
d\mu_{\frac{3}{2}} + d &\rightarrow dd\mu, \ \lambda_{dd\mu} = 3.21 \times 10^6 s^{-1} \\
t\mu + t &\rightarrow tt\mu, \ \lambda_{tt\mu} = 2.0 \times 10^6 s^{-1}
\end{aligned} \tag{4.33}$$

producing $pp\mu$, $pd\mu$, $pt\mu$, $dd\mu$ and $tt\mu$ molecules [15, 23, 79, 82]. These calculated rates do not depend strongly on energy [23] thus constant rates have been used in the Monte Carlo. The nonresonant molecular formation of $dt\mu$ molecules is included in the files which describe resonant molecular formation (described below) and thus does not need to be included separately into the Monte Carlo. The formation of $tt\mu$ molecules in our target which consists of 0.1% tritium is not very likely when compared to $pt\mu$ formation as the target consists of 99.9 % protium. The formation of $dd\mu$ molecules is a process which is not very likely either but has been included to test for background effects.

Resonant Molecular Formation

The resonant molecular formation rates are pertinent to the simulation as this is the key step in $dt\mu$ fusion, which the time-of-flight data is sensitive to. The processes included in SMC are given by

$$\begin{aligned}(t\mu)_F + D_2(ortho)_{\nu_i K_i} &\rightarrow [(dt\mu)dee]_{\nu_f K_f} \ , \ F = 0,1 \\ (t\mu)_F + D_2(para)_{\nu_i K_i} &\rightarrow [(dt\mu)dee]_{\nu_f K_f} \ , \ F = 0,1 \end{aligned} \tag{4.34}$$

$$(t\mu)_F + HD_{\nu_i K_i} \rightarrow [(dt\mu)pee]_{\nu_f K_f} \ , \ F = 0,1 \tag{4.35}$$

Due to the various layers of frozen hydrogen isotopes in the experiment, resonant molecular formation occurs in both D_2 and HD. The rates used in the code have been calculated by Faifman *et al.* [20, 22, 34, 36] using isolated molecules at a temperature of 3 K and an interaction potential truncated after quadrupolar terms. The rates of molecular formation have been calculated for an incident $t\mu$ energy varying from 0 to 2 eV. In calculating the rates for Eq. (4.34), the initial vibrational state of the D_2 molecule was taken to be ν_i=0 with the final vibrational state of the molecular complex being ν_f=3. For Eq. (4.35), the initial vibrational state of the of the HD molecule was taken as zero while the final state of the six body molecule was given by ν_f=2. Both calculations took into account the different hyperfine states of the atoms, using several rotational levels and accounting for ortho and para differences in the homonuclear D_2 target molecules. An ortho/para D_2 concentration was chosen to be 66.6% ortho D_2 (J=0) and 33.3% para D_2 (J=1) in the simulation (the same as the populations at room temperature [4]). This ortho-para concentration was chosen due to the procedure in which the target gas was deposited. The deposition involves a rapid freezing of the gas and, since the homonuclear hydrogens are forbidden (in first order) to have ΔJ=1 rotational transitions, this assumption is well justified [4].

When a muonic molecule is formed via resonant formation there is a possibility that "back decay" can occur and the processes given in Eq. (4.34) and Eq. (4.35) will reverse themselves. For example,

$$[(dt\mu)pee]_{\nu K} \rightarrow (t\mu)_F + HD_{\nu' k'} \tag{4.36}$$

and the hyperfine state of the $t\mu$ is the same as it was before molecular formation occurred. The energy of the $t\mu$ atom, which can be varied in the simulation, was set to 1 meV, although increasing this energy to 100 meV produced only a 3% difference in total simulated fusion yield.

Fusion

After molecular formation, the fusion process given by

$$(dt\mu) \rightarrow \mu + n + {}^4\mathrm{He} + 17.6 \ \ \mathrm{MeV} \tag{4.37}$$

competes with the back decay process. If fusion occurs, it releases 17.6 MeV of energy at a rate of 1.3×10^{12} s^{-1} [15].

4.6.3 Reaction Selection and Particle Propagation

All processes need to be described in a similar fashion before deciding on what process the muonic atom will undergo. To ensure this, all cross sections are converted to rates:

$$\lambda(i) = \sigma(i)\nu\phi N_0 \tag{4.38}$$

where $\lambda(i)$ is the rate for the ith process, $\sigma(i)$ is the cross section, ν is the relative velocity between the target and projectile, and ϕN_0 is the atomic number density of the scattering medium. In the code, the time between reactions is given by

$$REACTIME = -\frac{log(randval)}{\sum_i^j \lambda(i)} \tag{4.39}$$

where $REACTIME$ is the time between reactions, and *randval* is a random number between zero and one (the sum of all possible processes is given by $\sum_i^j \lambda(i)$). The distance to the reaction and the position where the reaction will occur is then calculated. A decision on what reaction process occurs must then be made. For the given projectile, the probability of undergoing a certain process i is given by

$$P(i) = \frac{\lambda(i)}{\sum_i^j \lambda(i)}. \tag{4.40}$$

A random number is generated between zero and $\sum_i^j \lambda(i)$ and the chosen process is the one which corresponds to the cumulative probability which is less than this random number. The projectile is then moved to this new position and the time is incremented. The kinetics governing the chosen process are calculated and the particle which emanates from this process is allowed to continue in the muon catalysis cycle. This process continues until a dead end is encountered such as fusion, muon decay, sticking, nuclear capture or another process in which the particle is lost. Then a random number is generated to decide if the muon will be regenerated and allowed to begin a new cycle of fusion or will be stuck to the helium produced by fusion. If regeneration is selected, a new muonic atom is formed based on the current scattering material. If however the muon is not regenerated, a μHe atom at rest is formed and will remain at rest until it decays.

4.7 $t\mu + D_2$ Resonant Molecular Formation

To study $t\mu + D_2$ resonant molecular formation, targets were deposited during the July 1996 experiment to correspond in thickness and composition to targets used in the July 1994 experiment. These data runs along with the target conditions are listed in Table 4.11. As mentioned in section 3.1, during some of the 1996 target depositions, difficulties arose with the gas diffuser, resulting in less gas being frozen onto the target foils than intended.

Year	Run #	Target US (Tl)	Target DS (Tl)	GMU (10^6)
1994	1630-31	SET $\oplus$ 3 D_2	20 D_2	48.3
1994	1635	SET $\oplus$ (3+3=6) D_2	20 D_2	50.4
1994	1640	SET $\oplus$ (3+3+8=14) D_2	20 D_2	33.5
1996	1908	SET $\oplus$ 2.2* D_2	20 D_2	23.4
1996	1910	SET $\oplus$ (2.2+1.8+5=9*) D_2	20 D_2	22.4
1996	1911-12	SET $\oplus$ (2.2+1.8+5+3=12*) D_2	20 D_2	36.0
1996	1946-47	SET $\oplus$ 3 D_2	-	7.7
1996	1948	SET $\oplus$ (3+5=8) D_2	-	5.0
1996	1949-56	SET $\oplus$ (3+5+2=10) D_2	-	220.3
1996	1977-79	SET $\oplus$ (3+5+2+4=14) D_2	7 HD $\oplus$ 20 D_2 $\oplus$ 300 HD	68.2

Table 4.11: *Data runs of July 1994 and 1996. The * indicates runs in which the diffuser was clogged and the thicknesses have been corrected for this effect.*

Before the resonant molecular formation rates can be studied, a determination of how much gas was deposited during the runs in which the diffuser was clogged must be undertaken.

To correct the target thicknesses, experimental data taken while the gas diffuser was in excellent working order have been compared to computer simulations using SMC. The data were analyzed with respect to fusion yield for targets of known thicknesses. Using SMC, a theoretical value of the fusion yield could also be determined. The ratio of experimental fusion events to simulated fusion events ($F_{\frac{E}{S}}$) could then be determined for targets of various thicknesses. The data taken with unknown target thicknesses were analyzed and simulations were done assuming no gas lost during the target deposition. By comparing the ratio $F_{\frac{E}{S}}$ for an unknown target thickness to $F_{\frac{E}{S}}$ for known target thicknesses, an estimate of how much gas was lost could be determined. The simulation would then be run again with this new value of target thickness and the resultant $F_{\frac{E}{S}}$ ratio compared to the known target thickness $F_{\frac{E}{S}}$ ratio. This method was repeated, using a different target thickness in the simulation until $F_{\frac{E}{S}}$ from the unknown target thickness corresponded within statistical uncertainty to $F_{\frac{E}{S}}$ from the known target thickness.

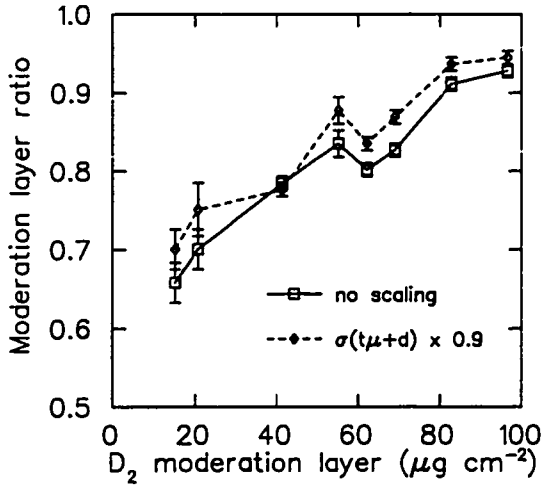

Figure 4.22: *Ratio of experimental to simulated fusion events ($F_{\frac{E}{S}}$) in the US D_2 moderator layer vs. moderator layer thickness. The effect of scaling the $t\mu + d$ cross section by 0.9 on US fusion is also plotted.*

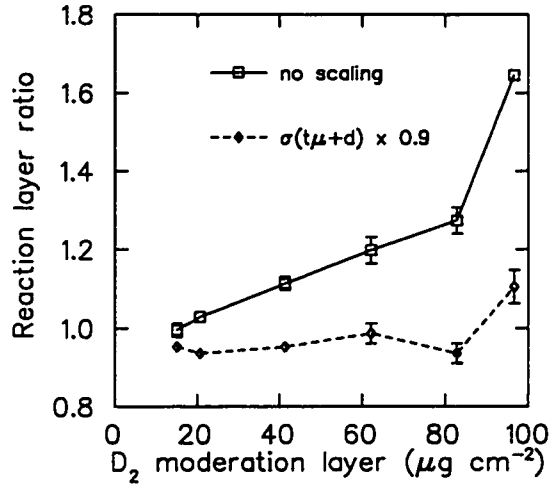

Figure 4.23: *Ratio of experimental to simulated fusion events ($F_{\frac{E}{S}}$) in the 20 Tl (140 $\mu g\ cm^2$) DS D_2 reaction layer vs. moderator layer thickness. The effect of scaling the $t\mu + d$ cross section by 0.9 is also plotted.*

The corrected target thicknesses are given in Table 4.11. To determine the target thickness for run 1908, runs 1630-31 and 1946-47 were used as a comparison for the $F_{\frac{E}{S}}$ ratio of US fusion. Runs 1630-31 were also used to make a comparison of $F_{\frac{E}{S}}$ of DS fusion. To make the thickness correction for run 1910, runs 1948 and 1949-56 were used for the $F_{\frac{E}{S}}$ ratio of fusion occurring US. Finally, the target thickness during runs 1911-12 was determined by comparison of the US fusion ratio to runs 1949-56, 1977-79 and 1640. Run 1640 was used as well for a comparison of the DS fusion ratio.

The ratio of experimental to simulated fusion yield for all runs given in Table 4.11 has been plotted as a function of US D_2 moderator layer thickness in Fig. 4.22 for US fusion and Fig. 4.23 for DS fusion. The effects of the solid angle of both silicon detectors and the

muon stopping fraction were necessary for and have been included in the calculated ratio $F_{\frac{E}{S}}$. The results have been plotted as a function of moderator layer thickness to search for any systematic trends which reveal weaknesses in the SMC simulation. A simulation with no systematic uncertainties, which accurately depicts the experiment would result in a ratio of unity, hence both plots would have zero slope. Because each ratio contains the same scaling factors, detector solid angle and stopping fraction, any inaccuracies in these numbers would shift each ratio uniformly from unity, thus an observed slope must be due to incorrect modelling of muonic reactions [69]. The trend in Fig. 4.22 is for the Monte Carlo simulation to be overestimating fusion in the US (especially in the thin) layers. However, in Fig. 4.23, SMC is underestimating fusion, except for the thin layers.

The muonic process which was studied in great detail and had a significant effect on the DS fusion results was the $t\mu+d$ scattering cross section. Several simulations were performed with this cross section scaled between 25% to 90% of its original value. Fig. 4.23 shows the dramatic flattening of the slope by changing this cross section by just 10%. However, it is clear from Fig. 4.22 that this does not solve the discrepancies in the US fusion ratios. By scaling the $t\mu+d$ scattering cross section to 90% of its original value, the $t\mu$ atoms in the D_2 moderator layer will undergo less scattering, therefore less energy loss and fusion will occur US. Thus, it is expected that the ratios $F_{\frac{E}{S}}$ for US fusion would increase. Because there is simply less fusion occurring US, this leaves more $t\mu$ atoms at a higher speed able to survive the flight into the DS reaction layer, implying more fusion will occur DS and hence the ratios $F_{\frac{E}{S}}$ in Fig. 4.23 will decrease. The net effect is to decrease the slope of the reaction layer ratios. Clearly all muonic processes occurring are interconnected and scaling of just one reaction cross section allows for quite satisfactory comparison of the experimental data to SMC simulations for DS fusion. However, something more subtle and yet undetermined is occurring as well in the US moderator layer. Clearly by scaling the $t\mu + d$ scattering

cross section by 90%, we change the energy distribution of the emitted $t\mu$ atoms into a distribution in good agreement with the experimental results. It should be noted that the error bars quoted are only statistical.

4.8 $t\mu + HD$ Resonant Molecular Formation

To study $t\mu + HD$ resonant molecular formation, data from targets which were deposited during the 1996 experiment were analyzed. Approximately 90% of data were taken with a SEMT upstream. Three different thicknesses of downstream HD targets were analyzed— 3, 7 and 300 Tl. The resultant time-of-flight spectra were then compared to Monte Carlo (SMC) simulation results in which certain specific input parameters were varied.

Plotted error bars are statistical for figures contained in this section, however systematic errors were included in determining results presented in chapter 5.

The fusion time distribution shown in Fig. 4.24 corresponds to fusion occurring in the upstream 10 Tl D_2 moderator layer and is shown on a log scale. A time cut of $0 < t < 1.5\ \mu s$ has been placed on the data to restrict fusion events to those occurring US. Background of a SET (Standard Emission Target) has been subtracted (discussed in the Time-of-Flight section of chapter 4). The SMC reproduces the physics occurring in this 10 Tl D_2 target quite well.

The fusion time distribution for the 3 Tl HD target is shown in Fig. 4.25. The molecular formation rates $\lambda_{dt\mu-p}$ have been appropriately scaled by a factor 0.5 (as discussed in Appendix A) for the SMC input. The time cut chosen ($1.5 < t < 6\ \mu s$) restricted events to fusion occurring in the HD layer downstream. Background determined from a SEMT has been subtracted (again see the Time-of-Flight section in chapter 4). The dark line is the simulated total fusion spectrum while the light line shows the contribution to fusion from direct molecular ion formation processes only. Recall that these processes are ones

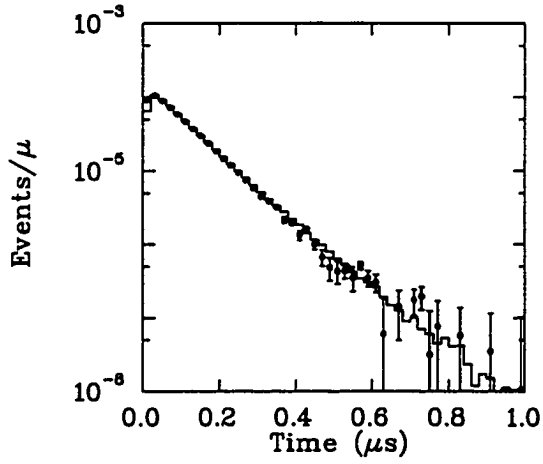

Figure 4.24: *Fusion (alpha product) time distribution normalized to the number of incident muons for an upstream moderation target of 1000 SET ⊕ 10 Tl D_2 (SEMT). The histogram is from SMC while the data is plotted as solid dots.*

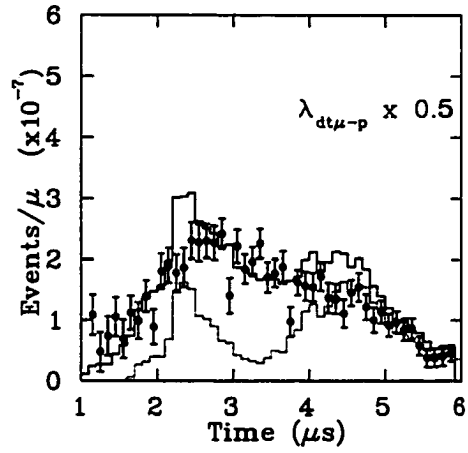

Figure 4.25: *Fusion (alpha product) time distribution normalized to the number of incident muons for a reaction layer of 3 Tl HD. The dark line is total alpha fusion from all processes while the light line is the contribution to fusion only from direct molecular ion formation processes. The data is plotted as solid circles.*

in which the $t\mu$ atom does not undergo energy loss before molecular formation occurs. To make all comparisons between SMC and the data, the silicon detector solid angle and hydrogen stopping fraction, discussed in sections 4.2.1 and 4.4, have been included in the calculations. The pronounced two-peak structure predicted by SMC does not appear in the data. Figure 4.26 (a) depicts the fusion time distribution for the 7 T*l* *HD* target and (b) shows the background-subtracted fusion time distribution for the 300 T*l* *HD* target. The 7 T*l* *HD* data are in reasonable agreement with the simulated results however the very thick 300 T*l* *HD* data are not. The Super Monte Carlo underestimates by about a factor of two the fusion yield in the 300 T*l* case. The shapes of the fusion time distributions in the 7 T*l*

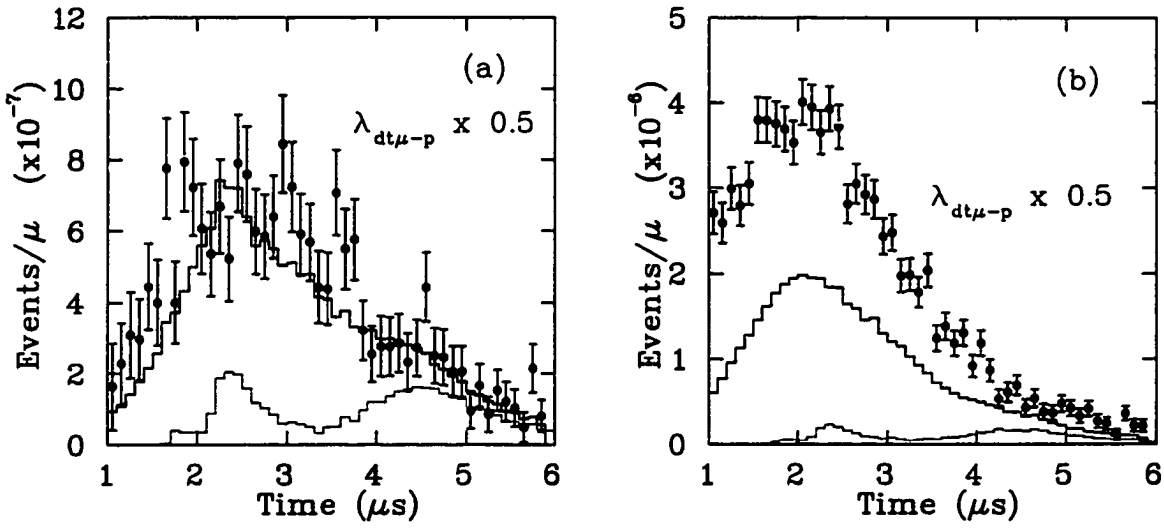

Figure 4.26: *Fusion time distributions normalized to the number of incident muons for a reaction layer of (a) 7 Tl HD and (b) 300 Tl HD. The dark line is total alpha fusion from all processes while the light line is the contribution to fusion only from direct molecular ion formation processes. The data are shown as solid circles.*

and 300 T*l* targets resemble the shape predicted by the Monte Carlo, however the thin 3 T*l* data does not match the two-peaked shape predicted by the code.

The dependence on the fusion yield and the shape of the fusion time histogram with respect to the energy of the molecular formation resonant peaks was then investigated. The theoretically predicted resonant molecular formation rate for $t\mu+HD$ scaled by 0.5 is shown in Fig. 4.27. For each hyperfine state of the $t\mu$ atom, the mean and standard deviation of each resonant peak was found. The calculated average standard deviation of the resonances was $\sim$ 0.18 eV for each hyperfine state. To determine the sensitivity of the fusion yield to these peak energies, the resonances were shifted 0.18 eV higher and lower in the input to SMC. Results are shown in Fig. 4.28 for $\lambda_{dt\mu-p} \times 1.0$ (twice the nominal value of scaling, chosen to enhance the direct formation mechanism and effect of the shift) and in Fig. 4.29 for the nominal value of scaling.

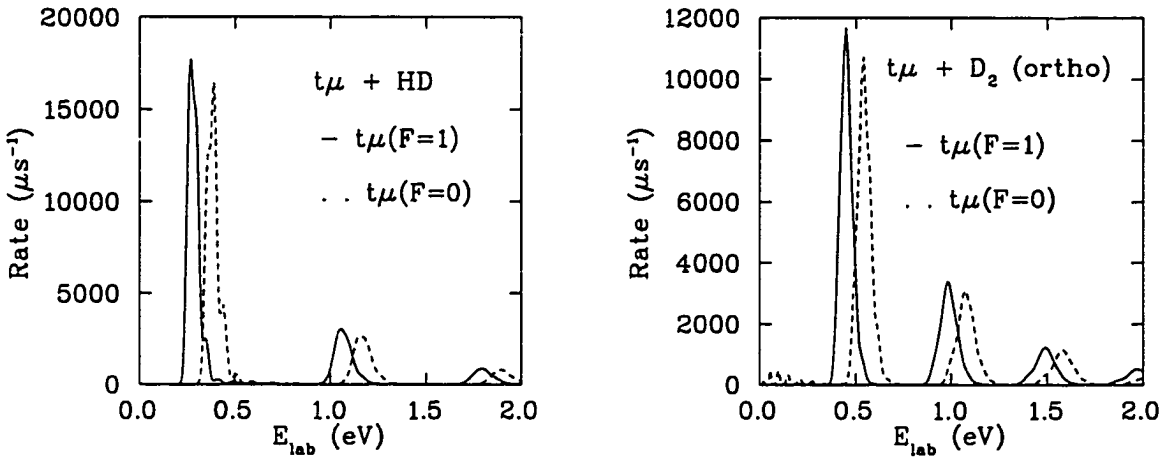

Figure 4.27: *The theoretically predicted molecular formation rate as a function of $t\mu$ lab energy for the resonant structures of $t\mu + HD \rightarrow [(dt\mu)pee]$ and for $t\mu + D_2 \rightarrow [(dt\mu)dee]$ calculated at 3 K by M.P. Faifman. The resonant structures for D_2 are shown for comparison. Note that the rates for HD have been multiplied by the normalization factor of 0.5.*

By choosing twice the nominal rate, the effect of shifting the resonance positions by $\pm$ 0.18 eV (shown in Fig. 4.28) is exaggerated because the intensities of the resonance peaks are twice as large. By shifting the resonant peaks to higher energies the contribution to fusion at late times (4 to 6 μs) is underestimated and the peak which appeared in the original simulation between 4 and 5 μs appears at an earlier time with greater intensity (see Fig. 4.29). By shifting the resonances to higher energies, it was expected that the peaks in the fusion time distribution would appear at earlier times because of the inverse relation between time-of-flight and energy of the $t\mu$ atom (discussed in section 4.5). Thus, the contribution from the lower energy, but highest-molecular-formation-rate resonance has been shifted into a range where it now contributes strongly. This can also be seen in the simulation of the contribution to fusion from direct formation.

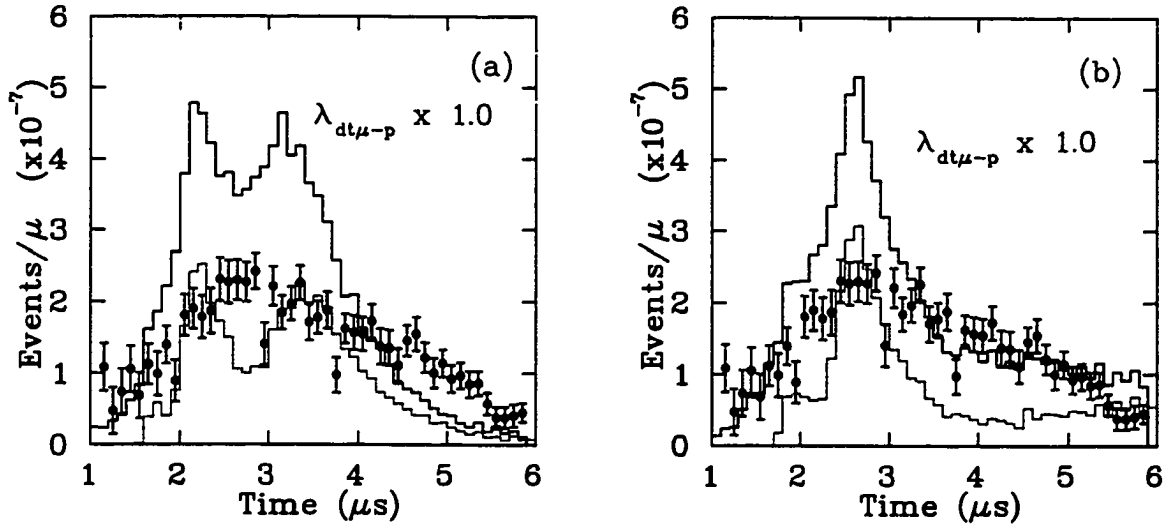

Figure 4.28: *Fusion time distributions for a reaction layer of 3 Tl HD. The input to SMC used the $t\mu + HD$ molecular formation resonances which were shifted by 0.18 eV to (a) higher energies and (b) lower energies. The dark line is total fusion from all processes while the light line is the contribution to fusion from direct processes in the reaction layer. Data are plotted as solid dots.*

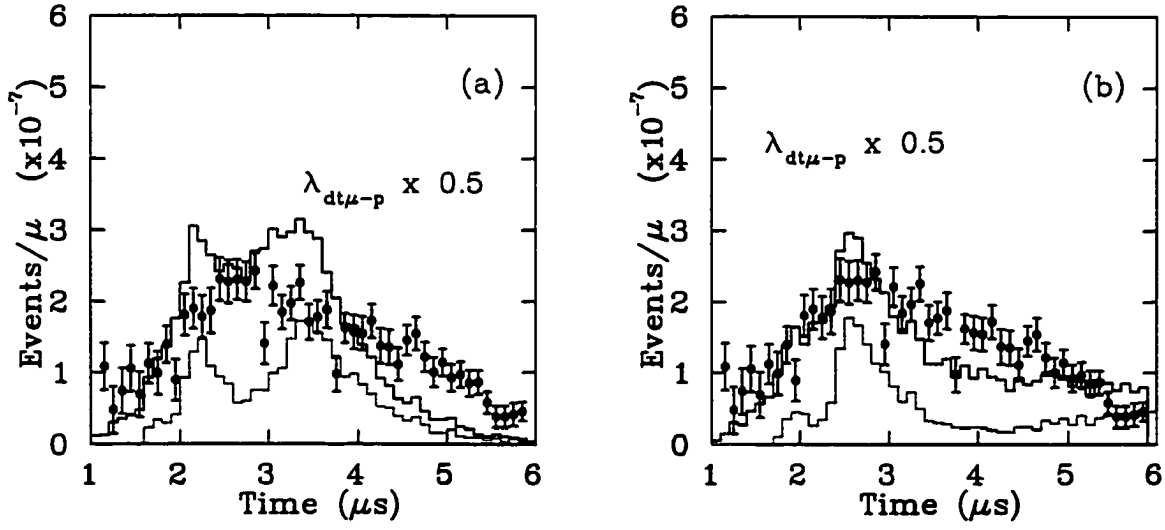

Figure 4.29: *Fusion time distributions for a reaction layer of 3 Tl HD. The input to SMC used the $t\mu + HD$ molecular formation resonances which were shifted by 0.18 eV to (a) higher energies and (b) lower energies. Data are plotted as solid dots.*

Shifting the resonances to lower energy has the opposite effect. The contribution from the high energy resonances is not greatly affected, however the contribution from the low energy resonance is suppressed. This is also verified by the small contribution of direct formation to total fusion yield between 4 and 6 μs since this late time range corresponds to the low energy resonance. The peak in the time distribution between 2 and 3 μs is shifted to slightly greater times, indicative of the resonances occurring at smaller energies.

Shown in Fig. 4.29 are the results of shifting the resonances by $\pm$ 0.18 eV while using the nominal rate of $\lambda_{dt\mu-p} \times 0.5$. Shifting the resonances to higher energies has the same effect as in Fig. 4.28, but with the SMC intensity smaller due to the reduced molecular formation rates, thus more in agreement with the data. Shifting the resonances to lower energies results in an SMC simulation which resembles the data, but underestimates fusion between 3 to 5 μs. The same procedure was also followed for the 7 Tl HD targets with similar results, given in Fig. 4.30.

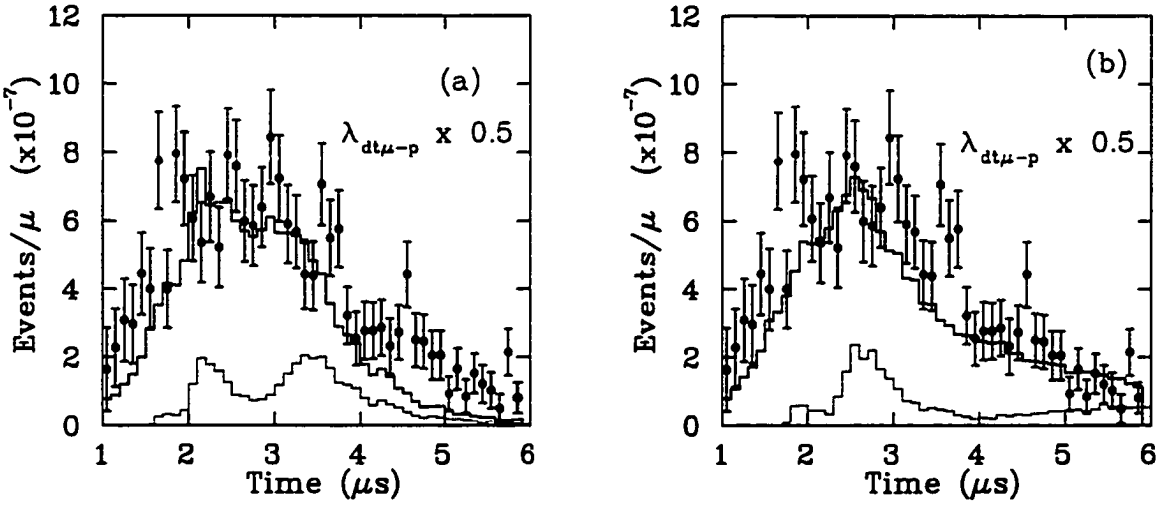

Figure 4.30: *Fusion time distributions for a reaction layer 7 Tl HD. The input to SMC used the $t\mu + HD$ resonant formation cross section shifted in energy by (a) 0.18 eV and (b) -0.18 eV.*

The Super Monte Carlo code reproduces the downstream fusion yield for D_2 targets rather well with a scaling of $\sigma_{t\mu+d} \times 0.9$. During the week in which all of the HD data was collected, a 20 Tl D_2 target were deposited on top of the 7 Tl HD target. This data is shown compared to the simulation in Fig. 4.31. According to the SMC, the contribution to the total fusion time spectrum from fusion occurring in the underlying HD layer is approximately 3.6% —so minimal that it is not visible in the plot. The simulation reproduces the D_2 fusion data quite well. From this good agreement for D_2 and the results of the previous section, it is clear that the discrepancy between SMC and the thick HD data results from the physics processes implemented in SMC for HD.

Some of the changes made to the SMC input parameters to test their effect on the simulated fusion results are summarized in Table 4.12. For each downstream target thickness, changes were made to SMC input and the results of (i) the ratio of fusion yield to simulated fusion yield, (ii) a fit of SMC results to the data allowing the scaling factor between the two to vary, (iii) the associated χ^2/dof of the fit are shown along with (iv) the fit of SMC to the data and the associated χ^2/dof of the fit when the scaling factor between the two is fixed at a value of one. The first results tell us how close we are to a scaling factor of one between SMC and data. The results of the second fit, in which the scaling factor is held constant, gives us an idea of how well the simulation is reproducing the shape of the data.

The results of scaling $\lambda_{dt\mu-p}$ by 1.00 for the 300 Tl HD target are shown in Fig. 4.32 (a). Scaling $\lambda_{dt\mu-p}$ by 0.5 and $\sigma_{t\mu+d}$ by 0.9 are shown in Fig. 4.32 (b). Clearly, in the 300 Tl HD case, the simulation underestimates the fusion and including the scaling of the $t\mu+d$ cross section does not resolve this discrepancy. To determine important effects in the thicker target, compared to the thin targets, we must examine the $t\mu$ atom energies where the fusion processes are occurring. In the thinner targets, the contribution to fusion from direct formation is quite high, which is not the case in the thick target. This means that

the $t\mu$ atoms arriving at the downstream 300 Tl target lose a significant amount of energy before molecular formation occurs.

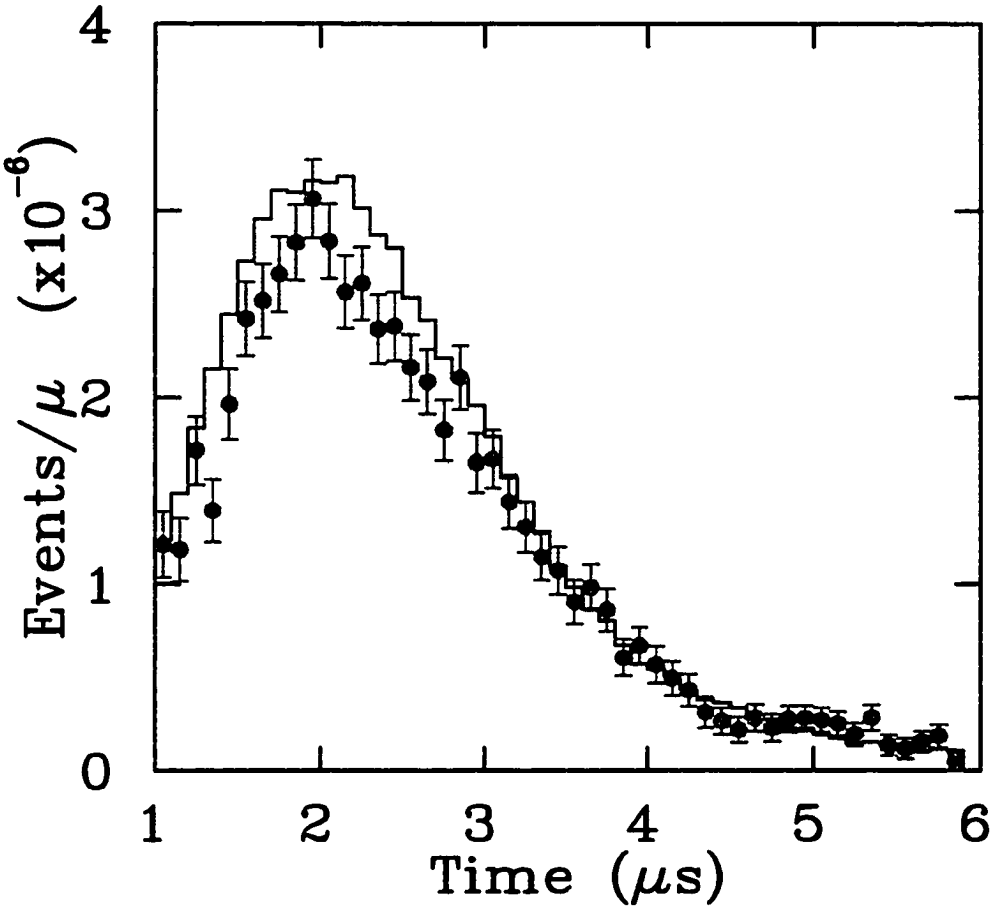

Figure 4.31: *Fusion time distribution for a reaction layer of 20 Tl D_2 frozen on top of the 7 Tl HD layer. The contribution to total fusion from the HD layer is minimal ($\sim$ 3.6 %) and is not visible on the plot. Thus, the resonant molecular formation rate for $t\mu + D_2$ is the dominating rate for $dt\mu$ fusion.*

DS Target (Tl)	MC Changes	Y_D/Y_{MC}	Fit Ratio D/MC	χ^2/dof	χ^2/dof (D/MC)=1
3 HD	$\lambda_{dt\mu-p} \times 0.5$	0.892(26)	0.839(31)	1.93	2.77
3 HD	$\lambda_{dt\mu-p} \times 0.5 + 0.18\ eV$	0.993(29)	0.804(56)	5.84	6.84
3 HD	$\lambda_{dt\mu-p} \times 0.5 - 0.18\ eV$	1.15(3)	1.04(5)	2.99	3.00
3 HD	$\lambda_{dt\mu-p} \times 0.5$,$\sigma_{t\mu+d} \times 0.9$ + $\lambda^{NR}_{dt\mu-p}$=0.56 μs^{-1}	0.842(24)	0.806(29)	1.62	3.02
3 HD	$\lambda_{dt\mu-p} \times 1.0$	0.635(18)	0.608(23)	1.99	11.9
3 HD	$\lambda_{dt\mu-p} \times 1.0 + 0.18\ eV$	0.691(20)	0.561(40)	6.27	17.8
3 HD	$\lambda_{dt\mu-p} \times 1.0 - 0.18\ eV$	0.781(22)	0.693(38)	4.00	8.00
3 HD	$\lambda_{dt\mu-p} = 200\ \mu s^{-1}$	1.07(3)	1.03(5)	2.99	2.98
7 HD	$\lambda_{dt\mu-p} \times 0.5$	1.23(5)	1.14(5)	1.27	1.47
7 HD	$\lambda_{dt\mu-p} \times 0.5 + 0.18\ eV$	1.41(5)	1.18(7)	2.37	2.67
7 HD	$\lambda_{dt\mu-p} \times 0.5 - 0.18\ eV$	1.28(5)	1.16(5)	1.53	1.79
7 HD	$\lambda_{dt\mu-p} \times 0.5$,$\sigma_{t\mu+d} \times 0.9$ + $\lambda^{NR}_{dt\mu-p}$=0.56 μs^{-1}	1.09(4)	1.02(4)	1.27	1.25
7 HD	$\lambda_{dt\mu-p} \times 1.0$	0.939(34)	0.862(38)	1.40	1.73
7 HD	$\lambda_{dt\mu-p} = 200\ \mu s^{-1}$	1.05(4)	0.998(37)	0.970	0.970
300 HD	$\lambda_{dt\mu-p} \times 0.5$	2.12(3)	2.02(5)	3.15	27.4
300 HD	$\lambda_{dt\mu-p} \times 0.5$,$\sigma_{t\mu+d} \times 0.9$	1.69(2)	1.64(3)	1.93	16.5
300 HD	$\lambda_{dt\mu-p} \times 0.5$,$\sigma_{t\mu+d} \times 0.9$ + $\lambda^{NR}_{dt\mu-p}$=0.56 μs^{-1}	1.14(2)	1.09(3)	2.90	3.47
300 HD	$\lambda_{dt\mu-p} \times 0.5$,$\sigma_{t\mu+d} \times 0.9$ + $\lambda^{NR}_{dt\mu-p}$=0.28 μs^{-1}	1.31(2)	1.24(3)	2.95	6.48
300 HD	$\lambda_{dt\mu-p} \times 1.0$	1.77(3)	1.68(5)	3.69	19.0
300 HD	$\lambda_{dt\mu-p} = 200\ \mu s^{-1}$	0.792(11)	0.744(20)	3.39	13.4
300 HD US Target SET $\oplus$ 14 D_2	$\lambda_{dt\mu-p} \times 0.5$ $\sigma_{t\mu+d} \times 0.9$ + $\lambda^{NR}_{dt\mu-p}$=0.56 μs^{-1}	1.18(3)	1.06(5)	3.51	3.56
//	$\lambda_{dt\mu-p} \times 0.5$, $\sigma_{t\mu+d} \times 0.9$ + $\lambda^{NR}_{dt\mu-p}$=0.28 μs^{-1}	1.36(3)	1.23(5)	3.14	4.39
//	$\lambda_{dt\mu-p} \times 1.0$	2.11(5)	1.86(9)	4.03	12.1
//	$\lambda_{dt\mu-p} = 200\ \mu s^{-1}$	0.882(20)	0.771(38)	4.37	7.43

Table 4.12: *The target thickness, changes in the SMC input, a ratio of data yield to simulated yield with a fit of the SMC results to the data allowing the scaling factor between the two to vary and the associated χ^2/dof for the fit. Also listed are the fit results of SMC to the data with the scaling factor held fixed at 1.00, along with the χ^2/dof for the fits.*

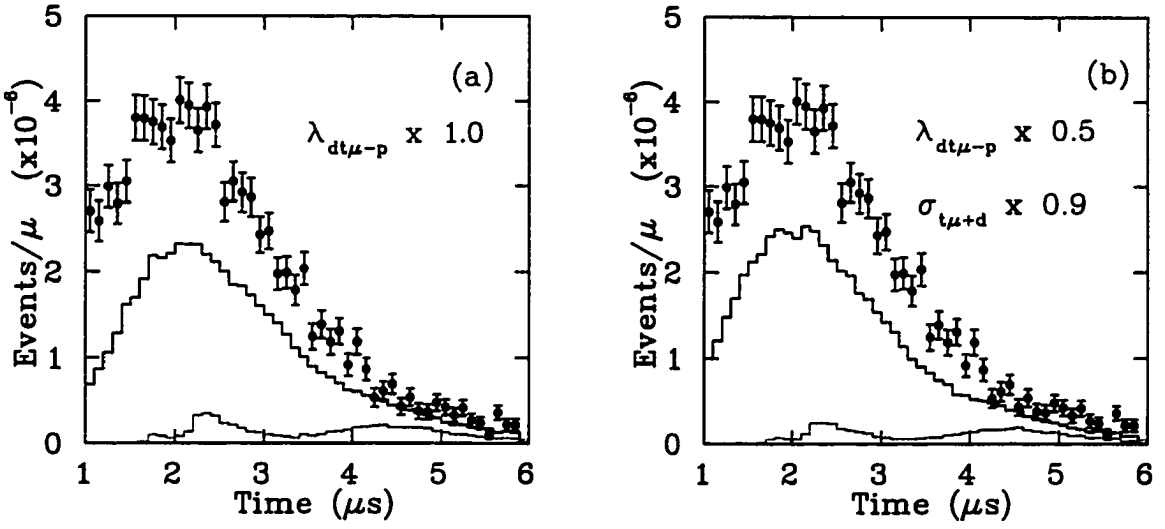

Figure 4.32: *Fusion time distributions for a reaction layer of 300 Tl HD. The input to SMC used (a)* $\lambda_{dt\mu-p} \times 1.0$ *and (b)* $\lambda_{dt\mu-p} \times 0.5$, $\sigma_{t\mu+d} \times 0.9$.

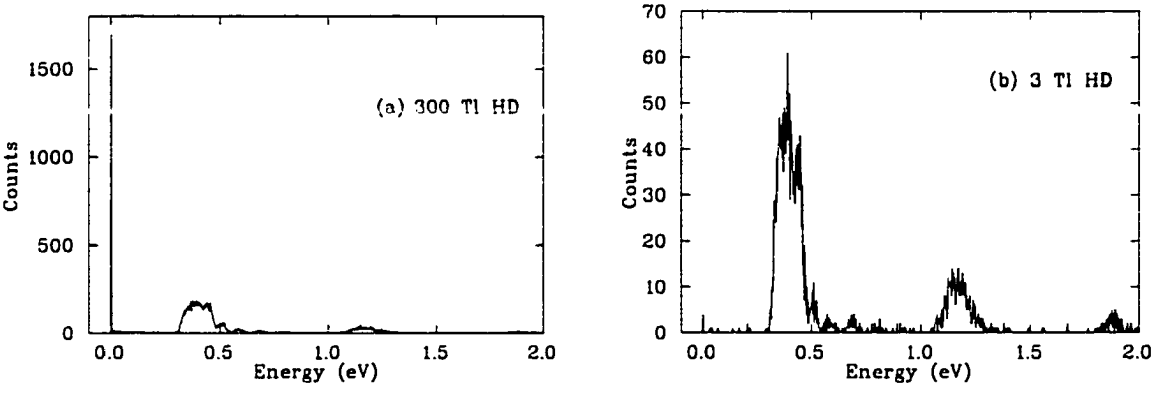

Figure 4.33: *The energy at which molecular formation takes place, simulated by SMC for (a) a 300 Tl HD target and (b) a 3 Tl HD target. A significant amount of molecular formation in the 300 Tl target takes place at energies close to zero (approximately 0.003 eV).*

The energy at which molecular formation occurs may be obtained from the SMC calculation. Shown in Fig. 4.33 is the $t\mu$ atom energy at which molecular formation takes place [22] for two target thicknesses. The energy (at which a significant contribution to fusion occurs) in the thin 3 Tl HD target is between 0.3 and 0.5 eV, which corresponds to the largest resonance peak in Fig. 4.27 with rates as high as $1.8 \times 10^{10} s^{-1}$. However, in the 300 T$l$ HD target, a significant contribution to fusion occurs at the much lower energy of about 0.003 eV (the first energy bin in SMC). In the rate table used in SMC, this corresponds to a resonant molecular formation rate of 0.13 μs^{-1}. In Chapter 2, it was shown that $dt\mu$ molecules can also be formed via a nonresonant process (see Eq. (2.6)). For very thin HD targets this nonresonant rate is negligible because the energy of $t\mu$ atoms in the HD layer is much higher and the resonant rates dominate in this energy region. This is not the case for thick targets. The calculated nonresonant rate for $t\mu$ atoms of 0.007 eV is $\lambda^{NR}_{dt\mu-p}$=0.56 μs^{-1} and is much higher than the resonant rate at this energy [23]. Although the resonant molecular formation tables used by SMC have the nonresonant rates included, averaging over the thermal motion of the hydrogen molecules and having the rates approach zero at 0 eV energy makes the values in the tables quite small at low energies. Maxwell-averaging over HD molecular motion is valid for gaseous HD but not for solid HD. Thus, it may be justified to examine the effect of adding an extra constant nonresonant rate for molecular formation. The rate $\lambda^{NR}_{dt\mu-p} = 0.56\ \mu s^{-1}$ has been added to the SMC input to determine its effect for the thick HD data comparison. Note that this rate has no significant effect in the thin 3 and 7 Tl HD targets.

Shown in Fig. 4.34 are the SMC results compared to the data for the 300 Tl HD when a nonresonant rate of $\lambda^{NR}_{dt\mu-p}$=0.56 μs^{-1} is included along with the resonant molecular formation rate, $\lambda_{dt\mu-p}$, scaled by 0.5 and the scattering cross section, $\sigma_{t\mu+d}$, scaled by 0.9. Shown in (a) is the comparison for the SEMT target upstream and 300 Tl HD downstream.

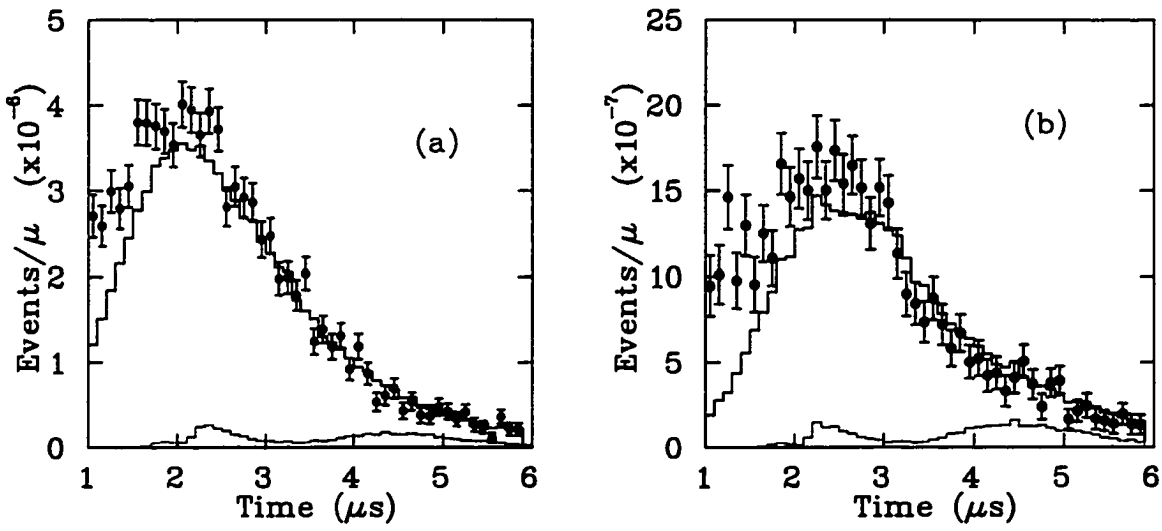

Figure 4.34: *Fusion time distribution compared to SMC results for (a) a SEMT upstream with 300 Tl HD downstream and (b) for a SET ⊕ 14 Tl D_2 target upstream and 300 Tl downstream. For input to SMC $\lambda_{dt\mu-p} \times 0.5$, $\sigma_{t\mu+d} \times 0.9$ was used and the nonresonant molecular formation rate of $\lambda^{NR}_{dt\mu-p}$=0.56 μs^{-1}.*

The values listed in Table 4.12 confirm that χ^2/dof is now reasonable and the ratio of data to simulation is closer to one. Figure (b) is a similar comparison for a 300 T*l* *HD* target which had an upstream moderator layer of 14 T*l* D_2, rather than the nominal 10 T*l* D_2. Because of the thicker moderator layer upstream, less $t\mu$ emission occurs resulting in a lower fusion yield downstream. Again, the fit results are more reasonable, and the fit ratio is close to one.

Because a factor of 0.5 is needed to correctly normalize the molecular formation rates $\lambda_{dt\mu-p}$ for *HD* (discussed in Appendix A), the Monte Carlo was also run with a nonresonant rate half of the published theoretical rate ($\lambda^{NR}_{dt\mu-p}$=0.28 μs^{-1}). The results are given in Table 4.12 for the 300 T*l* *HD* targets. Compared to the simulations in which the nonresonant rate of $\lambda^{NR}_{dt\mu-p}$=0.56 μs^{-1} was used, the quality of the fits is slightly poorer with the scaling factor being closest to one for the conditions of the rate input to SMC being 0.56 μs^{-1}.

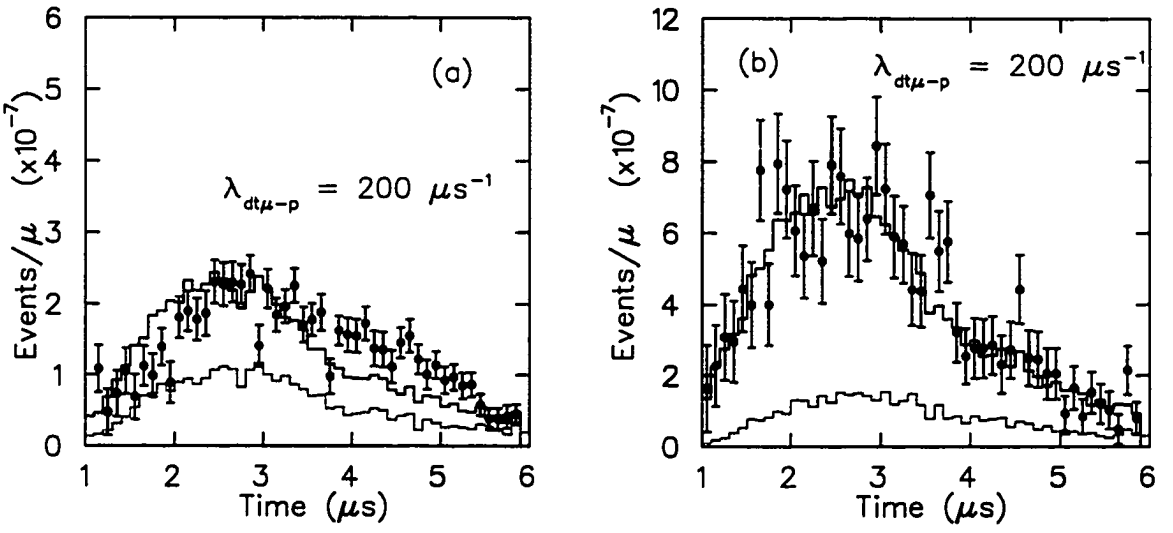

Figure 4.35: *Fusion distribution compared to SMC results for (a) 3 and (b) 7 Tl HD. The input to SMC used only the constant rate of 200 μs^{-1} for molecular formation on HD, no resonant molecular formation was included.*

Molecular formation of $dt\mu$ in HD was simulated using a constant rate of 200 μs^{-1}, the rate at which the simulation and data for the 3 T*l* HD target matched in yield, rather than using the resonant formation files. Shown in Fig. 4.35 are the SMC results compared to the time-of-flight data for the 3 and 7 T*l* HD targets. The simulation reproduces the 7 T*l* data but is not quite right for the thinner target, underestimating the fusion yield for times between 4 and 5.5 μs. To test this constant rate further, simulations of the 300 T*l* HD data are shown in Fig. 4.36. The fusion yield is overestimated, however the shape is clearly similar to the experimental results. The simulation has a peak around 2 μs in agreement with the maximum in the data, however in (b) where there is a thicker D_2 moderator layer upstream, and hence a different energy distribution of $t\mu$ atoms making it into the downstream layer, the agreement is poorer. The simulation reaches a maximum around 2.8 μs whereas the data peaks at around 2.3 μs. Notice that in all the simulations, the shape of the contribution from direct formation to fusion no longer has a two peaked structure as

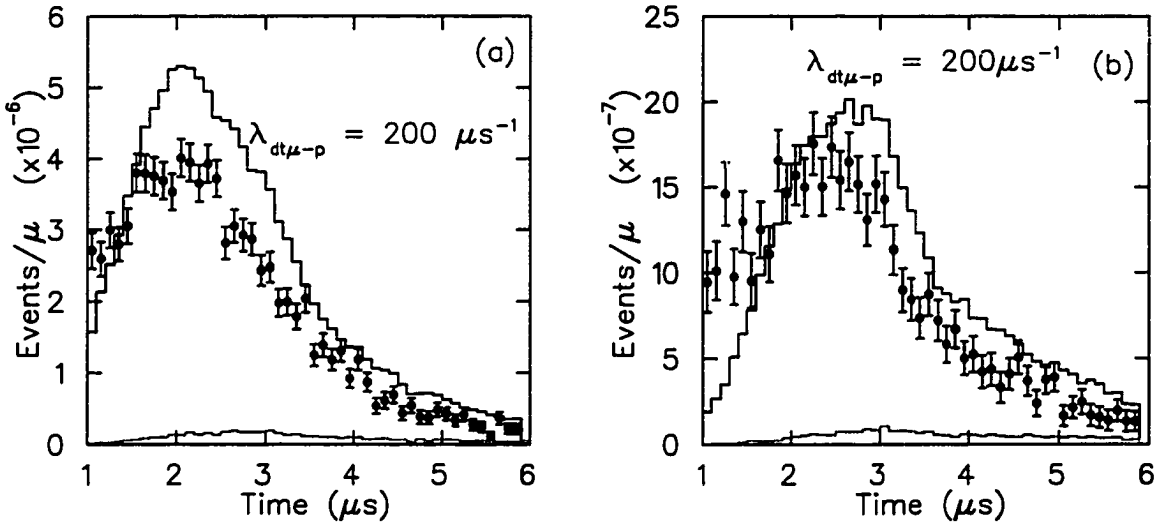

Figure 4.36: *Fusion time distribution compared to SMC results for (a) SEMT upstream and 300 Tl HD downstream and (b) SET ⊕ 14 Tl D_2 target upstream and 300 Tl HD downstream. The input to SMC used only the constant rate of 200 μs^{-1} for molecular formation on HD, no resonant molecular formation was included.*

expected for the energy dependent rates.

The fits of SMC to data are listed in Table 4.12 for the constant molecular formation rate of $\lambda_{dt\mu-p} = 200\ \mu s^{-1}$. For the 3 and 7 T*l* targets this results in a fit ratio very close to one, however for the 300 T*l* targets, the fit ratio is quite different from one. Comparing the χ^2/dof for the 3 T*l* target under the two separate conditions of (i) $\lambda_{dt\mu-p} = 200\ \mu s^{-1}$ and (ii) $\lambda_{dt\mu-p} \times 0.5$, $\sigma_{t\mu+d} \times 0.9$ with the nonresonant rate of $\lambda^{NR}_{dt\mu-p}$=0.56 μs^{-1}, the conditions in (ii) result in a better fit of the scaling factor and both (i) and (ii) produce similar quality fits to the shape of the fusion spectrum. For the 7 T*l* data, the scaling factors produced by (i) and (ii) are similar and close to one, however the fit of method (ii) is better, as is the fit of the shape comparison between the two fusion time spectra. However, when we use the energy independent molecular formation rate in thick targets, the fits are much poorer. The scaling factors favour the conditions in (ii) as does the shape comparison, although the

agreement is clearly not sufficient to show that all details are being simulated correctly.

4.8.1 Uncertainties

The uncertainties associated with selecting cuts on the fusion alpha energy spectrum for the time-of-flight analysis were discussed in section 4.5.1. However, for the 300 Tl HD targets, the determination of the errors associated with the background subtraction is not straightforward and is discussed in this section.

Recall that the background-subtracted energy spectrum for the fusion alpha particles in the 300 Tl targets at low energies was significantly different from that in the thin targets. A background which extends into the low energy region of the alpha peak must be accounted for. Using the SMC Monte Carlo, the location in the 300 Tl HD target at which fusion occurs was simulated and this position along the beam axis is shown in Fig. 4.37 (a) [2]. Figure 4.37 (b) shows the position at which fusion occurs due to direct processes only. The $t\mu$ atoms which lose no energy before molecular formation will of course result in molecular formation very near the surface of the HD target. The GEANT Monte Carlo simulation was then employed to use the information plotted in Fig. 4.37 (a) as an input to calculate the energy loss distribution of the 3.5 MeV alpha particles as they travel through the 300 Tl target and are subsequently detected by the silicon detectors.

To make a direct comparison, the GEANT simulation must be scaled to the data on the number of fusions occurring downstream. The data normalized to GMU can be expressed in terms of the Monte Carlo results by the following:

$$\frac{Data}{GMU} = \frac{GEANT\ \alpha}{\sum GEANT\ input\ events} \cdot \frac{SMC\ fusion}{\sum SMC\ input\ events} \cdot S_F \qquad (4.41)$$

where $\sum$ *input events* is the number of Monte Carlo events (SMC or GEANT) and puts both Monte Carlo results in terms of a single input muon. The GEANT output ($GEANT\ \alpha$)

[2] Zero defines the point at which the $t\mu$ atom enters the HD target.

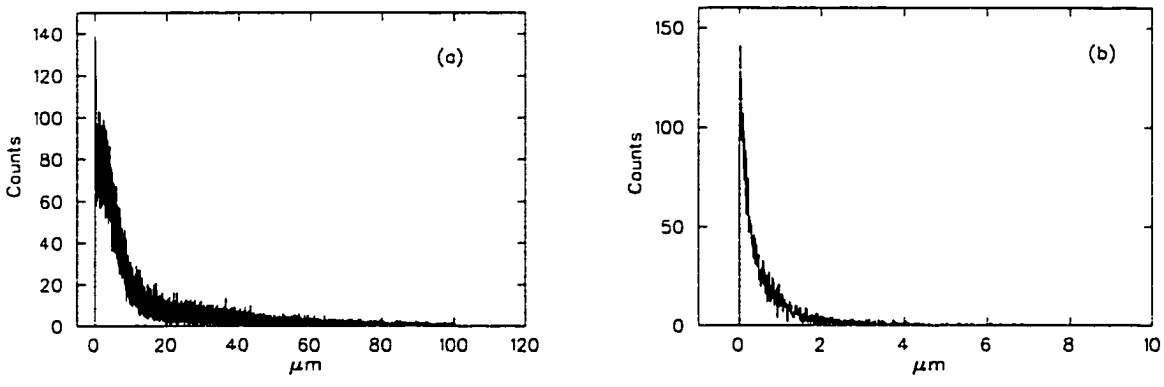

Figure 4.37: *SMC simulations of the position at which fusion occurs in the 300 Tl HD target. Shown in (a) is the position (along the beam axis) of all fusions occurring in the target and in (b) is the position of fusions which are due to direct processes only. Note that the simulations are for a SEMT upstream. The zero position defines the point at the which the $t\mu$ atom enters the HD target.*

needs to be converted into the number of fusions which occur downstream. This is done by using the results of the SMC code (*SMC fusion*) which calculates the number of fusion events which occur downstream. Finally scaling by the stopping fraction, S_F, must be done to account for the fact that not every muon that enters the upstream target (in SMC) stops there and enters the μCF process. The SMC code calculates the number of fusions which occur downstream. The comparison of GEANT results for the two targets (a SEMT upstream and 300 T*l* *HD* downstream and a SET $\oplus$ 14 T*l* D_2 upstream and 300 T*l* *HD* downstream) shown in Fig. 4.38 gives a measure of how well SMC is reproducing our data. (Note that some backgrounds are not included, but will be considered in the following pages.) The GEANT alpha energy distribution is shown as a smooth curve while the data are plotted as solid dots. The dashed lines show the energy cuts selected for the time-of-flight analysis.

The GEANT simulation includes the acceptance of the silicon detectors which have an

assumed efficiency of 1.00. Thus, the fraction of alpha particles in the simulation which exit the 300 Tl HD layer and enter the silicon detectors is given by the ratio $\frac{GEANT\ \alpha}{\sum input\ events}$ in Eq. (4.41) and should equal the silicon detector acceptance. This ratio for the SEMT upstream and 300 Tl HD downstream is 0.0353 $\pm$ 0.0002 instead of the nominal value Ω_{Si} = 0.0464 $\pm$ 0.0020 for Si1+Si2 quoted in section 4.2.1. For the target consisting of a SET $\oplus$ 14 Tl D_2 upstream and 300 Tl HD downstream, this ratio is 0.0356 $\pm$ 0.0002. Thus, the fusion alpha particles in the thick HD layer undergo a great deal of scattering and energy loss (compared to the thinner targets) and the "effective" solid angle of acceptance for Si1+Si2 is 0.035. For the 3 Tl HD target, a similar GEANT simulation was run and the solid angle was consistent with Ω_{Si} = 0.0464 $\pm$ 0.002 for Si1+Si2 as given in section 4.2.1. It should be noted that these "effective" solid angles are for the energy range of $0 < E < 5000$ keV.

The percentage difference in the number of counts for the scaled GEANT simulation compared to the data for a SEMT upstream and 300 Tl HD downstream is about 38% for the energy cut shown ($1800 < E < 3900$). For this target and energy range, the "effective" solid angle was found to be Ω_{Si} = 0.030 for Si1+Si2, smaller than the previous value of Ω_{Si} = 0.035 due to the narrower energy range. The percentage difference in the number of counts produced by the GEANT simulation compared to the data for a SET $\oplus$ 14 Tl D_2 upstream with 300 Tl HD downstream is about 41% for the energy cut shown ($2000 < E < 3800$). The "effective" solid angle corresponding to this target and energy range was found to be Ω_{Si} = 0.029 for Si1+Si2, again smaller than the previous value due to the narrower energy range. Note that the different energy cuts placed on the different targets were chosen to try to select the portion of the energy spectrum which represented only the alpha particle and minimized events from background.

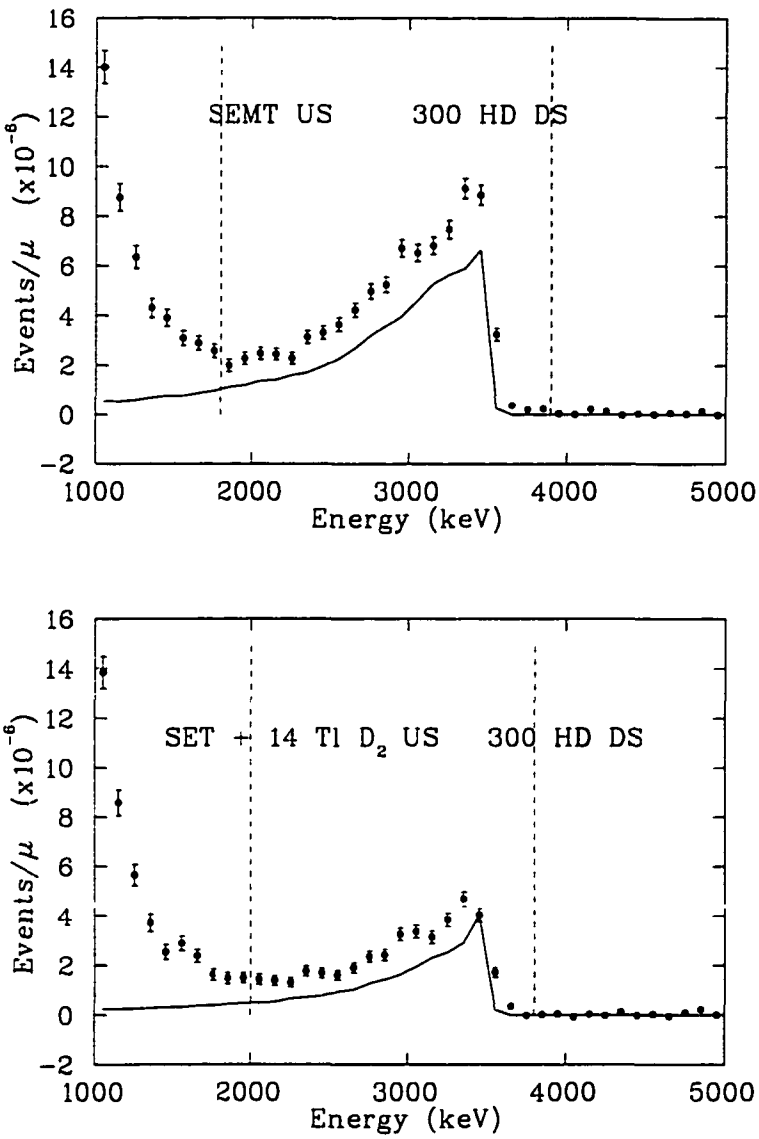

Figure 4.38: *GEANT simulations of the 3.5 MeV alpha particle energy spectrum for the 300 Tl HD targets compared to the data. The simulation results are plotted as curves and the data are plotted as solid dots. The dashed lines show the energy cuts selected for the time-of-flight analysis.*

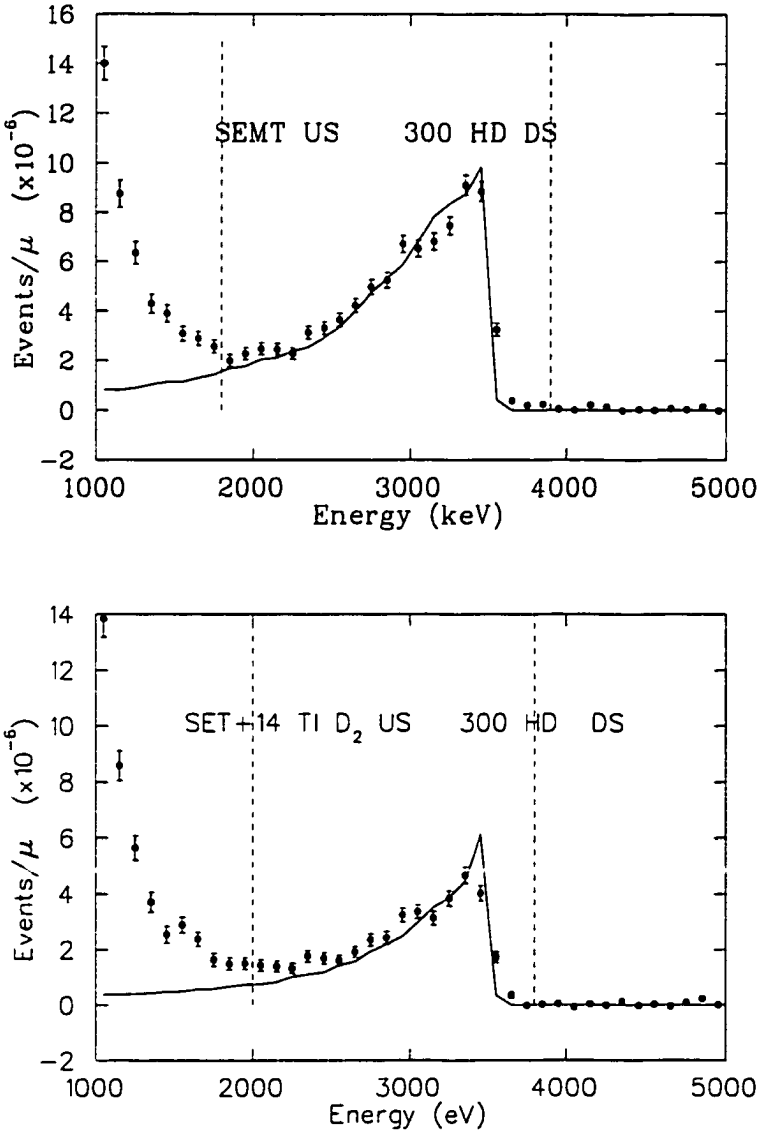

Figure 4.39: *GEANT simulations of the 3.5 MeV alpha particle energy spectrum for the 300 Tl HD targets compared to the data. The simulation results are plotted as curves and were fit to the data (plotted as dots) in the energy range shown by the dashed lines.*

Shown in Fig. 4.39 are the results of a fit ($\chi^2/dof \sim 9$), for the energy ranges defined by the dashed lines ((a) $1800 < E < 3900$ and (b) $2000 < E < 3800$), of GEANT simulation to data, allowing the scaling between the two to be a free parameter.

However, recall that in section 4.5.1 it was observed that the fusion alpha spectra for the thick targets had a small peak which could be due to the 3 MeV proton produced in the following fusion reaction:

$$dd\mu \rightarrow p + t + \mu \ . \tag{4.42}$$

To test this hypothesis, both the SMC and GEANT Monte Carlos were again used. For this type of fusion to be occurring in the downstream HD layer, incoming muons which do not decay or become captured while travelling through the upstream target can travel downstream, enter the HD target and be captured either on a proton or a deuteron. This process was simulated with SMC for muons stopping in the 300 Tl HD target downstream. Based on recent theoretical calculations of negative pion capture in HD gas, 47% of the muons were stopped on protons and 53% on deuterons [81]. All allowed reactions in the muon catalyzed fusion cycle (see Fig. 2.1) then took place with their reaction rates.

There exists little experimental and theoretical information for muon catalyzed fusion reactions in HD. The process of importance which was added to the SMC input files to allow the $dd\mu$ fusion cycle to occur was $d\mu + HD \rightarrow dd\mu$ where the rate of molecular formation from gaseous HD has been taken from Smirenin [46] and the fusion rate has been taken from Knowles [82].

The energy distribution of 3 MeV protons produced in the 300 Tl HD layer which strike the silicon detector has been simulated by GEANT and is shown in Fig. 4.40. The simulation was done for 10^5 protons generated with a uniform spatial distribution in the beam direction (Z) and with a flat-topped Gaussian to represent the beam profile in the XY plane. To determine the contribution to the spectrum in the silicon detector of this

3 MeV proton from $dd\mu$ fusion in the HD target, another GEANT simulation determined the fraction of the muon beam which stops in the 300 Tl target. This simulation is similar to the one described in section 4.4 and the resulting stopping fraction of muons in the downstream target was found to be 7.65%. To determine how much of a contribution to the fusion spectra this proton can make we must scale the spectrum given in Fig. 4.40 before comparing it to the fusion spectrum. Note that the efficiency of ~3.9% for detecting protons is given by the sum of counts in the GEANT proton spectrum normalized to the number of input protons. It is found that the yield/GMU of protons produced by $dd\mu$ fusion in the 300 Tl layer is $\sim 4.7 \times 10^{-7}$ (for a time window of 1 to 6 μs). Comparing this number with the number of counts in the alpha peak of Fig. 4.38 for a SEMT upstream, we see that this accounts for only $\sim$ 1% of the total fusion yield. It should be noted however that the rate used for $dd\mu$ fusion in HD in one which was measured in gaseous HD and not in the solid state. Thus, it is possible that the $dd\mu$ fusion rate used in SMC is underestimating this process in the solid state.

There are also other processes which can occur when muons enter the downstream HD target and need to be accounted for in SMC. Among these processes are: $p\mu + HD \rightarrow pd\mu$, $d\mu + HD \rightarrow pd\mu$ and $p\mu + HD \rightarrow pp\mu$ with the rates for the first two processes taken from Semenchuk [45] and the last from Mulhauser [79]. The fusion processes which occur due to the formation of $pd\mu$ molecular ions are given by

$$pd\mu \rightarrow {}^3He + \gamma + \mu \tag{4.43}$$

$$pd\mu \rightarrow \mu{}^3He + \gamma \tag{4.44}$$

$$pd\mu \rightarrow {}^3He + \mu \ . \tag{4.45}$$

If a γ is produced in the $pd\mu$ fusion process, the probability of the muon sticking to the helium nucleus is $\sim$ 99% and thus the reaction in Eq. (4.43) can be ignored [83]. If a

γ is not produced in this fusion process then the muon which is released is referred to as a conversion muon, because the atom's energy is converted into the kinetic energy of the muon, rather than emitted as a photon. The energy of this conversion muon is 5.3 MeV, while the energy of the γ is 5.5 MeV.

The energy loss distribution of the 5.3 MeV conversion muons produced in $pd\mu$ fusion and simulated in GEANT is shown in Fig. 4.41. The simulation was performed for 10^6 muons originating in the 300 T*l* target distributed uniformly along Z and with a flat-topped Gaussian in the XY plane. The muons are quite energetic, losing an insignificant amount of energy in the 300 T*l* HD target, and depositing only a small amount of energy in passing through the silicon detectors. The efficiency, given by the sum of counts in the peak divided by the $\sum$ *GEANT input events*, is found to be ~ 0.062. Clearly this is greater than the silicon detector acceptance given in section 4.2.1; this is because the muons are very energetic and can travel through the thin copper collimator shield placed in front of the silicon detectors. Thus, the active surface area of the silicon detectors for these 5.3 MeV muons is larger.

Shown in Fig. 4.42 are the scaled GEANT contributions from the 3 MeV proton and 5.3 MeV muon compared to the experimental fusion peak for the SEMT upstream and 300 T*l* HD target downstream. In figure (a) the proton and muon contributions are plotted separately. Both contributions are negligible past $\sim$ 3 MeV. In figure (b) these contributions are added together and in figure (c) the GEANT contribution of the 3.5 MeV fusion alpha particle is included as well.

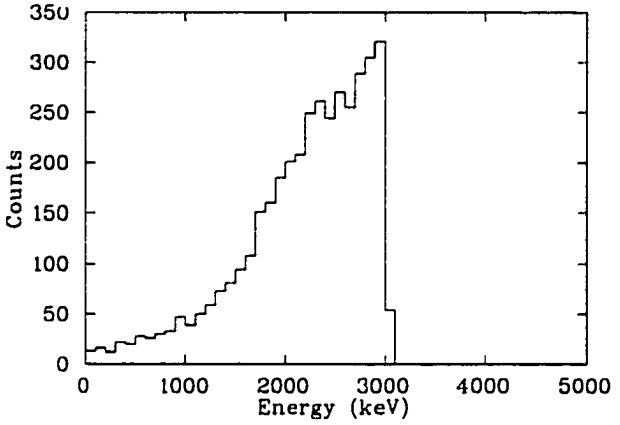

Figure 4.40: *GEANT simulation of the 3 MeV proton energy distribution detected by the silicon detectors. The simulation is for* 10^5 *protons generated with a uniform distribution in the (300 Tl HD) target Z plane and a flat-topped Gaussian in the XY plane (see section 4.3).*

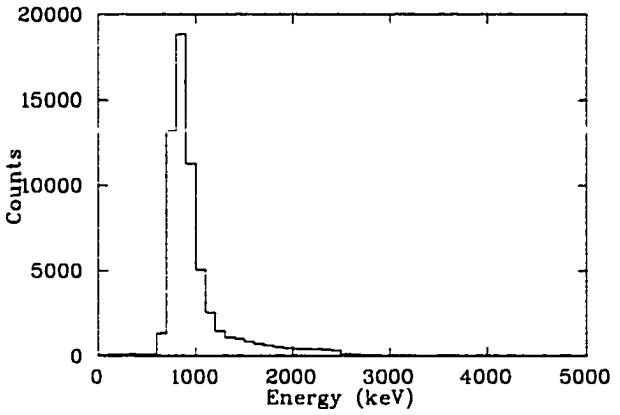

Figure 4.41: *GEANT simulation of the 5.3 MeV muon energy loss distribution. The simulation is for one million 5.3 MeV muons originating in the 300 Tl HD target with their distribution being a flat-topped Gaussian (see section 4.3) with 10 mm flat top radius and 10 mm FWHM in the XY plane and a uniform distribution in the Z plane.*

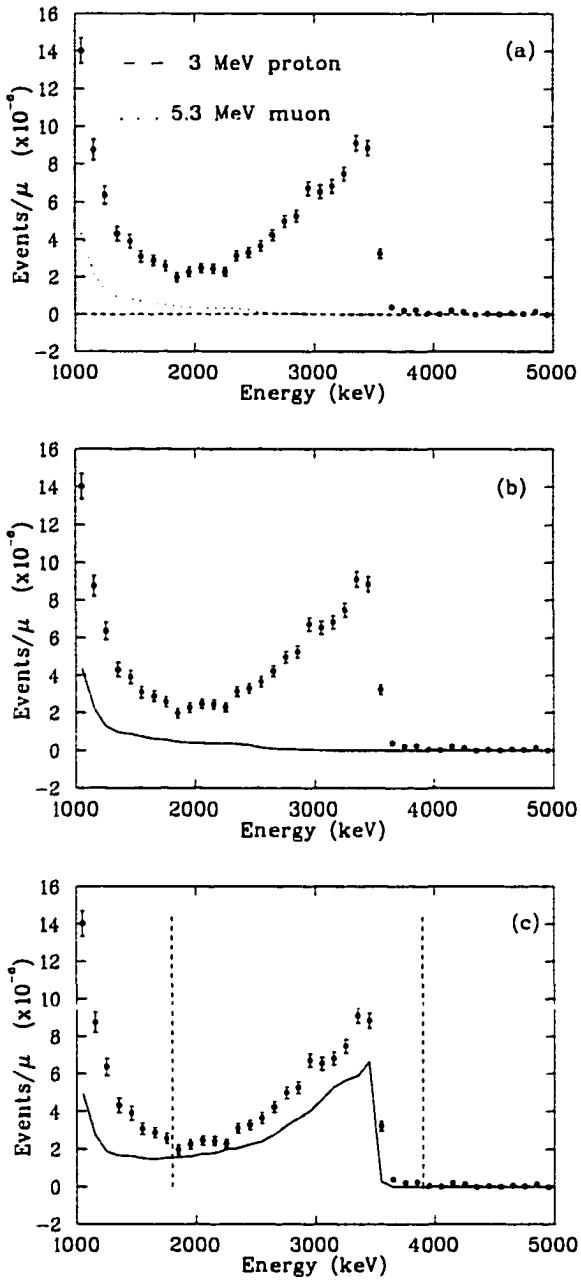

Figure 4.42: *GEANT simulations of the energy spectrum for the SEMT upstream and 300 Tl HD downstream target. In (a) the contributions of the 3 MeV proton spectrum and 5.3 MeV muon spectrum are shown. In (b) these contributions are added together and figure (c) shows the total contribution from the 3.5 MeV alpha particle, 3 MeV proton and 5.3 MeV muon.*

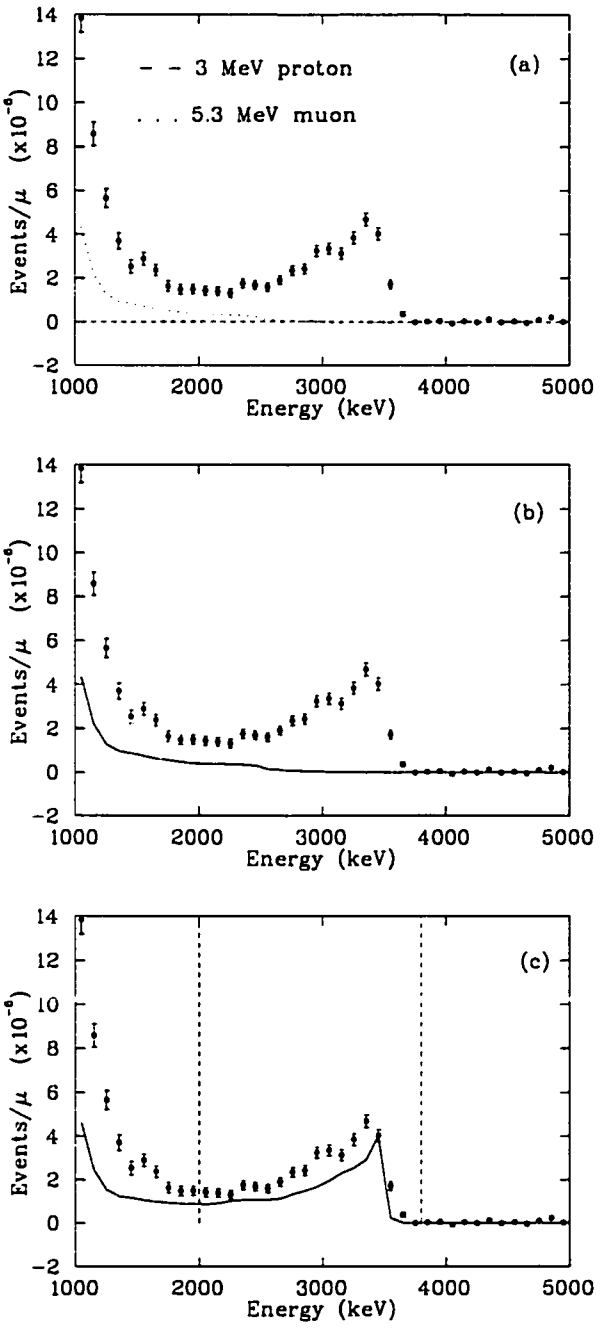

Figure 4.43: *GEANT simulations of the energy spectrum for the SET ⊕ 14 Tl D_2 upstream and 300 Tl HD downstream. In (a) the contributions of the 3 MeV proton and 5.3 MeV muon are shown. In (b) these contributions have been added together and figure (c) shows the total contribution from the 3.5 MeV alpha particle, 3 MeV proton and 5.3 MeV muon.*

Similarly we show in Fig. 4.43 the scaled GEANT results for the proton and muon contributions compared to the experimental fusion alpha peak for the SET $\oplus$ 14 Tl D_2 upstream and 300 Tl HD downstream. Again, figure (a) shows the proton and muon contributions plotted separately and (b) shows them added together. In figure (c) the GEANT contribution of the fusion alpha peak has been added. The trend is the same as in the previous result.

To account for the background seen at $\sim$ 1000 keV, a GEANT simulation of the silicon detector energy spectrum for muon decay electrons in the 300 Tl HD target was performed and the results are shown in Fig. 4.44 (a), scaled as previously discussed. The source of background which appears in all targets at low energies indeed appears to be due to electrons produced in muon decay. This is also evident in the time spectra for this energy region, which shows an exponential dependence with a lifetime of $\sim$ 2 μs. The "effective" solid angle from GEANT for muon decay electrons was found to be 0.113— larger than the nominal value of $\Omega_{Si} = 0.046$. This is approximately twice as large as the value $\Omega_{Si} = 0.062$ determined for conversion muons. Although it is possible that the decay electrons are traversing not only the copper mask but also a copper support plate in front of the silicon detectors, a comparison with the data indicates this contribution is too high. By comparing the GEANT results to the data in Fig. 4.44 (a), (between $1000 < E < 2000$) we can clearly see that the simulation is overestimating this contribution. Because of an energy threshold cut off in the electronics, only the tail of the muon decay electron spectrum appears. Note that the efficiency of the silicon detectors under 2 MeV is not 100% as seen in Fig. 4.1 from the intensity of the pulser peaks decreasing under 2 MeV. To avoid the problem of overestimating this contribution, the GEANT results have been fit to the decay electron tail in the data, making sure that at high energies (4 to 5 keV) this contribution is consistent with zero. The results are given in Fig. 4.44 (b) with the conversion muons being plotted as

well. Fig. 4.44 (c) depicts the sum of the GEANT contributions from the decay electrons, conversion muons and fusion alphas.

The result of including contributions from the conversion muons, decay electrons and protons to the time-of-flight simulated fusion time spectra are given in Fig. 4.45 and Fig. 4.46 for the targets consisting of (a) SEMT US and 300 T*l* HD DS and (b) SET $\oplus$ 14 T*l* D_2 US and 300 T*l* HD DS. The "effective" solid angle for each simulated process has been included. The proton, muon and decay electron contributions have been plotted separately and the sum of all contributions (fusion alphas + protons + decay electrons + conversion muons) is shown as the dark line histogram which is to be compared to the data plotted as solid dots. Note that the "effective" solid angle for the fusion alpha contribution is $\Omega_{Si} = 0.030$, which has the effect of lowering the SMC alpha contribution results, compared to the results shown in the previous section in which the nominal solid angle of $\Omega_{Si} = 0.046$ was used in scaling the SMC results.

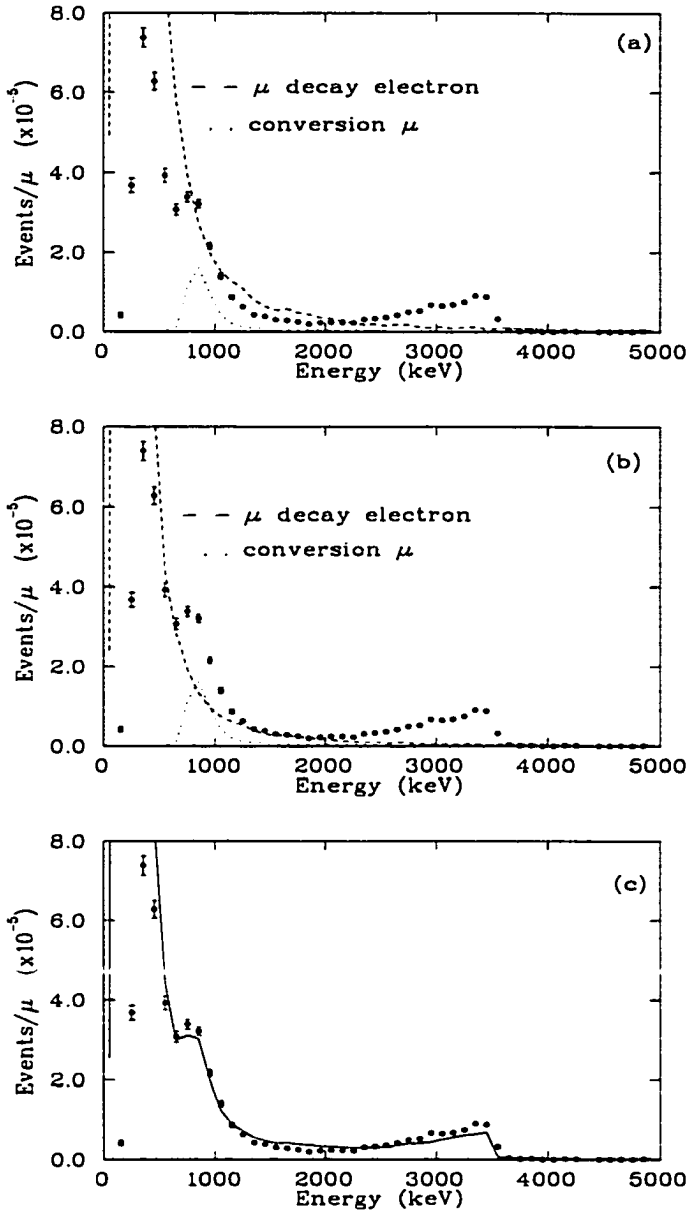

Figure 4.44: *The energy spectrum for the SEMT upstream and 300 Tl HD downstream target is shown. Figure (a) shows the muon decay electron peak simulated by GEANT and scaled to the data. Figure (b) shows the GEANT electrons fit to the data. In figure (c) the contribution from decay electrons and conversion muons has been added together for comparison with the data.*

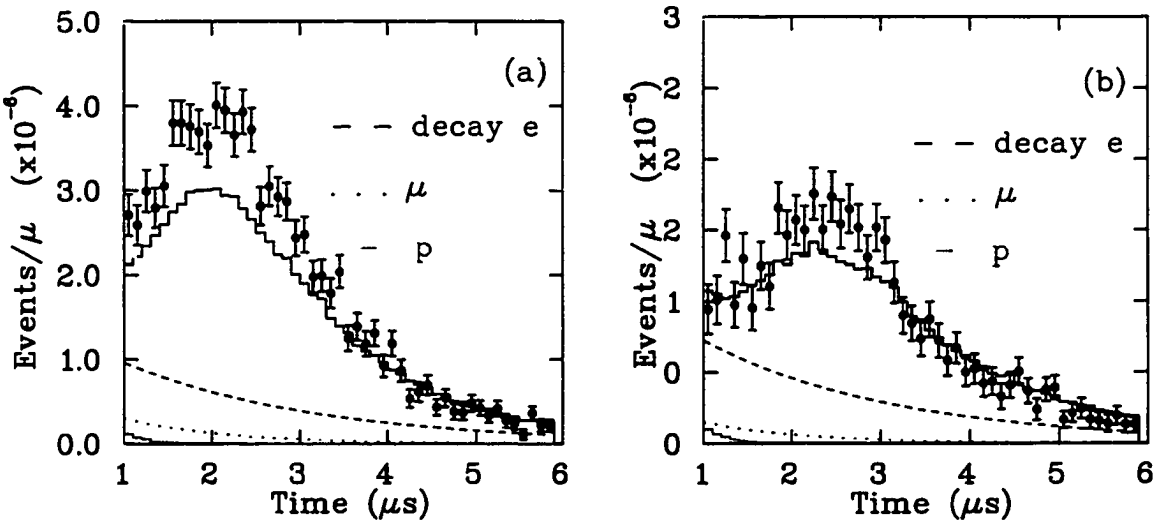

Figure 4.45: *Time-of-flight comparison for (a) the SEMT and (b) the SET ⊕ 14 Tl D_2 US and 300 Tl HD DS targets. The total SMC contribution (3.5 MeV alpha particles + 3 MeV protons + 5.3 MeV conversion muons + decay electrons) is shown by the dark histogram line. The input to SMC used the factors of $\lambda_{dt\mu-p} \times 0.5$, $\sigma_{t\mu+d} \times 0.9$ and + $\lambda^{NR}_{dt\mu-p}$=0.56 μs^{-1}.*

For Fig. 4.45 the changes made in the input to SMC were $\lambda_{dt\mu-p} \times 0.5$, $\sigma_{t\mu+d} \times 0.9$ and the constant rate of $\lambda^{NR}_{dt\mu-p} = 0.56\ \mu s^{-1}$ was included. In Fig. 4.46 the changes made in the input to SMC were that the molecular formation on HD was set to a constant rate of $\lambda_{dt\mu-p} = 200\ \mu s^{-1}$ and the theoretical molecular formation rate files for HD were not used. For the SEMT upstream and 300 T*l* HD target, the proton contribution to the fusion data yield for a time window of 1 to 6 μs is $\sim$ 1%, the conversion muon contribution is $\sim$ 4% and the decay electron contribution is $\sim$ 19%. Thus, the thick HD data has a significant background contribution from other processes occurring for the energy cut chosen. Comparing Fig. 4.45 to Fig. 4.34 and Fig. 4.46 to Fig. 4.36 we see that including these above mentioned backgrounds reduces the shape discrepancy between data and simulation, especially in the early time range of 1 to 2 μs (note: the differences in intensity between the figures is due to

the "effective" solid angle versus the nominal solid angle used in the normalization of SMC to data).

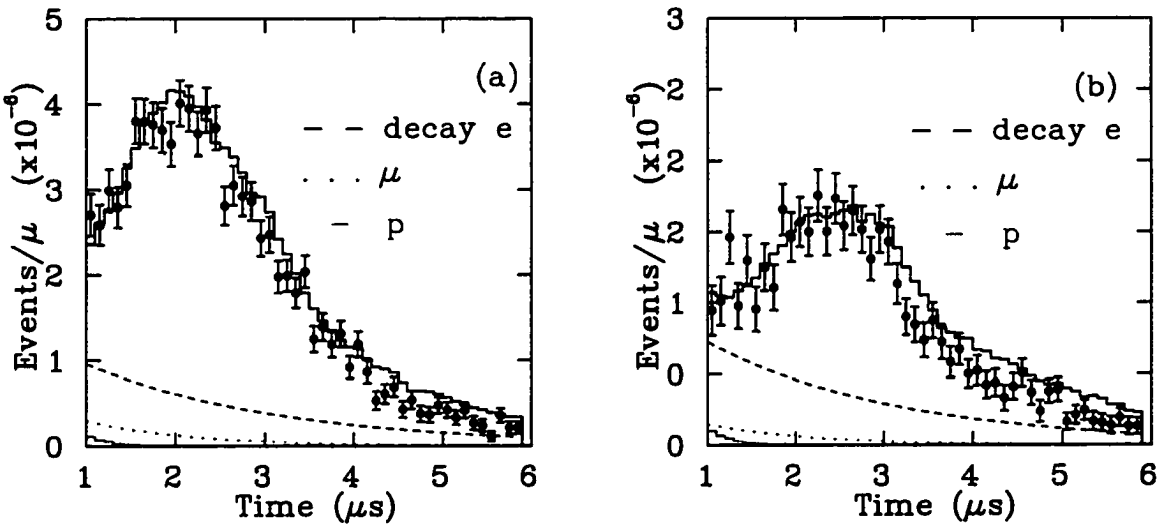

Figure 4.46: *Time-of-flight comparison for (a) the SEMT and (b) the SET ⊕ 14 Tl D_2 US and 300 Tl HD DS targets. The total SMC contribution (3.5 MeV alphas + 5.3 MeV muons + decay electrons + 3 MeV protons) is shown by the dark histogram line. The input to SMC used a constant rate of* $\lambda_{dt\mu-p} = 200\ \mu s^{-1}$.

The final results of the data analysis are presented in Chapter 5, with the systematic uncertainties included. Results of fitting SMC to the data for the four HD targets will be presented.

Chapter 5

Results, Discussion and Conclusions

The data and analysis presented in this thesis have posed many new questions as well as answered others. The results including all uncertainties will be summarized. Proposals for future experiments to verify these results will be presented.

To determine the best value of the $\lambda_{dt\mu-p}$ scaling factor, simulations were done in which this scaling factor was varied from the nominal value of 0.5 to values between 0.25 and 0.7. The input into the SMC simulations used the pertinent cross section tables and rates discussed in section 4.6 of the thesis with the following modifications, (i) the $\sigma_{t\mu+d}$ scattering cross section was multiplied by the factor of 0.9, and (ii) the nonresonant rate of $\lambda^{NR}_{dt\mu-p}$=0.56 μs^{-1} was included. The results of the simulations were then fit to the HD fusion data. The sensitivity to the HD molecular formation resonances is highest in the thin targets where a significant amount of molecular formation occurs due to direct processes. Thus, the targets used for this analysis were the 3 and 7 Tl HD targets. The χ^2 values of these fits were then plotted versus $\lambda_{dt\mu-p}$ scaling factor. The minimum in χ^2 was then

DS Target	$\Omega_{Si} \cdot S_F$	$\lambda_{dt\mu-p}$ scaling factor
3 T*l* *HD*	0.00742	0.399 ± 0.030
3 T*l* *HD*	0.00799	0.342 ± 0.032
3 T*l* *HD*	0.00686	0.450 ± 0.029
7 T*l* *HD*	0.00742	0.520 ± 0.036
7 T*l* *HD*	0.00799	0.473 ± 0.036
7 T*l* *HD*	0.00686	0.563 ± 0.036

Table 5.1: $\lambda_{dt\mu-p}$ *scaling factors determined from the minimum* χ^2 *fits of fusion data to SMC simulations.*

found by fitting a parabola to the values of χ^2 versus scaling factor. Listed in Table 5.1 are the values of the scaling factor when χ^2 is a minimum for the two HD targets. The error on the minimum value represents the range in scaling factor which results in a change of χ^2 by one. To include errors associated with scaling the SMC results to the data, this same procedure was followed for the minimum and maximum values of the normalization $\Omega_{Si} \cdot S_F$, where the errors on S_F and Ω_{Si} have been added in quadrature to determine the error on the product $\Omega_{Si} \cdot S_F$=(7.42 ± 0.56) × 10^{-3}. The results of these fits are given in Table 5.1. Shown in Fig. 5.1 are plots of χ^2 versus the $\lambda_{dt\mu-p}$ scaling factor for the 7 T*l* data. Figure (a) shows the fit for the nominal values of stopping fraction and solid angle (S_F=0.32 ± 0.02 and Ω_{Si}=0.0232 ± 0.0010), while (b) and (c) show the fits for the upper and lower limits of $\Omega_{Si} \cdot S_F$.

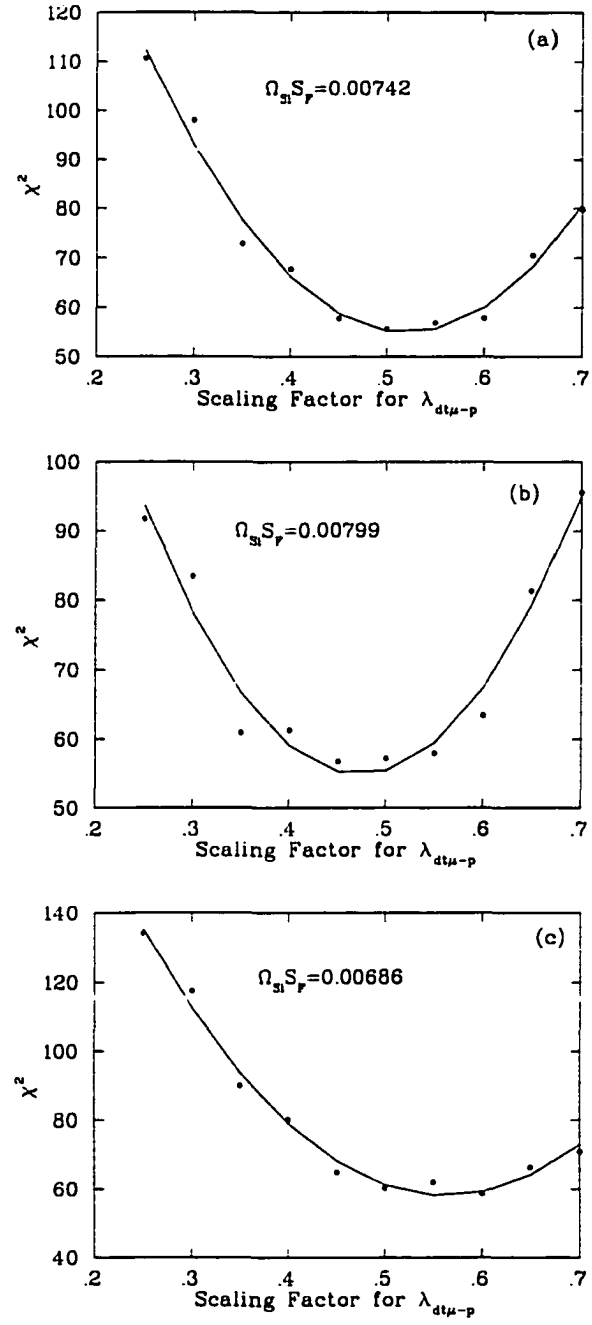

Figure 5.1: *Results of fitting the χ^2 versus $\lambda_{dt\mu-p}$ scaling factor for the 7 Tl HD data. The solid dots represent the χ^2 value for the fit of SMC simulation to data. The line is a fit of a parabola to the dots. The difference between the three graphs is in the solid angle and stopping fraction used to normalize the simulations to the data.*

The $\lambda_{dt\mu-p}$ scaling factors which best represent the data correspond to a minimum in χ^2 for the nominal S_F=0.32 $\pm$ 0.02 and $\Omega_{S:}$=0.0232 $\pm$ 0.010. The errors on the stopping fraction and solid angle, along with other significant systematic errors in the experiment, are common to both the 3 and 7 T*l* *HD* data and thus will not be used in the comparison of $\lambda_{dt\mu-p}$ scaling factors. It is clear that the two values, 0.399 $\pm$ 0.030 and 0.520 $\pm$ 0.036, are not in agreement within their quoted errors. This points to a source of unknown systematic uncertainty. The difference between these two scaling factors is 0.121 $\pm$ 0.047. A systematic uncertainty of unknown origin ($u - sys$) has been assessed to account for this difference using the method discussed in [84]. This error is such that, when added in quadrature to the statistical errors on the scaling factors, it produces a difference in the 3 and 7 T*l* $\lambda_{dt\mu-p}$ scaling factors of one sigma. These values are listed in Table 5.2 along with the weighted average of the results for the two targets. The errors included in the averaging were only the statistical errors, thus the statistical error on the weighted average reflects this. The determined value of $\lambda_{dt\mu-p}$ scaling factor for the 3 and 7 T*l* *HD* targets is 0.449 $\pm$ $(0.023)_{stat}$ $\pm$ $(0.079)_{u-sys}$.

DS Target	$\lambda_{dt\mu-p}$ scaling factor
3 T*l* *HD*	0.399 $\pm$ $(0.030)_{stat}$ $\pm$ $(0.079)_{u-sys}$
7 T*l* *HD*	0.520 $\pm$ $(0.036)_{stat}$ $\pm$ $(0.079)_{u-sys}$
Average	0.449 $\pm$ $(0.023)_{stat}$ $\pm$ $(0.079)_{u-sys}$

Table 5.2: *Listed are the determined values for the $\lambda_{dt\mu-p}$ scaling factor with their statistical errors and the unknown uncorrelated systematic error added to account for the difference in scaling factor between the 3, and 7 Tl HD targets.*

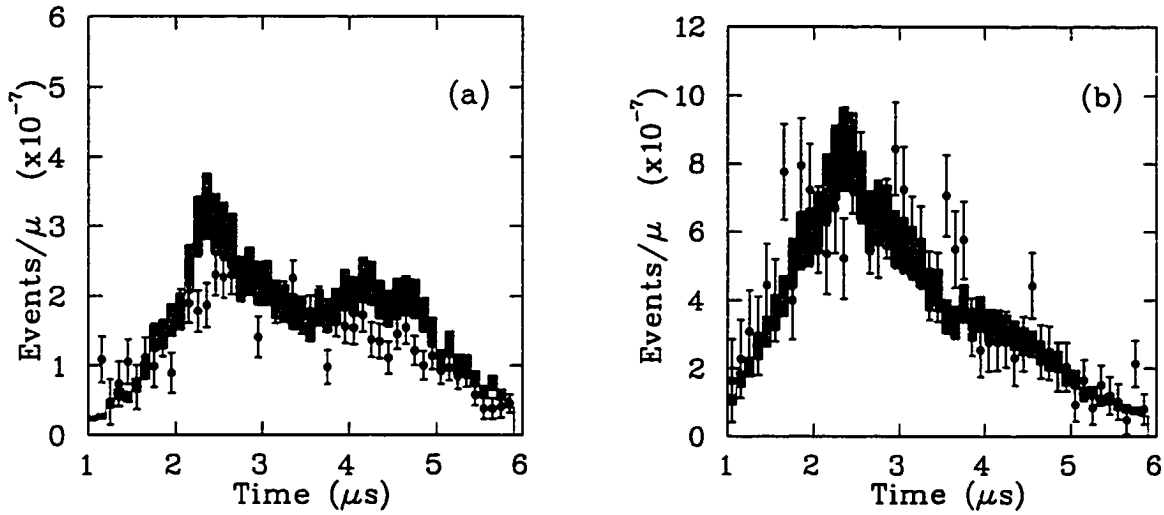

Figure 5.2: *Time-of-flight comparison for (a) 3 and (b) 7 Tl HD. The data are plotted as solid dots with statistical error bars. The SMC results (histogram) are for an input of* $\lambda_{dt\mu-p} \times 0.5$, $\sigma_{t\mu+d} \times 0.9$ *with the nonresonant rate of* $\lambda^{NR}_{dt\mu-p} = 0.56\ \mu s^{-1}$ *included.*

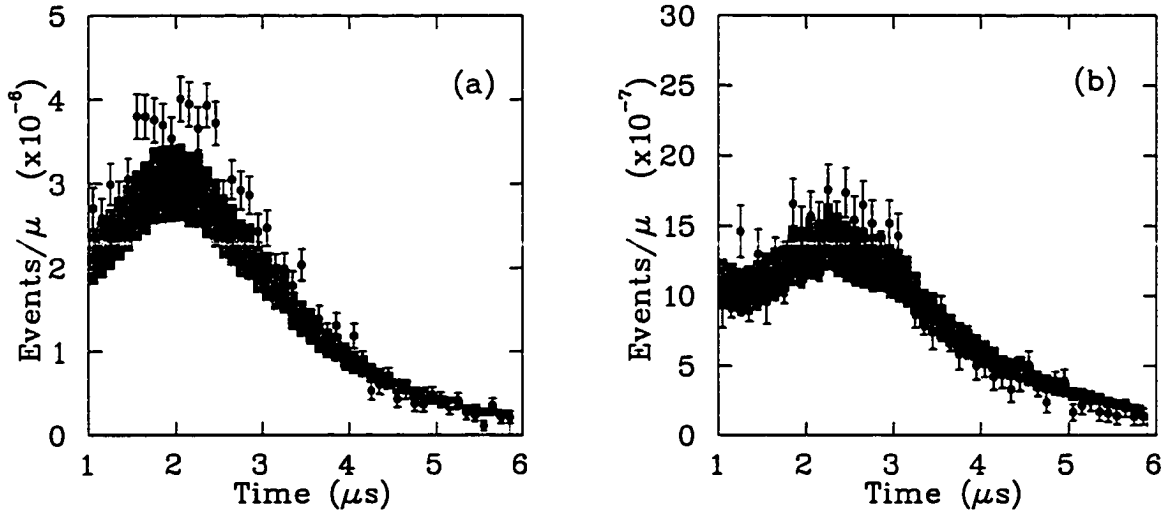

Figure 5.3: *Time-of-flight comparison for the 300 Tl HD targets with (a) SEMT US and (b) SET* $\oplus$ *14 Tl* D_2 *US. The data are plotted as solid dots with statistical error bars. The SMC results (histogram) are for an input of* $\lambda_{dt\mu-p} \times 0.5$, $\sigma_{t\mu+d} \times 0.9$ *with* $\lambda^{NR}_{dt\mu-p} = 0.56\ \mu s^{-1}$ *included. Contributions from decay electrons, conversion muons and 3 MeV fusion protons have been included.*

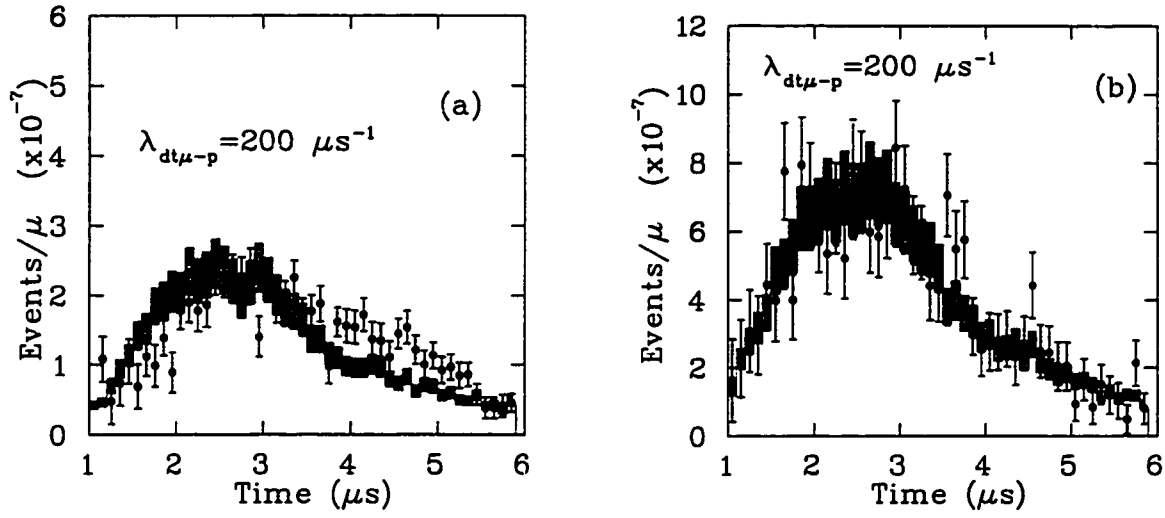

Figure 5.4: *Time-of-flight spectra for (a) the 3 and (b) 7 Tl HD targets. The data are plotted as solid dots with statistical error bars. The SMC results (histogram) are for an input of the constant rate* $\lambda_{dt\mu-p} = 200\ \mu s^{-1}$.

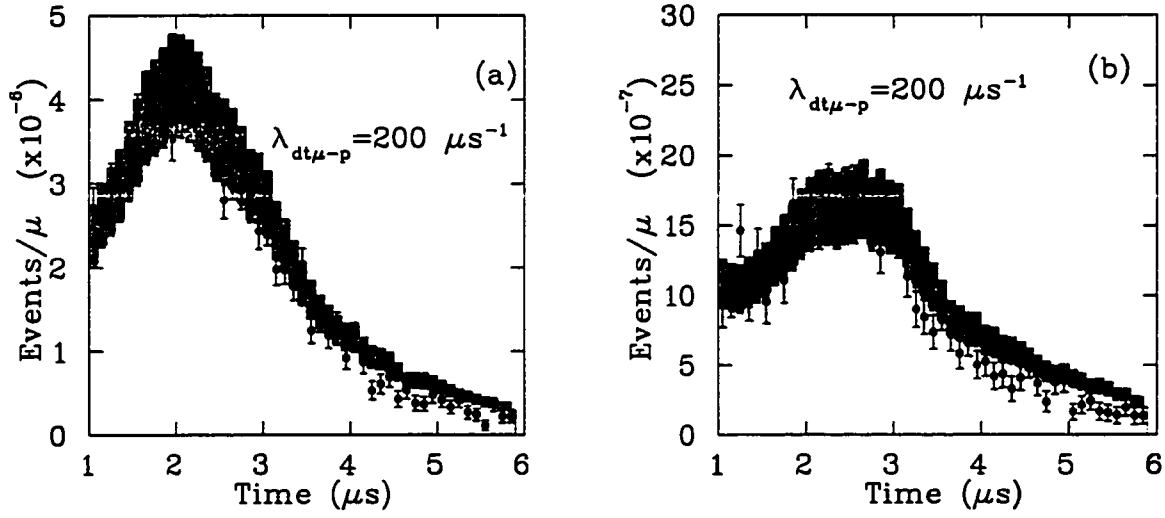

Figure 5.5: *Time-of-flight comparison for the 300 Tl HD targets with (a) SEMT US and (b) SET* $\oplus$ *14 Tl* D_2 *US. The data are plotted as solid dots with statistical error bars. The SMC results (histogram) are for an input of* $\lambda_{dt\mu-p} = 200\ \mu s^{-1}$. *Contributions from decay electrons, conversion muons and 3 MeV fusion protons have been included.*

All the systematic errors in the experiment will now be discussed and summarized, along with the "best" parameters used in the SMC. The data will be compared to these "best" SMC simulations, with the inclusion of all errors, statistical and systematic.

The two sources of error which were not immediately straightforward to determine are the difference in yield between Si1 and Si2 and the dependence of how a change in the thickness of the target scales with varying the $\lambda_{dt\mu-p}$ scaling factor. For the first error, if the difference in yield between Si1 and Si2 was more than two sigma, an appropriate scaled error was taken as half the difference between the two discrepant values [84], the same procedure followed above to determine the unknown systematic uncertainty $u - sys$. To determine the effect of a target thickness error, the ratio of the fractional change in $\lambda_{dt\mu-p}$ scaling factor between the 3 and 7 Tl targets to the fractional change in SMC fusion yield between the 3 and 7 Tl targets was found to 34%. As this dependence is not one to one, 34% of the total error on the determined thickness of the targets (3.65 ± 0.25 μg·cm^{-2}(Tl)$^{-1}$) was used, corresponding to an error of 0.010 (2.3%) on the average scaling factor.

The results of the SMC simulations for the four different target conditions involving HD are shown in Figs. 5.2, 5.3, 5.4 and 5.5. Two separate SMC results have been shown for each of the 3, 7 and 300 Tl HD targets (for both SEMT US and SET $\oplus$ 14 Tl D_2 US). The simulation results shown in Fig. 5.2 and Fig. 5.3 are for the SMC input of $\lambda_{dt\mu-p} \times 0.5$, $\sigma_{t\mu+d} \times 0.9$, plus the nonresonant rate of $\lambda^{NR}_{dt\mu-p} = 0.56$ μs^{-1}. These input parameters were found to best represent all the HD data and will be referred to as the "best theoretical parameters". The SMC results shown in Fig. 5.4 and Fig. 5.5 are for the energy-independent rate of $\lambda_{dt\mu-p} = 200$ μs^{-1}.

The error bars on the data represent the statistical errors and background subtraction while all the other normalization and efficiency errors have been added in quadrature and included as a band on the SMC results. For the normalization and efficiency errors, five

Source of Error	Absolute Uncertainty	Percentage Uncertainty
S_F	0.028	6.2%
Ω_{Si}	0.019	4.3%
energy cut on alpha peak	0.036	8.0%
Si1/Si2 yield difference	0.035	7.8%
target thickness	0.010 or 0.030*	2.3% or 6.8%*

Table 5.3: *Listed are the sources of error for the 7 Tl HD data. The absolute uncertainties are uncertainties in the average $\lambda_{dt\mu-p}$ scaling factor of 0.449. These values are added in quadrature to determine the systematic error on the time-of-flight data. The * depicts the total error on target thickness and was used in the quadratic sum for the comparisons given in Figs. 5.2, 5.3, 5.4 and 5.5.*

terms were considered: (i) the systematic error on the muon stopping fraction which was included since S_F is used to normalize the SMC results; (ii) the error in the solid angle of the silicon detectors also used to normalize the SMC results; (iii) errors associated with choice of energy cut on the fusion alpha peak, the dominant error, ranging from 8 to 10%, depending on the downstream target; (iv) an error resulting from the observed higher yield of Si2 over Si1; and (v) the error on the target thickness. These are summarized in Table 5.3 for the 7 Tl *HD* data.

These uncertainties in solid angle, stopping fraction, energy cut Si1/Si2 difference and target thickness(*) were added in quadrature to produce an error of $\pm$ 0.067 (15%) for the 3, 7 and 300 Tl *HD* targets. The target with SET $\oplus$ 14 Tl D_2 US and 300 Tl *HD* DS has a total uncertainty of $\pm$ 0.076 (17%). All Monte Carlo simulations used a sufficiently large number of input events so that this statistical error is negligible.

Target	$\lambda_{dt\mu-p}$ scaling factor
3 T*l* HD	$0.399 \pm (0.030)_{stat} \pm (0.079)_{u-sys} \pm (0.055)_{sys}$
7 T*l* HD	$0.520 \pm (0.036)_{stat} \pm (0.079)_{u-sys} \pm (0.074)_{sys}$

Table 5.4: *The values of $\lambda_{dt\mu-p}$ scaling factors with all sources of error included.*

The systematic uncertainty on the $\lambda_{dt\mu-p}$ scaling factors have been calculated from adding the last three errors listed in Table 5.3 in quadrature with one other error. This error comes from the results of determining the minimum χ^2 versus scaling factor for the variations in the product $\Omega_{Si} \cdot S_F$. This is the average of the errors on the change in minimum χ^2 by varying the product $\Omega_{Si} \cdot S_F$ to its upper and lower limits (*i.e.* $\Omega_{Si} \cdot S_F$=0.00799 and $\Omega_{Si} \cdot S_F$=0.00686). The $\lambda_{dt\mu-p}$ scaling factors for the 3 and 7 T*l* HD targets are summarized in Table 5.4.

The $\sigma_{t\mu+d}$ scaling factor is estimated to be 0.9 $\pm$ 0.05 based on results presented in section 4.7, along with SMC simulations in which the $\sigma_{t\mu+d}$ scaling factor was varied. Estimating the error from the use of a nonresonant $\lambda^{NR}_{dt\mu-p}$ rate of 0.56 μs^{-1} is not straightforward. Recall that this rate significantly effects only the 300 T*l* HD data and has been included to account for the large difference observed between SMC and data in these targets. The theory includes nonresonant rates in the files which describe molecular formation on HD, however, as discussed in Section 4.8, these nonresonant rates are for gaseous HD. The theorists state there is room for improvement in the calculations of the nonresonant rate by including higher order terms in the calculation and quote at least a 5-10% uncertainty [23]. The normalization factor of Appendix A states we should be using a rate of $\lambda^{NR}_{dt\mu-p} = 0.28\ \mu s^{-1}$, half of the above rate (0.56 μs^{-1}). However, the fit results of SMC to data favour the higher rate. Thus, a 50% error on this rate is well within reason, (*i.e.*

$\lambda^{NR}_{dt\mu-p} = 0.56 \pm 0.28\ \mu s^{-1}$).

The 3 Tl HD target is most sensitive to the molecular formation resonances. Using a constant rate of $\lambda_{dt\mu-p}$ does give good agreement in absolute yield between SMC and 3 Tl HD data as well as a fair fit in the shape. However, the χ^2/dof using the theoretical molecular formation files ("best theoretical parameters") is equally good (see Table 4.12). The absolute yield however is $\sim$ 15% higher than the data. Using the constant rate underestimates the fusion yield between 4 to 5 μs and overestimates the yield between 1.5 to 2 μs. Using the "best theoretical parameters" in the SMC input shows directly the effect of the resonance structure in the molecular formation rates by the appearance of a simulated two-peaked structure in the time-of-flight. The data clearly does not show this two-peaked structure. One possible explanation is that the theoretically calculated molecular formation resonances have not been doppler broadened enough to account for the molecular formation occurring in a solid. Remember that the theory does not take into account any effects of the crystal lattice or its motion with respect to the $t\mu$ atoms. This SMC is also overestimating the yield between 2–3 and 4–5 μs, however the χ^2/dof in fitting the absolute yield favours the "best theoretical parameters" as does the data.

For the 7 Tl HD data, both SMC simulations produce similar results and χ^2/dof for the fits of both intensity and shape. The 300 Tl HD data is very insensitive to the resonances because the majority of fusion occurs due to molecular formation from indirect processes. The constant rate of $\lambda_{dt\mu-p}$ results in a simulated fusion yield which is higher than the data. The fits tend to favour the use of theoretical calculations to match the data yield. Fitting the shape does not distinguish between the two SMC results.

The results of this experiment are in resonable agreement with the theoretical calculations for the resonant molecular formation rates which describe the process $t\mu + HD \rightarrow [(dt\mu)pee]$. The sensitivity of the data to the resonances is largest in thin HD targets in

which a substantial amount of molecular formation occurs from $t\mu$ atoms which do not undergo any energy loss before forming $dt\mu$ molecular ions. However, only one very thin target was deposited. Future experiments that concentrate on measuring $dt\mu$ fusion in solid HD would greatly benefit from using more targets of various thicknesses in which the majority of fusion occurs from direct formation processes. These data would serve to answer questions as to the strength of the resonances, which seem to create a definite two-peaked structure in the simulations which is not reproduced in the present data.

Future experiments would also benefit from studying $dt\mu$ molecular formation in solid HD targets that were thick enough so that the energy at which molecular formation takes place is around $\sim$ 0.003 eV. At these energies, the resonant formation rate is small and the nonresonant formation rate becomes important. This would serve to verify that either the rates included at low energies are too small or that the way the averaging over molecular motion is performed in the calculation is not applicable for the solid state.

Indeed there are yet many questions that could be answered by more experiments on muon catalyzed fusion in solid HD, which would verify the results presented herein.

Bibliography

[1] J.K Bhasin and R.N. Srivastava, Proceedings of the National Seminar on Electrical Energy and Environment, Indian National Academy of Engineering, New Delhi, pp. II-1, 1989.

[2] R. Con *et al.*, Nuclear Fusion **30**, 1924 (1990).

[3] H. Cember, Introduction to Health Physics, Permagon Press, New York, 1983.

[4] P.C. Souers, Hydrogen Properties for Fusion Energy, University of California Press, Berkeley, 1986.

[5] L.I. Ponomarev, Contemporary Physics **31**, pp. 219-245, 1990.

[6] A.A. Harms, Principles of Nuclear Science and Engineering, Research Studies Press Ltd., England, 1987.

[7] H. Muirhead, The Physics of Elementary Particles, Pergamon Press, Oxford, 1965.

[8] S.H. Neddermeyer and C.D. Anderson, Physical Review **51**, 884 (1937).

[9] J.C. Street and E.C. Stevenson, Physical Review **52**, 1002 (1937).

[10] D.H. Perkins, Introduction to High Energy Physics, Addison-Wesley Publishing Company, Inc., Menlo Park, California, 1987.

[11] E. Segre, Nuclei and Particles, The Benjamin/Cummings Publishing Company, Inc., Don Mills, Ontario, 1977.

[12] J.S. Cohen, Physical Review A **27**, 167 (1983).

[13] E.C. Ashenauer and V.E. Markushin, Hyperfine Interactions **101-102**, 97 (1996).

[14] J.S. Cohen, Review of Fundamental Processes and Applications of Atoms and Ions, World Scientific, Singapore, 1993.

[15] W.H. Breunlich *et al.*, Annual Review of Nuclear and Particle Science **39**, 311 (1989).

[16] V.I. Korobov *et al.*, Muon Catalyzed Fusion **7**, 63 (1992).

[17] E.A.G Armour *et al.*, Proceedings of the XVIII International Conference on the Physics of Electronic and Atomic Collisions, Aarhus, Denmark, American Institute of Physics, pp. 478-490, 1993.

[18] M. Jeitler *et al.*, Physical Review A **51**, 2881 (1995).

[19] C. Petitjean *et al.*, Hyperfine Interactions **82**, 1993.

[20] M.P. Faifman *et al.*, Muon Catalyzed Fusion **4**, pp. 1-30, 1989.

[21] L.I. Ponomarev, Muon Catalyzed Fusion **3**, 629 (1988).

[22] M.P. Faifman *et al.*, Hyperfine Interaction **101-102**, pp. 179-189, 1996.

[23] M.P. Faifman, Muon Catalyzed Fusion **4**, pp. 341-364, 1989.

[24] I.V. Puzynin and S.I. Vinitsky, Muon Catalyzed Fusion **3**, 307 (1988).

[25] S.A. Alexander and H.J. Monkhorst, Physical Review A **38**, 26 (1988).

[26] D. Bakalov, Muon Catalyzed Fusion **3**, 321 (1988).

[27] G. Aissing and H.J. Monkhorst, Physical Review A **42**, 3789 (1990).

[28] K. Swe Myint *et al.*, Zeitschrift für Physik A **334**, 423 (1989).

[29] Yu.V. Petrov *et al.*, Physics Letters B **331**, pp. 266-270, 1994.

[30] E.A.G. Armour *et al.*, Physical Review A **46**, 6888 (1992).

[31] Yu.V. Petrov, Muon Catalyzed Fusion **1**, 219 (1987).

[32] L.I. Menshikov, Soviet Journal of Nuclear Physics **42**, 750 (1985).

[33] Yu. V. Petrov *et al.*, Muon Catalyzed Fusion **2**, pp. 261-272, 1988.

[34] M.P. Faifman, Muon Catalyzed Fusion **2**, 247 (1988).

[35] V.V. Kuziminov *et al.*, Hyperfine Interactions **101-102**, pp. 197-205, 1996.

[36] M.P. Faifman and L.I. Ponomarev, Physics Letters B **265**, 201 (1991).

[37] L.I Schiff, Quantum Mechanics, McGraw Hill, Singapore, 1968.

[38] L. Bracci *et al.*, Muon Catalyzed Fusion **4**, pp. 247- 302, 1989.

[39] C. Petitjean *et al.*, Muon Catalyzed Fusion **5-6**, 199 (1990-91).

[40] D.V. Balin *et al.*, Proceedings of the International Symposium of Muon Catalyzed Fusion '89, Oxford,p. 41, 1989.

[41] A.A. Vorobyov, Muon Catalyzed Fusion **2**, 17 (1988).

[42] G.G. Semenchuk it et al., Hyperfine Interactions **101-102**, pp. 57-65, 1996.

[43] K.A. Aniol *et al.*, Muon Catalyzed Fusion **2**, pp. 63- 72, 1988.

[44] J.G. Fetkovich *et al.*, Physical Review Letters **4**, 570(1960).

[45] G.G. Semenchuk *et al.*, Hyperfine Interactions **101-102**, pp. 547-562, 1996.

[46] Yu.V. Smirenin *et al.*, Hyperfine Interactions **101-102**, pp. 29-35, 1996.

[47] J. Van Kranendonk, Solid Hydrogen, Pelnum Press, New York, 1983.

[48] G. Burns, Solid State Physics, Academic Press Inc., San Diego, 1990.

[49] J.L. Beveridge *et al.*, Nuclear Instuments and Methods A **240**, 316 (1985).

[50] C.J. Oram *et al.*, Nuclear Instruments and Methods A **179**, 95(1981).

[51] P.E. Knowles *et al.*, Nuclear Instruments and Methods A **368**, 604 (1996).

[52] M.C. Fujiwara *et al.*, Nuclear Instruments and Methods A **395**, 159 (1997).

[53] E. Wicke *et al.*, Hydrogen in Metals II, Springer-Verlag, New York, pp. 73-151, 1978.

[54] R.M. Barrer, Hydrothermal Chemistry of Zeolites, Academic Press, London, 1982.

[55] Canberra Instruments Inc., Canberra Nuclear Instruments Catalogue, Edition Nine, Meriden, CT.

[56] W.R. Leo, Techniques for Nuclear and Particle Physics, Springer-Verlag, New York, 1987.

[57] Nuclear Enterprises, Scintillators for the Physical Sciences Catalogue, Edinburgh, Scotland.

[58] P.E. Knowles, Muonic Processes in Solid Hydrogen Films, Ph.D. Thesis, University of Victoria, 1996.

[59] A.W. Bennett and C. Kost, Molli Reference Manual, Triumf, 1985.

[60] A.W. Bennett, A.K. Haynes, Fiowa Reference Manual, Triumf and University of British Columbia, 1981.

[61] J.L. Chuma, Replay Reference Manual, TRIUMF Computing Document, 1987.

[62] J.L. Chuma, Physica Reference Manual, TRIUMF Computing Document, 1994.

[63] Handbook of Chemistry and Physics, 56th Edition,CRC Press, Inc., Ohio, 1974, 1975.

[64] V.V. Verbinski *et al.*, Nuclear Instruments and Methods **65**, 8 (1968).

[65] M.C. Fujiwara, Ph.D. Thesis, University of British Columbia, 1999.

[66] R.W. Huff, Annals of Physics **16**, 288 (1961).

[67] T. Suzuki *et al.*, Physical Review C **35**, 2212 (1987).

[68] J. Wozniak *et al.*, to be published in Hyperfine Interaction.

[69] G.M. Marshall *et al.*, to be published in Hyperfine Interaction.

[70] GEANT 3.21, CERN Program Library Long Writeup W5013, CERN, Geneva (1993).

[71] TRIUMF Users Handbook, TRIUMF Users Executive Committee, TRIUMF (1978).

[72] G.M. Marshall *et al.*, Hyperfine Interactions **101-102**, 47 (1996).

[73] A. Adamczak, Hyperfine Interactions **101-102**, 113, 1996.

[74] C. Chiccoli *et al.*, Muon Catalyzed Fusion **7**, 87 (1992).

[75] V.S. Melezhik and J. Wozniak, Muon Catalyzed Fusion **7**, 203 (1992).

[76] V.S. Melezhik, Hyperfine Interactions **101-102**, 365 (1996).

[77] J. Woźniak *et al.*, Hyperfine Interactions **101-102**, 573 (1996).

[78] J.S. Cohen, Physical Review A **344**, 2719 (1986).

[79] F. Mulhauser *et al.*, Physical Review A **53**, 3069 (1996).

[80] Y.A. Thalmann *et al.*, Physical Review A **57**, 1713 (1998).

[81] J.S. Cohen, private communication.

[82] P.E. Knowles *et al.*, Physical Review A **56** 1970 (1997).

[83] V.E. Markushin, Muon Catalyzed Fusion **3**, 395 (1987).

[84] Review of Particle Properties, Physical Review D **50**, 1180 (1994).

[85] S.S. Gershtein, Soviet Physics JETP **51**, 6 (1980).

[86] M. Leon, Physical Review Letters **52**, 605 (1984).

Appendix A

Resonant Molecular Formation Rate Normalization

Normalization of the resonant molecular formation rates is not straightforward when dealing with nonhomonuclear hydrogen and needs an explanation. The equations were published for the case of a muon in a deuterium/tritium mixture in which the convention

$$C_d + C_t = 1 \tag{A.1}$$

was used, where C_d and C_t are the normalized concentrations of deuterium and tritium nuclei [85,86]. The meaning of the molecular formation rate was given as

$$C_d \lambda_{dt\mu} = 2C_{D_2}\lambda_{dt\mu-d} + C_{DT}\lambda_{dt\mu-t} \tag{A.2}$$

where C_{D_2} and C_{DT} are the concentrations of D_2 and DT molecules. It is assumed that the mixture is in equilibrium so that the following equilibrium concentration expression applies

$$C_{D_2} : C_{DT} : C_{T_2} = {C_d}^2 : 2C_dC_t : {C_t}^2 \ . \tag{A.3}$$

The effective molecular formation rate in the kinetic equations at equilibrium was

defined as

$$\lambda_{dt\mu} = C_d\lambda_{dt\mu-d} + C_t\lambda_{dt\mu-t} \quad . \tag{A.4}$$

Consistency with Eq. (A.2) implies

$$C_{D_2} = \frac{C_d{}^2}{2} \quad , C_{DT} = C_dC_t \tag{A.5}$$

which is true only for

$$C_{D_2} + C_{DT} + C_{T_2} = 0.5 \ , \tag{A.6}$$

an equilibrated DT mixture; it means 25% D_2, 50% DT, 25% T_2. This convention is not immediately obvious or intuitive.

However if we now assume we do not have an equilibrated mixture of DT, but one in which 100% of the mixture is DT molecules, Eq. (A.1) still holds and we have $C_d = 0.5$ and $C_t = 0.5$. From Eq. (A.6) because we have 100% DT molecules we get C_{DT}=0.5. Writing Eq. (A.4) in terms of the values for the atomic concentrations gives

$$\lambda_{dt\mu} = 0.5\lambda_{dt\mu-d} + 0.5\lambda_{dt\mu-t}. \tag{A.7}$$

From Eq. (A.2) and using C'_d=0.5 with $C'_{DT} = 0.5$ we have the following

$$\lambda_{dt\mu} = \lambda_{dt\mu-t} \tag{A.8}$$

which contradicts Eq. (A.7). Thus, the conventions of [85] are not valid for non-equilibrated mixtures.

For the case of the HD data presented in the thesis, the targets consisted of 100% HD molecules. We believe that the correct normalization for comparison with rates calculated as in [22] is to assume Eq. (A.6), that is

$$\lambda_{dt\mu} = C_{HD}\lambda_{dt\mu-p} \tag{A.9}$$

where C_{HD}=0.5.

Appendix B

List of Abbreviations

ADC	Analogue-to-Digital Converter
AMP	Signal AMPlifier
ATT	Signal ATTenuator
$\overline{B}$F	Busy signal Fanout
CAMAC	Computer Automated Measurement And Control
CFD	Constant Fraction Discriminator
CLF	CLear Fan
CPINH	Clear Pulse INHibit
c_t	tritium concentration
del-e	Delay decay electron coincidence
del-tel	Delay decay electron coincidence with energy cut
DISC	Signal DISCriminator
DS	DownStream target foil
D14N1	Dynode 14 from the neutron detector 1 phototube
E1N, E2N	first and second plastic scintillators in front of N (neutron detector)
EB	End of Busy
EEVG	End of Event Gate
EGE	Plastic scintillator in front of GErmanium
EVENA	End of EVEnt gate timing output
EVG	EVent Gate
EVCL	EVent CLear
EVGF	EVent Gate Fan
EVTR	EVent TRigger
FAN	signal FANout
FIOWA	an analysis program
FMHM	Full Width Half Maximum
GE	GErmanium detector
GEANT	A Monte Carlo program
GMU	Good Muon (no pileup during the event)

HINH	Hardware INHibit
LINAMP	LINear AMPlifier
MOLLI	A histogramming program
μCF	Muon Catalyzed Fusion
1/N	prescaled trigger
NE213	plastic scintillator material used in the neutron detectors
N1	Neutron detector 1
N2	Neutron detector 2
NIM	Nuclear Instrument Module
PREAMP	PREAMPlifier
PSD	Pulse Shape Discriminator
PSD SHIFT	Pulse Shape Discrimination DC voltage level adaptor
PUG	Pile Up Gate
ϕ	density of liquid hydrogen (4.25×10^{22} nuclei/cm^3)
SET	Standard Emission Target (1000 Tl H_2 + 0.1% T_2)
SEMT	SET target with a 10 Tl D_2 overlayer
Si1, Si2	silicon detectors
S_F	muon stopping fraction
Ω_{Si}	silicon detector solid angle
SMC	Super Monte Carlo
STARBURST	CAMAC computer interface system
T1	Particle entry scintillator
T1AMP	Particle entry energy loss amplifier
T1ATT	Particle entry energy loss attenuator
T1HI	Particle entry with high threshold
T1IF	Particle entry signal fanout
T$\overline{BI}$	Particle entry, no busy, no inhibits
T$\overline{BIF}$	Signal fanout for the above
TBS	Tritium Barrier Space
TFAMP	Timing Filter Amplifier
Tl	Torr·liter
TRGF	TRiGger Fanout
TRGn	TRiGger signal n
TTL	Transistor-Transistor Logic: 5 V logic levels
US	UpStream target foil
VDACS	a standard data acquisition program